

**Surface and Interface Characterization of
 $\text{CH}_3\text{NH}_3\text{PbI}_{(3-x)}\text{Cl}_x$ and CsSnBr_3 Perovskite based
Thin-Film Solar Cell Structures**

Von der Fakultät MINT - Mathematik, Informatik, Physik,
Elektro- und Informationstechnik
der Brandenburgischen Technischen Universität Cottbus-Senftenberg
zur Erlangung des akademischen Grades eines
Doktor der Naturwissenschaften
(Dr. rer. nat.)

genehmigte Dissertation
vorgelegt von

Diplom-Physikerin

Claudia Marion Hartmann
geboren am 03.07.1984 in Berlin

Gutachter: Prof. Dr. Dieter Schmeißer

Gutachter: Prof. Dr. Klaus Lips

Gutachter: Prof. Dr. Marcus Bär

Tag der mündlichen Prüfung: 22. Juni 2018

Abstract

Perovskite-based solar cell devices promise high efficiencies and low cost, but their use in PV is limited by several factors. In this thesis, I look at the different limiting factors, e.g., pin-holes, decomposition and the toxicity of Pb, which can be eliminated/controlled by using Cs for better stability, Sn for less toxicity, and SnF₂ for better coverage and prevention of oxidation.

The chemical and electronic structure of solution-processable hybrid organometallic (CH₃NH₃PbI_(3-x)Cl_x) and completely inorganic (CsSnBr₃) perovskite materials have been studied using x-ray and electron based spectroscopic techniques. The morphology and local elemental composition of CH₃NH₃PbI_(3-x)Cl_x used as absorbers in PV devices, which define the film quality (properties) and influences the performance of the solar cell have been studied in detail. Further, the impact of water and light on the chemical structure of CH₃NH₃PbI_(3-x)Cl_x is studied in-situ to gain insight into the degradation mechanism responsible for the short life-time of the absorber and solar cell. For alternative, completely inorganic CsSnBr₃ absorbers, the impact of SnF₂, as an oxidation inhibitor on the chemical and electronic structure is studied to identify its role in the improved performance of the solar cell.

Photoemission electron microscopy (PEEM) is used to investigate the interface of the wet-chemically deposited 300 nm thick CH₃NH₃PbI_(3-x)Cl_x perovskite thin-film on planar compact TiO₂ (c-TiO₂, electron transporting material [ETM]) on FTO/glass substrates providing insight into coverage, morphology, local elemental composition and spatially resolved electronic structure of the sample. Microscopy images (PEEM and complementary scanning electron microscopy (SEM) images) reveal an incomplete coverage, with holes reaching down to the c-TiO₂ substrate. Three different topological regions with different degrees of coverage and chemical composition are identified. Depending on the degree of coverage, photoemission electron microscopy - x-ray photoelectron spectroscopy (PEEM-XPS) data indicate a variation in iodine oxidation and the formation of metallic Pb in the vicinity of the c-TiO₂ substrate. The valence band maxima (VBM) derived from PEEM-XPS for the perovskite and ETM give insight into the electronic structure, and combined with information from literature on

2,2',7,7'-Tetrakis-(N,N-di-4-methoxyphenylamino)-9,9'-spirobifluorene (spiro-MeOTAD, hole transporting material [HTM]), an excellent charge selectivity at the absorber/HTM and absorber/ETM interfaces respectively can be determined. Furthermore, the derived energy level alignment (using a combination of measurement and literature) indicates a large recombination barrier (on the order of 2 eV), which would prevent shunts from occurring due to contact between ETM and HTM in the pin-holes.

In-situ ambient pressure hard x-ray photoelectron spectroscopy (AP-HAXPES) studies of 60 and 300 nm thick $\text{CH}_3\text{NH}_3\text{PbI}_{(3-x)}\text{Cl}_x$ perovskites on c-TiO₂ have been performed under different conditions (i.e. vacuum/water and dark/UV light) to investigate the degradation process in-situ. 60 nm and 300 nm thick perovskite absorbers show distinct degradation mechanisms, which is partly (in addition to the nominal thickness difference) ascribed to the difference in morphology and the related differences in chemical composition. The 60 nm perovskite sample forms Pb^0 in water vapor ($p \sim 19.7 - 16.4$ Torr, non-defined illumination) in presence of x-rays (radiolysis), indicating a significant amount of PbI_2 contained in the sample and being converted into Pb^0 . The 300 nm thick perovskite sample illustrates a complex behavior under illumination and in the dark:

It is stable in the dark in high vacuum ($p \sim 1 \times 10^{-5}$ Torr). Introducing water vapor ($p = 15$ Torr) leads to adsorption of water on the perovskite, decreasing the signal of Pb^0 and the methylammonium iodide ($\text{CH}_3\text{NH}_3\text{I}$, MAI) related C species, whereas the perovskite related signal stays constant, indicating a dissolution of the perovskite mainly into its organic (MAI) and inorganic components (PbI_2).

In low vapor pressure ($p \sim 1.8 \times 10^{-4} - 2.6 \times 10^{-5}$ Torr) under illumination (with AM1.5G), water residues in the chamber from the previous experimental run serve as water source in high vacuum and a solar simulator as UV light source. A decrease of I, Pb perovskite (PbI_2) and MAI-related C species and an increase in Pb^0 indicates the dissolution of the perovskite into MAI and PbI_2 , and the further UV-induced formation of Pb^0 from PbI_2 . Additionally, a binding energy (E_B) shift, caused by surface photovoltage (SPV), is observed. The direction of this shift, caused by SPV, is influenced by the amount of water adsorbed on the sample surface.

HAXPES and lab-XPS measurements were performed on wet-chemically deposited CsSnBr_3 absorbers with and without SnF_2 on c-TiO₂/FTO/glass to study the impact of SnF_2 on the chemical and electronic structure. Two Sn, Cs and Br species are seen in all samples, where the second species is attributed to the oxidized Sn (Sn^{4+}) component. When adding SnF_2 to

the precursor solution, the coverage is improved and less oxidized Sn (Sn^{4+}) component and the related species can be observed, confirming the oxidation inhibiting properties of SnF_2 . Additionally, SnF_2 impacts the electronic structure, enhancing the density of states close to the valence band maximum (VBM).

In the recent years it has been shown that the film quality of the hybrid organometallic based perovskite absorbers influences the performance of the resulting solar cell. The surface and interface investigations of $\text{CH}_3\text{NH}_3\text{PbI}_{(3-x)}\text{Cl}_x/\text{c-TiO}_2$ based perovskite absorbers will give insight into the detrimental effect of morphology and ambient environment on the chemical and electronic structure determining the device performance. The results in this thesis show an inhomogeneous and gradually degrading film, suggesting, for device production, an improved deposition and protection of the film against moisture and UV light is needed. Alternative inorganic Pb-free perovskite absorbers such as CsSnBr_3 promise to be more stable and less toxic than organometallic perovskite, if the oxidation of the Sn can be controlled, by e.g., SnF_2 treatment or UHV deposition. The findings of the study of inorganic absorbers will help to comprehend the mechanism behind the improved performance of the solar cell due to the SnF_2 treatment and will aid in further improvements of the performance of the device.

Zusammenfassung

Perowskit basierte Solarzellen versprechen hohe Effizienzen und niedrige Kosten, aber ihre Anwendung in der PV ist beschränkt durch verschiedenen Faktoren. In dieser Doktorarbeit, werden die verschiedenen einschränkende Faktoren, wie z.B. Poren, Zersetzung und die Toxizität von Pb, näher untersucht, welche eliminiert/kontrolliert werden können durch Benutzung von Cs für eine besser Stabilität, Sn für weniger Toxizität, und SnF₂ für bessere Bedeckung und Prävention von Oxidation. Die chemische und elektronische Struktur von lösungs-basierten Hybrid-Organometallverbindungen (CH₃NH₃PbI_(3-x)Cl_x) und komplett inorganischen (CsSnBr₃) Perowskitabsorbern wurde mit Röntgen- und Elektronenspektroskopiemethoden untersucht. Die Morphologie und lokale elementare Zusammensetzung von CH₃NH₃PbI_(3-x)Cl_x Absorbern (angewendet in PV Applikationen), welche die Filmqualität (Filmeigenschaften) definieren und die Leistung der Solarzelle beeinflussen, wurden im Detail untersucht. Des Weiteren wurden die Auswirkungen von Wasser und Licht auf die chemische Struktur von CH₃NH₃PbI_(3-x)Cl_x Absorbern in-situ untersucht, um Einsicht in die Degradierungsvorgänge, welche für die kurze Lebenszeit des Absorbers und der Solarzelle verantwortlich sind, zu erhalten. Für alternative komplett inorganische CsSnBr₃ Absorber wurde die Auswirkung von SnF₂, als Oxidationshemmer auf dessen chemische und elektronische Struktur untersucht, um seine Rolle in der Verbesserung der Leistung der Solarzelle zu identifizieren.

Photoemissionselektronenmikroskopie (PEEM) wird zur Untersuchung der Grenzfläche von nasschemisch abgeschiedenem 300 nm dicken CH₃NH₃PbI_(3-x)Cl_x Perowskitdünnschichtfilmen auf planarem kompaktem TiO₂ (c-TiO₂, Elektrontransportmaterial [ETM]) auf FTO/-Glass Substraten angewendet und liefert Einblicke in die Bedeckung, Morphologie, lokale elementare Komposition und räumlich aufgelöste elektronische Struktur der Probe. Mikroskopiebilder (PEEM und komplementäre Rasterelektronenmikroskopie (SEM) Bilder) enthüllen eine unvollständige Bedeckung, mit Löchern die bis zum c-TiO₂ Substrat hinunterreichen. Es werden drei verschiedene Topologien mit unterschiedlichen Graden von Bedeckung und chemischer Zusammensetzung identifiziert. Abhängig von dem Grad der Bedeckung, zeigen die

Photoemissionselektronenmikroskopie-Röntgenphotoelektronenspektroskopie (PEEM-XPS) Daten eine Variation der Jod Oxidation und die Bildung vom metallischen Pb in der Nähe des c-TiO₂ Substrats. Die Valenzbandmaxima (VBM), bestimmt von den PEEM-XPS Daten für das Perowskit und ETM, liefern Erkenntnis über die elektronische Struktur und kombiniert mit Literaturinformationen über 2,2',7,7'-Tetrakis-(N,N-di-4-methoxyphenylamino)-9,9'-spirobifluorene (spiro-MeOTAD, Löchertransportmaterial [HTM]) kann jeweils eine exzellente Ladungselektivität an der Absorber/HTM und Absorber/ETM Grenzfläche ermittelt werden. Des Weiteren weist die Energiebandausrichtung (bestimmt durch eine Kombination von Messung und Literatur) eine große Rekombinationsbarriere auf (in der Größenordnung von 2 eV), welche das mögliche Auftreten von Shunts durch den Kontakt zwischen ETM und HTM in den Poren verhindert.

In-situ Umgebungsdruckröntgenspektroskopiestudien (AP-HAXPES) mit harter Röntgenstrahlung von 60 und 300 nm dicken CH₃NH₃PbI_(3-x)Cl_x Perowskiten auf c-TiO₂ wurden unter verschiedenen Umgebungsbedingungen (z.B. Vakuum/Wasser und dunkel/Licht) durchgeführt, um die Degradierungsprozesse in-situ zu untersuchen. Die 60 nm und 300 nm dicken Perowskitabsorber zeigen dabei verschiedene Degradierungsmechanismen, welche teilweise (zusätzlich zu der nominalen Schichtdickendifferenz) dem Unterschied in der Morphologie und der zugehörigen unterschiedlichen chemischen Zusammensetzung zu zuschreiben ist. Die 60 nm Perowskitprobe bildet in Wasserdampf ($p \sim 19.7 - 16.4$ Torr, nicht-definierte Beleuchtung) und in Gegenwart von Röntgenstrahlung Pb⁰ (Radiolyse), was auf einen signifikanten Anteil von PbI₂ in der Probe hinweist und in Pb⁰ umgewandelt wird. Die 300 nm dicke Perowskitprobe zeigt ein komplexes Verhalten unter Beleuchtung und im Dunkeln: Sie ist stabil im dunkeln Hochvakuum ($p \sim 1 \times 10^{-5}$ Torr). Einschleusen von Wasserdampf ($p = 15$ Torr) führt zur Adsorption von Wasser auf dem Perowskit, welches zur Verringerung des Signals von Pb⁰ und der Methylammoniumiodid (CH₃NH₃I, MAI) zugehörigen C Spezies führt, während das Perowskits zugehörige Signal konstant bleibt, welches eine Ausflösung des Perowskits, hauptsächlich in seine organischen (MAI) und anorganisch (PbI₂) Bestandteile, andeutet. Im niedrigen Dampfdruck ($p \sim 1.8 \times 10^{-4} - 2.6 \times 10^{-5}$ Torr) unter Beleuchtung (mit AM1.5G), dienen die Wasserrestbestände von dem vorherigen Experimentdurchlauf als Wasserquelle und ein Sonnensimulator dient als UV-Lichtquelle. Eine Verringerung von I, Pb Perowskit (PbI₂) und MAI zugehörigen C Spezies und ein Anstieg in Pb⁰ weisen auf eine Ausflösung des Perowskits in MAI und PbI₂ hin, und weiter auf eine UV-induzierte Bildung von Pb⁰ aus PbI₂. Zusätzlich wird eine Verschiebung in der Bindungsenergie (E_B), verursacht durch Oberflächen-

Photospannung (SPV), beobachtet. Die Richtung der Verschiebung, verursacht durch SPV, wird durch die adsorbierte Wassermenge auf der Probe beeinflusst.

HAXPES und Labor-XPS Messungen wurden an nasschemisch abgeschiedenem CsSnBr₃ Absorbern mit und ohne SnF₂ auf c-TiO₂/FTO/Glass durchgeführt, um die Auswirkungen von SnF₂ auf die chemische und elektronische Struktur zu untersuchen. Es sind in allen Proben zwei Sn, Cs und Br Spezies gefunden worden, wobei die Zweite Spezies der oxidierten Sn (Sn⁴⁺) Komponente zugeordnet wird. Wenn SnF₂ zur Ausgangslösung hinzugegeben wird, wird eine verbesserte Bedeckung und eine weniger oxidierte Sn (Sn⁴⁺) Komponente und deren zugehörigen Spezies beobachtet, welches die oxidationshemmenden Eigenschaften von SnF₂ bestätigt. Zusätzlich hat SnF₂ einen Einfluss auf die elektronische Struktur des Absorbers, es erhöht die Zustandsdichte in der Nähe des Valenzbandmaximums (VBM).

In den letzten Jahren wurde gezeigt, dass die Filmqualität der auf Hybrid-Organometallverbindungen basierenden Perowskitabsorbern die Leistung der Solarzelle beeinflusst. Die Oberflächen- und Grenzflächenuntersuchungen von CH₃NH₃PbI_(3-x)Cl_x/c-TiO₂ basierten Perowskitabsorbern geben Einsicht in die schädlichen Effekte von Morphologie und Umgebungbedingungen auf die chemische und elektronische Struktur, welche die Leistung der Solarzelle bestimmt. Die Ergebnisse in dieser Doktorarbeit zeigen einen inhomogenen und graduierlich zerfallenen Film und weisen, für die Modulherstellung auf eine Verbesserung der Deposition hin und das ein Schutzfilm gegen Feuchtigkeit und UV-Licht benötigt wird. Alternative anorganische Perowskitabsorber, wie CsSnBr₃, versprechen stabilere und weniger giftige Absorber im Vergleich zu Hybrid-Organometallverbindungs Perowskiten, wenn die Oxidation von Sn kontrolliert werden kann, wie z.B. durch die SnF₂ Behandlung oder UHV Deposition. Die Ergebnisse der Untersuchung von anorganischen Absorbern wird zum besseren Verständnis der Vorgänge hinter der gesteigerten Leistung der Solarzelle durch die SnF₂ Behandlung und zur weiteren Verbesserungen der Leistung von Anwendungen beitragen.

Contents

1. Introduction	1
2. Thin-Film Absorbers and Application in Solar Cells	5
2.1. Perovskite Absorbers in Solar Cells	6
2.2. Hybrid Organometallic Perovskites	7
2.2.1. Device Performance Limiting Factors	7
2.2.2. Proposed Degradation Pathways for CH ₃ NH ₃ PbI ₃ Perovskites	8
2.2.3. Properties of Hybrid Organometallic Perovskite Absorbers	10
2.2.4. Sample Preparation of CH ₃ NH ₃ PbI _(3-x) Cl _x Absorbers	10
2.3. Inorganic Pb-free CsSnX ₃ -based Perovskites	11
2.3.1. Sample Preparation of CsSnBr ₃ Absorbers	12
3. Methods and Experimental Details	13
3.1. Photoelectron Spectroscopy (PES)	13
3.2. Scanning Electron Microscopy(SEM) and Energy Dispersive X-ray Spectroscopy (EDX)	15
3.3. Photoelectron Emission Microscopy (PEEM)	16
3.4. Data analysis	16
3.4.1. Curve Fit Analysis	16
3.4.2. Inelastic Mean Free Path and Layer Thickness	19
3.4.3. Valence Band, Conduction Band, and Band Offset	20
3.5. Experimental Set-up and Details	21
3.5.1. Laboratory-based Techniques	21
3.5.2. Synchrotron-based Techniques	22
4. Spatially-Resolved Characterization of the CH₃NH₃PbI_(3-x)Cl_x/TiO₂ Interface	27
4.1. Results and Discussion	27
4.1.1. Morphology and Elemental Distribution Study by SEM and EDX	27

Contents

4.1.2. Chemical Structure Study by PEEM-XAS and -XPS	30
4.1.3. Electronic Structure	39
4.1.4. Summary	43
5. In-situ Study and Characterization of Environmental Impact on Mixed Halide Perovskite Absorbers	45
5.1. 60 nm Perovskites in UHV and Water Vapor	46
5.2. Environmental Effects on 300 nm Perovskites	53
5.2.1. Perovskite in the Dark and in High Vacuum	54
5.2.2. Perovskite in the Dark and Water Vapor	59
5.2.3. Perovskite in the Light and Water	65
5.2.4. Degradation of 300 nm Perovskite in Ambient Environment	71
5.3. 60 nm vs. 300 nm Perovskite	74
6. Inorganic Pb-free CsSnBr₃ Perovskites	77
6.1. Results and Discussion	77
6.1.1. Chemical Structure of CsSnBr ₃ Perovskites	77
6.1.2. Electronic Structure of CsSnBr ₃	84
6.1.3. Summary	88
7. Conclusion and Outlook	89
A. Appendix A	93
B. Appendix B	95
B.1. 60 nm Perovskite	95
B.2. 300 nm Perovskite	104
B.2.1. 300 nm Perovskite in the Dark	104
B.2.2. 300 nm Perovskite under Illumination	108
C. Appendix C	119
Bibliography	127
Publications	141
Acknowledgement	141

List of Symbols and Abbreviations

ALS	Advanced light source in Berkeley
AM1.5(G or D)	Air mass 1.5 (global or direct)
(AP-)HAXPES	(Ambient pressure) hard x-ray photoelectron spectroscopy
B	Magnetic field of the bending magnet
B₀	Amplitude of the magnetic field
BESSY II	Berliner Elektronenspeicherring-Gesellschaft für Synchrotronstrahlung m.b.H
c	Speed of light in vacuum
c – TiO₂	Compact TiO ₂
CB(M)	Conduction band (minimum)
CBO	Conduction band offset
CdTe	Cadmium telluride
CIGS	Copper indium diselenide
CL	Core level
d	Thickness
D(E, k)	Transport probability
DMF	N,N-dimethylformamide
DMSO	Dimethyl sulfoxide
DOS	Density of states

List of Symbols and Abbreviations

DSSCs	Dye-sensitized solar cells
e	Elemental charge
ϵ	Emittance
E_B	Binding energy
E_C	Critical energy
EDX	Energy dispersive x-ray spectroscopy
E_e	Electron energy
$E_f(\mathbf{k})$	Energy of final state
E_F	Fermi level
E_G	Band gap
$E_i(\mathbf{k})$	Energy of initial state
E_{kin}	Kinetic energy
EMIL	Energy Materials In-Situ Laboratory Berlin
ETM	Electron transporting material
E_{Vac}	Vacuum level
FA	Formamidinium $CH(NH_2)_2^+$
FTO	Fluorine-doped tin oxide
FWHM	Full width half maximum
γ	Lorentzian factor
G_U	Undulator gap
h	Planck's constant
\mathcal{H}	Perturbation operator
HI	Hydroiodic acid

List of Symbols and Abbreviations

HiKE	High Kinetic Energy Photoelectron Spectrometer
HOMO	Highest occupied molecular orbital
HTM	Hole transporting material
HZB	Helmholtz-Zentrum Berlin für Materialien und Energie
I_0	Intensity of bare absorber/substrate
I_{cov}	Intensity of cover layer
$I_{\text{ref}}^{\text{cov}}$	Saturated intensity of thick cover layer
IE	Ionization energy
iibb	Interface induced band bending
IMFP	Inelastic mean free path (λ)
IPES	Inverse photoelectron spectroscopy
j	Total angular momentum quantum number
k	Wave vector of the electron
K	Non-dimensional magnetic strength
λ_e	Mean-free path of electrons
Linac	Linear accelerator
λ_U	Undulator period
LUMO	Lowest unoccupied molecular orbital
m	Mass
MA	Methylammonium CH_3NH_3^+
MAI	Methylammonium iodide $\text{CH}_3\text{NH}_3\text{I}$
η	Power conversion efficiency
NAPXPS	Near-ambient-pressure x-ray photoelectron spectroscopy

List of Symbols and Abbreviations

p	Pressure
Φ	Work function
PEEM	Photoemission electron microscopy
PEEM-XAS	Photoemission electron microscopy - x-ray absorption spectroscopy
PEEM-XPS	Photoemission electron microscopy - x-ray photoelectron spectroscopy
PES	Photoelectron spectroscopy
PV	Photovoltaic
RF	Radio frequency
SEM	Scanning electron microscopy
SMART	Spectro-Microscope with Aberration correction for many Relevant Techniques
spiro-MeOTAD	2,2',7,7'-Tetrakis-(N,N-di-4-methoxyphenylamino)-9,9'-spirobifluorene
SPV	Surface photovoltage
UHV	Ultra-high vacuum
UPS	Ultra violet photoelectron spectroscopy
UV	Ultra violet
v	Velocity
ν	Frequency of wave
VB(M)	Valence band (maximum)
VBO	Valence band offset
V_{OC}	Open circuit voltage
W_{fi}	Transition probability for optical excitation
WIS	Weizmann Institute of Science

List of Symbols and Abbreviations

χ^2	Describes the Goodness of fit
XPS	X-ray photoelectron spectroscopy
XRD	X-ray diffraction

1. Introduction

The growing energy consumption world wide is heading towards a shortage/use-up of fossil fuels needed for energy production. The burning of fossil fuels is on top of that also harmful for the environment and health; society is compelled to rethink energy production and energy resource management. Directing the focus towards renewable energies using replenishable sources like wind, water, sunlight etc. In particular sunlight is a clean source of energy and available world wide allowing the direct conversion of light into electricity, aka photovoltaics (PV).

Over the last years diverse solar cells based on different absorber materials and device structures have been developed. In addition to the conventional and commercially dominant wafer based solar cells (made from crystalline silicon) also thin-film solar cells have surged. Solid-state thin-film technology, based on amorphous silicon, cadmium telluride (CdTe), and copper indium gallium (di)selenide (CIGS) absorbers are already commercially available. They promise a lower production cost due to lower amount of materials needed for production. Thin-film technology is also compatible with light, flexible substrates, finding use in utility-scale based application, e.g. building integrated PV [1].

Thin-film technologies based on organic or partially organic materials, e.g. organometallic compounds, which are currently in research and development stages promise efficiency greater than or equal to that of the already existing thin-film solar cells on the market, at lower production cost. The hot topic in that research category has recently been the mixed-halide organometallic perovskites, e.g., $\text{CH}_3\text{NH}_3\text{PbI}_3$ and $\text{CH}_3\text{NH}_3\text{PbI}_{(3-x)}\text{Cl}_x$. A material class that has evolved from dye-sensitized solar cells into perovskite solid-state solar cells with efficiencies currently exceeding 22 % [2]. However, they are still inhibited by a short lifetime due to instability of the absorber [3–9]. Nevertheless the easy production of the perovskite, e.g., spin-coating (on even flexible substrates [10]) and the tunability of the band gap [11] make it a very interesting material for a variety of applications, including combinations with other absorbers like silicon for tandem solar cells [12].

Introduction

The continued fast increase in conversion efficiencies is one of the key aspects in perovskite research, limited in real devices i.a. by the quality of the absorber film [13, 14]. For perovskite layers e.g., in planar device structures, spin-coating leads to incomplete coverage of the compact electron transporting material (ETM), suffering from pin-hole formation limiting the efficiency [14, 15].

Another limiting factor for the efficiency of e.g., inorganic-organic hybrid perovskite solar cells is the short lifetime and instability of the absorber in ambient environment, making them not applicable for the market at the moment. They are sensitive to moisture/water and ultraviolet (UV) light, which degrades the absorber material reducing the efficiency greatly [16]. To move toward real-life applications of the technology, "degradation" studies of perovskite under different conditions have been performed to understand the corresponding mechanism behind it and to ultimately improve the stability [16–21].

In the community, efforts have been put into encapsulation to enhance the stability and lifetime of hybrid perovskites [22–24]. Another approach is the replacement of the hygroscopic and UV-sensitive organic component with e.g., inorganic Cs, to improve stability, and the replacement of Pb with Sn to reduce the toxicity of the solar cell. The resulting completely inorganic CsSnX_3 based-perovskite, with $X = \text{I, Cl or Br}$, has so far shown only low efficiencies [25, 26], partially due to the easy oxidation of Sn in air [27–29].

This thesis focuses on the absorber's surfaces and interfaces of the different perovskite stacks $\text{CH}_3\text{NH}_3\text{PbI}_{(3-x)}\text{Cl}_x/\text{c-TiO}_2$ and $\text{CsSnBr}_3/\text{c-TiO}_2$ to study and understand their chemical and electronic properties which are necessary for further device optimization.

Spatially-resolved analysis of the perovskite at this interface gives insight into the laterally-resolved chemical and electronic properties, offering the possibility to explain the reasonable performance and why the resulting device is not completely short circuited (see chapter 4). Further the degradation of the perovskites under different ambient conditions is studied (see chapter 5); many degradation paths have already been proclaimed but the process and contributing factors behind it is not fully understood yet.

Since humidity/UV light and also Pb is a disadvantage for the current perovskite solar cell devices also alternative presumably more stable $\text{CsSnBr}_3/\text{c-TiO}_2$ interfaces were studied. SnF_2 has been shown to improve efficiency of corresponding solar cells by inhibiting the oxidation of Sn [25, 29]. However the impact of SnF_2 on the chemical and electronic properties of CsSnBr_3 is not completely understood and will be evaluated for further device improvement in the future (see chapter 6).

The interfaces were studied by using spatially resolved photoelectron emission microscopy in UHV and non-spatially resolved x-ray photoelectron emission spectroscopy (XPS) in UHV and under ambient conditions for $\text{CH}_3\text{NH}_3\text{PbI}_{(3-x)}\text{Cl}_x$. For CsSnBr_3 XPS studies were performed solely in UHV.

This thesis is outlined as follows: Chapter 2 introduces the different absorbers used for perovskite-based solar cells and studied in this thesis along with their preparation procedure. In chapter 3 the methods used within this thesis and the relevant theoretical basics will be briefly introduced along with the details of the equipment. Chapter 4 presents the measurements and results of the spatially-resolved study of the $\text{CH}_3\text{NH}_3\text{PbI}_{(3-x)}\text{Cl}_x/\text{c-TiO}_2$ interface crucial for device performance. In chapter 5 the same absorbers were studied under ambient conditions, monitoring the chemical changes of the interfaces with a non-closed film and tracing the degradation. Chapter 6 presents the study of $\text{CsSnBr}_3/\text{c-TiO}_2$ absorber and the impact of SnF_2 on the oxidation of Sn and the related properties of the absorber.

2. Thin-Film Absorbers and Application in Solar Cells

In this chapter, a brief introduction to the basics of thin-film solar cells will be given, focusing specifically on hybrid organometallic and inorganic Pb-free perovskite thin-film absorbers studied within this thesis.

Solar cells in general are electrical devices, generally based on semiconductors, which convert the energy of light into electricity by the photovoltaic effect. Under illumination with sunlight, solar cells absorb photons with an energy $h\nu$ larger than the band gap E_G ($\neq 0$) of the absorber material and excite electrons from the valence band into the conduction band, leaving a hole behind. The so-created electron-hole pairs will be then spatially separated by electrical contacts. The separation is facilitated by an internal field produced by, e.g., a p-n junction. The p-n junction can be divided into two types: an p-n heterojunction consisting of different p- and n-doped materials, or a homojunction where an internal field is created by differently doping the same material.

Since for the creation of many electron-hole pairs, photon energies $h\nu > E_G$ are required, E_G should be adapted to the terrestrial sun spectrum, which is shown in Figure 2.1 a) under AM0 (abbr. for air mass) and AM1.5G, to enable the absorption of as many photons as possible. Air mass in general describes the relative path length of the solar radiation traveling from the sun to the earth surface through the atmosphere, being 0 for radiation outside the Earth atmosphere and 1.5 for radiation passing through the atmosphere under an angle of 48.2° [30]. The latter describes a longer path way for the irradiation through the atmosphere causing losses in intensity through absorption and scattering. An AM1.5(G [global] or D [direct]) solar spectrum is usually used to test solar cells and determine their conversion efficiency η . Note that AM1.5G has an integrated power density of 1000 W/m^2 whereas AM1.5D has an integrated power density of only 900 W/m^2 [31]. The theoretical limits for η (Shockley-Queisser limit) of p-n junction solar cells were determined, based on AM1.5, by W. Shockley and H. J. Queisser in 1961 [32]. Figure 2.1 b) shows the efficiency for different band gaps, indicating a maximum efficiency (around 33%) for E_G between 1.2 and 1.4 eV .

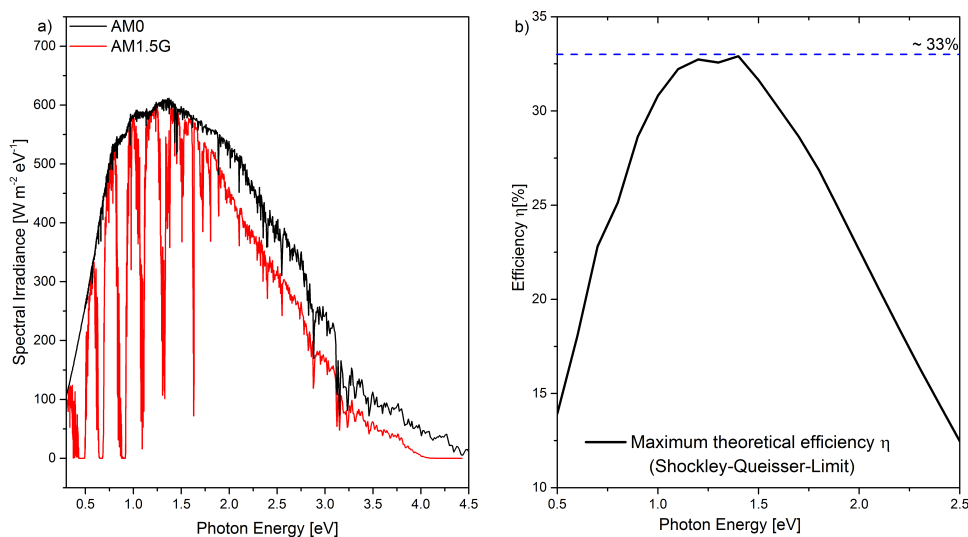


Figure 2.1.: a) Shows the terrestrial AM0 and AM1.5G sun spectrum. Data was taken from Ref. [31] and energy scale converted into photon energy. b) Shows the Shockley-Queisser limit for single junctions solar cells. Data were taken from Ref. [33].

2.1. Perovskite Absorbers in Solar Cells

The story of perovskites as absorbers in solar cells started basically in 1991, when Grätzel first described dye-sensitized solar cells (DSSCs) [34], from which the solid-state sensitized perovskite solar cells have evolved. The DSSC consist of a redox-active electrolyte and a light-absorbing dye introduced into mesoporous TiO_2 , which increases covering area and light absorption of the dye [3]. The dye was then replaced by inorganic-organic perovskite-based materials introduced into the mesoporous TiO_2 , and resulting in a cell first reported by Kojima et al. in 2009 with an efficiency of 3.8% [35]. Since then the solid-state hybrid solar cells based on solution-processable inorganic-organic perovskite absorber layers have exceeded the 20% conversion efficiency [2, 36, 37] promising low material and production cost.

Materials denoted as perovskites have an AMX_3 crystal structure composed of a cation A, a metal cation $\text{M} = \text{e.g., Pb or Sn}$ and a halide anion $\text{X} = \text{I, Cl, or Br}$. The cation A could be an organic ion e.g. CH_3NH_3^+ (Methylammonium, MA) or $\text{CH}(\text{NH}_2)_2^+$ (Formamidinium, FA) for hybrid organometallic perovskites or inorganic e.g., Cs. For perovskites, different combinations of cations and anions are possible, including mixtures with varying ratios of different halides, metals and organic/inorganic components, to either tune the band gap [11, 38, 39] and therefore tune the optoelectronic properties of the perovskite, or to improve the stability [40, 41], which

2.2 Hybrid Organometallic Perovskites

is still one of the main issues for application of perovskites in solar cells.

Figure 2.2 shows the corresponding n-i-p planar and mesoscopic structure of the solar cell devices based on the absorbers studied in this thesis. The mesoscopic structure consists of a mesoporous TiO_2 (mp- TiO_2) layer on top of c- TiO_2 on FTO/glass covered with a perovskite layer (here CsSnBr_3 [25]), hole transporting material (HTM, here 2,2',7,7'-tetrakis-(N,N-di-4-methoxyphenylamino)-9,9'-spirobifluorene [spiro-MeOTAD]) and Au contact. For the planar structure the c- TiO_2 on FTO/glas is covered by the perovskite (here $\text{CH}_3\text{NH}_3\text{PbI}_{(3-x)}\text{Cl}_x$ [15]) covered with a HTM (here: spiro-MeOTAD) and Au contacts. In both structures TiO_2 is the electron transporting material (ETM).

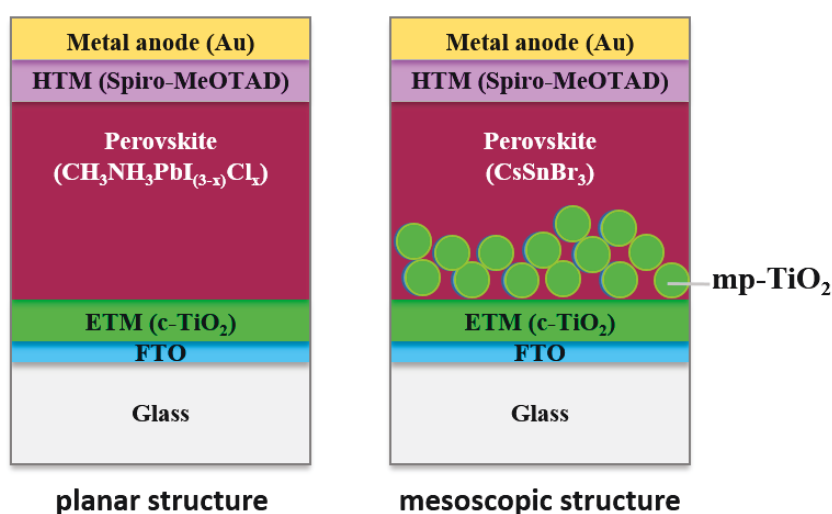


Figure 2.2.: Shows the n-i-p planar and mesoscopic device structure based on the two perovskite absorber types studied in this thesis. Adapted from Ref. [13]

2.2. Hybrid Organometallic Perovskites

2.2.1. Device Performance Limiting Factors

For perovskite solar cells the performance of the device is determined by the film quality of the absorber layer as one of the main factors [13, 14]. Leading solution-processed hybrid organometallic perovskites to conversion efficiencies exceeding 20% [2, 36, 37], with the highest efficiencies achieved by using a mesoporous electron transport material (ETM) scaffold of TiO_2 or Al_2O_3 [5] upon which the perovskite is spin-coated. However, devices based on a planar device structure should also be able to reach high performances, although they lag behind

in that respect so far. Therefore, a lot of work is invested into the development of a method to successfully deposit the perovskite layer directly on compact ETMs (e.g., from solution at low process temperatures $< 150^\circ \text{C}$ for low cost) [3, 15, 42].

Spin-coated perovskite layers on compact ETMs tend to have an incomplete coverage, suffering from pin-hole formation in the perovskite, limiting the efficiency [15], which might decrease light absorption (limiting the current) and might result in a direct contact between HTM and ETM, providing low-resistance shunt paths causing electron-hole recombination (limiting the voltage) [14]. Alternatively the deposition of a transparent, insulating shunt-blocking layer on the uncovered ETM introduced into the device structure can enhance the open circuit voltage (V_{OC}) without deteriorating charge extraction [43] and minimizing the risk of shunting.

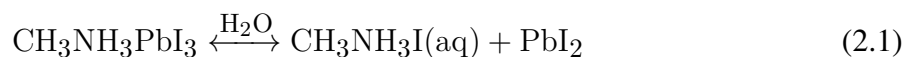
Another device performance limiting factor of the hybrid organometallic perovskites is the stability of the absorber under different environmental conditions (e.g., moisture and UV light) [16]. Leading to a degradation of the absorber during/after exposure to sunlight, elevated temperatures and/or humidity [13] reducing the efficiency of the resulting solar cell, which is very unfavorable for outdoor applications.

2.2.2. Proposed Degradation Pathways for $\text{CH}_3\text{NH}_3\text{PbI}_3$ Perovskites

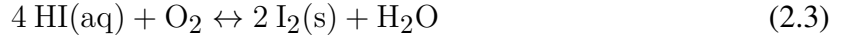
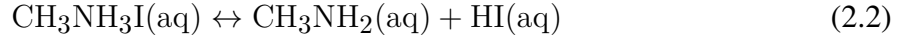
To improve the stability of hybrid organometallic perovskite, leading to devices with good reproducibility, a long lifetime, and high efficiencies, an understanding of the degradation process is necessary [16]. Part of the stability issue is already being addressed, to improve e.g., moisture stability, by protection of the perovskite layer from the humid environment by depositing Al_2O_3 layers between the perovskite and HTM (or on top of the HTM) [22, 23] or by encapsulation [24, 44]. Similar attempts have been done to improve the UV stability by including UV cutoff filters on top of the perovskite [45, 46].

To unravel the degradation paths of the perovskite in a humid environment and/or under UV light illumination, a lot of studies have been done so far, but most of them were done without monitoring the change of the absorber under ambient conditions (ex-situ) [16–21].

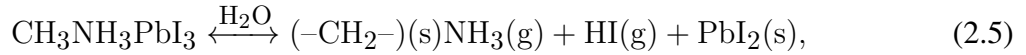
The degradation path described in literature usually includes moisture, oxygen and light together. In the following the proposed degradation mechanism for $\text{CH}_3\text{NH}_3\text{PbI}_3$ according to [9, 16, 47] are summarized:



2.2 Hybrid Organometallic Perovskites

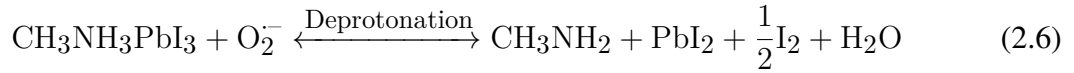


For the reaction in equation 2.3 and 2.4 oxygen and UV light are necessary. If no oxygen or light is available, the degradation ends with equation 2.2 [21]. Another possible starting degradation path of $\text{CH}_3\text{NH}_3\text{PbI}_3$ in water could be

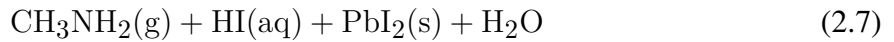


which Ke et al. [48] supports in their Near-ambient-pressure X-ray photoelectron spectroscopy (NAPXPS) study with water. Additionally stating the further decomposition of PbI_2 under water and UV light exposure into Pb^0 and I_2 .

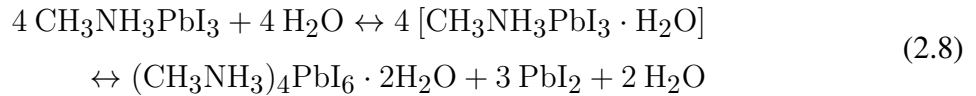
Also other degradation paths are proposed with varying environment parameters leading always to PbI_2 as the end product, which has a yellow color and clearly indicates a degradation of a perovskite by its color change from brown for $\text{CH}_3\text{NH}_3\text{PbI}_3$ to yellow. In case of light and oxygen a deprotonation happens according to [47]:



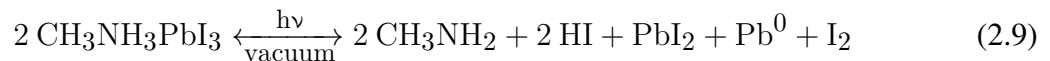
Equation 2.6 further converts under UV illumination and O_2 to [21]:



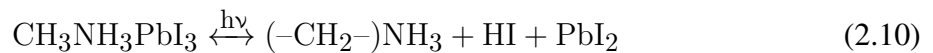
For samples in the dark and moisture the following degradation path is proposed [47]:



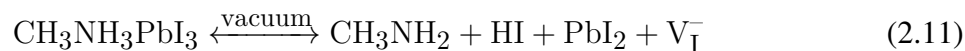
The degradation path of perovskite proposed under illumination without water or oxygen is according to [19, 20]:



or



Further PbI_2 separates under illumination into Pb^0 and I_2 . Also Tang et al. [19] proposes a degradation of perovskite in vacuum in the dark due to iodine vacancy (V_I^-) formation:



The final degradation product in the dark and vacuum is PbI_2 , whereas vacuum and light lead to PbI_2 and Pb^0 as final degradation products [19].

Still in-situ measurements (e.g., monitoring the changes of the material properties) in vacuum and at ambient pressure with and without UV irradiation in addition to water vapor exposure are missing to complement the degradation picture of the perovskite.

2.2.3. Properties of Hybrid Organometallic Perovskite Absorbers

The $\text{CH}_3\text{NH}_3\text{PbI}_3$ perovskite absorber discussed in this section has a band gap between 1.5 and 1.6 eV [49], which is higher than the ideal band gap between 1.2 and 1.4 eV close to the Shockley-Queisser Limit. $\text{CH}_3\text{NH}_3\text{PbI}_{(3-x)}\text{Cl}_x$ (discussed in 4 and 5), obtained by adding Cl to the precursor solution (see subsection 2.2.4), has a band gap of 1.55 eV [49], longer diffusion length [50] enhancing carrier transport, a high optical absorption coefficient, and better charge mobility [51] and lifetime [52] compared to $\text{CH}_3\text{NH}_3\text{PbI}_3$. The Cl in $\text{CH}_3\text{NH}_3\text{PbI}_{(3-x)}\text{Cl}_x$ also reduces the charge recombination [52] and the resulting solar cells exhibit a high open circuit voltage [5]. However the distribution/location of Cl in the film remains uncertain; it is assumed that after preparation of the sample the Cl is depleted at the surface (enrichment of Cl at the interface) [53] or it has facilitated during preparation the release of excess CH_3NH_3^+ , leading to x-ray diffraction (XRD) structure identical to $\text{CH}_3\text{NH}_3\text{PbI}_3$ [54], suggesting the absence of Cl in the absorber.

2.2.4. Sample Preparation of $\text{CH}_3\text{NH}_3\text{PbI}_{(3-x)}\text{Cl}_x$ Absorbers

The device-relevant 300 nm thick $\text{CH}_3\text{NH}_3\text{PbI}_{(3-x)}\text{Cl}_x$ perovskite thin-films studied in this thesis were prepared on compact $\text{TiO}_2/\text{FTO}/\text{glass}$ substrates at the University of Oxford (group of H. Snaith) using their standard one-step preparation method according to [5, 15].

The compact TiO_2 (c- TiO_2) layers, acting as the electron transporting material (ETM), were prepared by spin-coating an acidic solution of titanium isopropoxide dissolved in ethanol at 2000 rpm for 60s on fluorine-doped tin oxide (FTO) substrates (Pilkington, TEC7), followed

2.3 Inorganic Pb-free CsSnX₃-based Perovskites

by drying at 150°C and annealing at 500°C for 45 min.

The methylammonium iodide (CH₃NH₃I, "MAI") was synthesised by reacting a 33 wt% methylamine (CH₃NH₃) solution in ethanol with a 57 wt% hydroiodic acid (HI) in water at room temperature. For the crystallization of MAI the reacted solution was dried by using a rotary evaporator resulting in a white colored powder.

For the one-step deposition of the perovskite, the precursor solution was prepared by dissolving MAI and lead (II) chloride (PbCl₂) in anhydrous N,N-dimethylformamide (DMF) in a 3:1 molar ratio with a final concentration of 2.64 mol/l MAI and 0.88 mol/l PbCl₂. This precursor solution was then spin-coated onto compact TiO₂ at 2000 rpm in a nitrogen-filled glovebox for 45 s and left to dry at room temperature inside the glovebox, allowing the solvent to slowly evaporate. After drying, an annealing step for 2.5 h at 90°C was done for the crystallization and formation of the perovskite structure. For absorbers with a decreased thickness of 60 nm the precursor solution is diluted with DMF before spin-coating.

The freshly prepared samples were sealed in a container under inert gas and transferred from the University of Oxford to the Helmholtz-Zentrum Berlin für Materialien und Energie (HZB), where they were stored and/or unpacked and mounted on sample holders in a N₂-purged glovebox. The handling/storing of samples under inert gas is necessary due to high moisture sensitivity of the perovskite leading to degradation and decomposition of the absorber material. In cases where introducing of samples into the experimental set-up under inert gas atmosphere was not possible, the exposure to ambient air was kept at minimum (such specific cases will be identified where appropriate).

The preparation of the CH₃NH₃PbI_(3-x)Cl_x absorbers described so far and studied throughout this thesis do not represent a complete solar cell. For the completion of the solar cell device a hole transporting material (HTM), usually spiro-MeOTAD would be spin-coated on top of the 300 nm perovskite layer. For contacting the solar cell, a gold or silver electrode is thermally evaporated on top of the spiro-MeOTAD.

2.3. Inorganic Pb-free CsSnX₃-based Perovskites

Hybrid organometallic perovskite, e.g. CH₃NH₃PbI_(3-x)Cl_x, as briefly mentioned in the previously section, have two major issues: One is the toxicity of Pb and the other is the instability of the hybrid-based perovskite solar cell due to Ultraviolet (UV) induced radiation damage of the organic component in addition to moisture instability.

The toxicity issue can be addressed by replacing Pb with Sn. Sn in conjunction with organic

components is toxic, but not in its inorganic form [55]. The second issue can be approached by completely substituting the organic cation(s) with (inorganic) Cs to improve device longevity [56]. Incorporating these modifications leads to a new variant of inorganic Pb-free perovskites - CsSnX_3 - as promising alternative absorbers.

Devices based on CsSnX_3 have thus far exhibited only relatively low efficiencies [25,26], possibly due at least in part to the easy oxidization from Sn^{+2} to Sn^{+4} producing deep defects in the absorber [27,29]. Adding SnF_2 during preparation seems to inhibit this oxidation [29] and increase conversion efficiency [25,29]. For CsSnBr_3 samples with SnF_2 , a band gap of 1.75 eV and an efficiency of 2.1% with an improved V_{OC} is found [25]. However, the exact mechanism behind the SnF_2 treatment, in particular its impact on the chemical and electronic structure, is not yet fully understood.

2.3.1. Sample Preparation of CsSnBr_3 Absorbers

The CsSnBr_3 samples studied in this thesis were prepared by the Weizmann Institute of Science (WIS) in Israel according to [25]. They prepared two types of samples, CsSnBr_3 without and with SnF_2 on compact TiO_2 on FTO coated glass substrates (Xinyan Technology, TCO-XY15). First, layers of compact TiO_2 (70 nm) were deposited on FTO coated substrates by spray pyrolysis of a 30 mM titanium diisopropoxide bis(acetylacetonate) solution in isopropanol using air as the carrier gas on a hot plate, which was set to $\sim 500^\circ\text{C}$. The substrate was then annealed in air at 160°C and 500°C respectively for 1 h each. After cooling down, the sample was transferred into the glovebox for the deposition of the perovskite (the HTM layer was skipped for our purposes, for a complete cell it would also be deposited in the glovebox).

For the preparation of the precursor solution resulting in 0.8 M of CsSnBr_3 , 0.170 g of cesium bromide (CsBr) and 0.222 g of tin bromide (SnBr_2) were mixed together. For the required 20 mol% of tin fluoride (SnF_2 from Sigma Aldrich) 0.025 g of SnF_2 were added to the mixture followed-up by 1 mL of dimethyl sulfoxide (DMSO). The resulting precursor solution was stirred over night at 75°C and filtered afterwards. Then the solution was spin-coated on pre-heated TiO_2 substrates (at 100°C) for 30 seconds at 2000 rpm followed by a drying process at 100°C for 10 minutes.

After preparation, the samples were packed and sealed under inert gas and shipped from WIS to HZB. Since the CsSnBr_3 samples contain tin, which is highly air sensitive, the samples were stored and handled in a N_2 -filled glovebox to avoid oxidation and therefore degradation.

3. Methods and Experimental Details

In this chapter an introduction into the characterization methods, instrumentation, and analysis used within the scope of this thesis will be given.

For studying the chemical and electronic properties of the perovskite absorber, mostly photoelectron spectroscopy (PES) was used. But also supporting/complementary methods like scanning electron microscopy, elemental distribution maps, and photoelectron emission microscopy were used.

3.1. Photoelectron Spectroscopy (PES)

PES is a common technique to study electronic and chemical properties of a material due to its capability of being element and compound specific. It is based on the photoelectric effect: When a solid is irradiated with (monochromatic, in this case) photons of sufficient energy (x-rays or UV), electrons within the solid are excited from occupied (initial, $|i, \mathbf{k}\rangle$) into empty (final, $|f, \mathbf{k}\rangle$) states from where they are released into vacuum and detected by an electron-energy analyser.

The excitation of an electron (for a single particle system) is described by Fermi's golden rule transition probability for optical excitation [57]:

$$W_{fi} = \frac{1}{h} |\langle f, \mathbf{k} | \mathcal{H} | i, \mathbf{k} \rangle|^2 \delta(E_f(\mathbf{k}) - E_i(\mathbf{k}) - h\nu) \quad (3.1)$$

Where \mathcal{H} is the perturbation operator for a system disturbed by an electromagnetic field and the δ -function describes the energy conservation in the excitation of the electron from an initial state $E_i(\mathbf{k})$ into a final state $E_f(\mathbf{k})$ of the electronic band structure. \mathbf{k} is the wave vector of the electron.

Further, the propagation of the excited electron to the surface and emission of the electron from the solid into the vacuum are not completely described by Fermi's golden rule and loss processes need to be taken in consideration. The propagation of the electrons can be described by the transport probability $D(E, \mathbf{k})$ which is proportional to the mean-free path λ_e (without inelastic scattering). Transmission of the photoelectron through the surface is theoretically described by

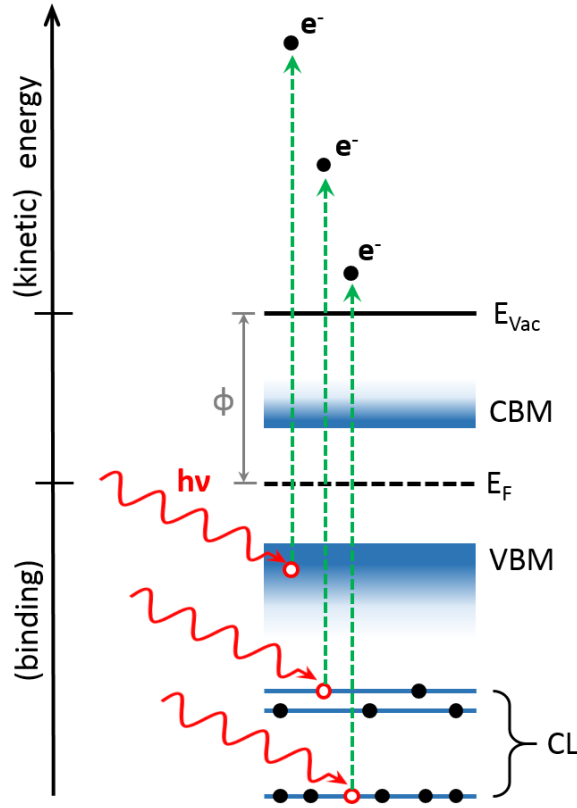


Figure 3.1.: Schematic energy-band diagram of a semiconductor showing the photoemission process. The incoming photon with energy $h\nu$ is absorbed by an electron and excited above the vacuum level. Leaving the semiconductor with a certain kinetic energy. The energy axis indicates the ranges of the kinetic and binding energy towards the vacuum and Fermi level, respectively.

a transmission rate [57].

In the end the kinetic energy of the detected electrons can be simply described by the following equation:

$$E_{\text{kin}} = h\nu - E_B - \Phi \quad (3.2)$$

Here E_B is the binding energy of the electron, $\Phi = E_{\text{Vac}} - E_F$ the work function with E_{Vac} and E_F being the vacuum and Fermi level respectively. $h\nu$ is the photon energy used for the excitation of the electron. Note that the binding energy of electrons is element specific, allowing the identification of chemical species and elements in a material on basis of reference materials.

For photoelectrons to leave the sample, an excitation energy $h\nu \geq E_B + \Phi$ is necessary. Depending on the kinetic energy of the electrons, information about the initial state can be retrieved. For a given $h\nu$, electrons with high kinetic energies originate from the valence band

3.2 Scanning Electron Microscopy(SEM) and Energy Dispersive X-ray Spectroscopy (EDX)

region or shallow core levels. Electrons that are more strongly bound, e.g., from core levels, have lower kinetic energy. This is schematically shown in Figure 3.1.

Photoelectron spectroscopy is a general term and can be divided into sub-categories depending on the source or sample probing environment. For example, PES techniques using photons in the UV range are called UPS (ultraviolet photoelectron spectroscopy) and an excitation energy of e.g., $h\nu = 21.2$ eV (He I) is used to study the valence band. If x-ray radiation is used it is called XPS (x-ray photoelectron spectroscopy), which can be further divided into XPS using Mg K_{α} ($h\nu = 1253.56$ eV) and Al K_{α} ($h\nu = 1486.58$ eV) for excitation and hard x-ray photoelectron spectroscopy (HAXPES) with $h\nu$ between 2 and 8 keV. In this thesis, also ambient pressure HAXPES (AP-HAXPES) is used to study the sample in ambient conditions (in this case, in an atmosphere of ≈ 15 Torr water vapor).

3.2. Scanning Electron Microscopy(SEM) and Energy Dispersive X-ray Spectroscopy (EDX)

Scanning Electron Microscopy (SEM) and Energy Dispersive X-ray Spectroscopy (EDX) deliver spatially resolved information about the sample surface.

SEM maps the spatially resolved surface morphology by scanning a focused electron beam (with an energy from 2-10 keV) over the sample and simultaneously detecting the emitting electrons from the surface. The incoming electrons interact with the sample and the emitted electrons from the surface can have various origins found in different energy ranges. Aside from elastically backscattered electrons, inelastic backscattered electrons which lost their energy due to plasmon excitation and interband transitions can be detected. These excitations are specific for every material or solid. Secondary electrons or the secondary background originates from electrons undergoing multiple scattering events on their way to the surface. Depending on the tuned energy range of the detector, a chemical composition with low resolution (by detecting backscattered electrons) or a topographical image with poor chemical composition (by detecting secondary background) can be mapped. The contrast or intensity of the image is determined by the interaction of the electrons with the material and is therefore material specific [57].

For a topography image with a good resolution and local chemical composition, SEM and EDX are combined. For recording EDX maps in the same set-up as SEM, the sample is again irradiated with an electron beam and fluorescence x-ray photons, which are element-specific and map the local chemical composition, are detected [58].

Note that SEM and/or EDX measurements recorded with an electron beam energy of a few keV always contain the risk of being influenced (or, in the worst case, dominated) by artifacts due to beam-induced alteration of the material properties. This is particularly true for organic or inorganic/organic hybrid materials such as perovskites, where the organic part can be quickly damaged by the high kinetic electrons. This risk can be reduced by limiting the exposure time of the probed sample area. Further, if comparison of the SEM and EDX data before and after measurements do not show any visible changes in the morphology and elemental distribution of the surface (e.g., due to beam exposure-induced decomposition), the measurements can be considered to be mainly free of electron beam induced artifacts, unless beam damage arises directly at the beginning of the measurements.

3.3. Photoelectron Emission Microscopy (PEEM)

Photoelectron Emission Microscopy (PEEM) is an alternative imaging method to SEM described in the previous section. In contrast to SEM, the sample surface is illuminated by photons, and electrons of different kinetic energies are emitted according to equation 3.2 and detected. The physics behind this technique are similar to XPS described in 3.1.

The sample surface is mapped by recording the photoemission from each point by means of a fluorescence screen in front of the imaging detector (here a CCD camera) [59, 60].

Further, X-PEEM can, in particular, be used to perform laterally-resolved and chemically sensitive x-ray photoelectron spectroscopy (XPS) and x-ray absorption spectroscopy (XAS) measurements, in microscopy mode, to reveal the chemical environment of the formed species. Making PEEM a full-field microscopy technique compared to SEM as an imaging technique with limited composition information. The energy resolution for the spectroscopy methods is realized by an energy filter (here an energy analyzer) positioned in front of the detector. For visualization, the contrast of each image according to the fulfillment of the energy conditions for a certain core electron is then determined (more details can be found in Refs. [59, 60]).

3.4. Data analysis

3.4.1. Curve Fit Analysis

Curve fit analysis is applied to XPS spectra, which were normalized to the background, to determine the intensity/area of the core levels as well as the chemical speciation. This involves fitting the peaks with Voigt functions, which are a convolution of the Lorentzian- and Gaussian

3.4 Data analysis

function. The convolution in spectroscopy is necessary to account for the natural (Lorentzian) and experimental (Gaussian) line broadening due to lifetime and experimental resolution, respectively. The fit analysis with Voigt functions is done by iterative fitting according to the least-squares methods using the fitting softwares Fityk [61] and Unifit 2016 [62]. The goal is to minimize the χ^2 value, which represents a quality feature of the fit. χ^2 is related to the residuum, which gives the difference between the fitted or simulated spectrum and the experimental measured spectrum (data). In Figure 3.2 an example of a Pb 4f fit displaying/explaining some of the fit related terms, mentioned in this subsection, is shown. Note that this is a simplified quantification, because the plasmonic loss structure known for Pb 4f, overlapping with the doublet peak at higher E_B , is not taken into account nor the satellites peaks appearing additionally in lab-based XPS, overlapping at lower E_B with the doublet peak.

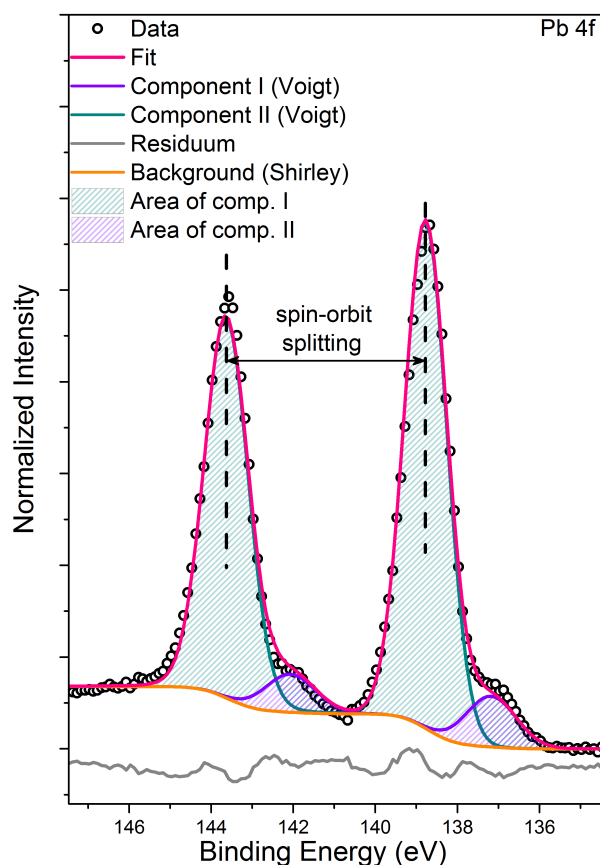


Figure 3.2.: Example fit of Pb 4f doublet including some fit related terms used in the text.

A reasonable physical interpretation of the curve fit analysis is obtained by adding additional constraints to the Voigt functions, e.g., accounting for the spin-orbit splitting of doublets by fixing the area ratio of the components according to the multiplicity $(2j+1)$, coupling the peak

Methods and Experimental Details

shape and width for every core level of the same element and subshell, and setting the spin-orbit split separation fixed according to literature values. The spectral background is usually fitted with a linear (Fityk) or Shirley (Unifit 2016) background. Detailed information of the constraining parameters and fitted background for curve fit analysis can be found in the respective data chapters. Note that for Unifit the coupling of the peak shape and width is not dynamic for batch processing of multiple spectra obtained from a measured series/sequence, and can only be fixed. In contrast, in Fityk the spectra can be fit "simultaneously". The batch processing in Unifit uses the same settings for every spectra and transferring all performed fitting steps of the active window (spectrum) to the following spectra. Nevertheless coupling of peaks of the same element, e.g., for different species, for a single spectrum is possible and dynamic.

For further analysis and interpretation of the intensity/area obtained from the fit, the excitation energy as well as the experimental geometry needs to be taken into account due to the fact that the photoionization cross section differs for every core level and excitation energy, and to take also the angular distribution of the photoelectrons within the electric dipole approximation into consideration [63, 64].

This is done by calculating the photoionization cross section of every core level (for a given excitation energy) for polarized or unpolarized x-rays from Ref. [63, 64] under consideration of the experimental geometry and normalizing the fitted area/intensity to it. For HAXPES measurements (performed at HiKE [BESSY II]) and AP-HAXPES (performed at the ALS) the geometry is as follows: the horizontally polarized x-rays irradiate the sample under (near) grazing incidence and the electrons are then emitted (near) normal to the sample surface. For the photoionization cross section calculation an angle of 90° is therefore assumed between polarization of the light and entrance of the analyzer. For lab-based XPS unpolarized x-rays the angle between source and analyzer is the "magic" angle of 54.7° where angle-dependent effects cancel out.

For the HAXPES data of CsSnBr_3 measured at $h\nu = 2$ keV the photoionization cross section for Sn $4d_{5/2}$, Br $3d_{5/2}$, Cs $4d_{5/2}$, F 1s and Ti 3p (Ti $3p_{3/2}$) can be directly calculated from Ref. [63, 64]. For the lab-based measurements of CsSnBr_3 , the photoionization cross section of F 1s and Sn $3p_{3/2}$ was determined from plotting the calculated photoionization cross section from Ref. [63, 64] over the excitation energy (500 - 5000 eV), leading for Al K_α to a photoionization cross section of (3.35 ± 0.01) kb ($= 10^{-21} \text{ cm}^2$) for F 1s and of (6.25 ± 0.01) kb ($= 10^{-21} \text{ cm}^2$) for Sn $3p_{3/2}$, respectively.

3.4.2. Inelastic Mean Free Path and Layer Thickness

Aside from the photoionization cross section, the distance that electrons can travel through a material without losing energy is also energy and material dependent and given by the inelastic mean free path (IMFP). Figure 3.3 shows this dependency of the IMFP over the kinetic energy displayed as a universal curve according Seah and Dench [65]. This curve reflects the general trend of IMFPs for different elements/materials and has a minimum (with lowest IMFP of ~ 0.4 nm) at ~ 40 eV. The shape arises from the competing elastic and inelastic scattering processes. Electrons with kinetic energies smaller than 40 eV are mainly elastically scattered, electrons with larger energies lose their energy through inelastic scattering.

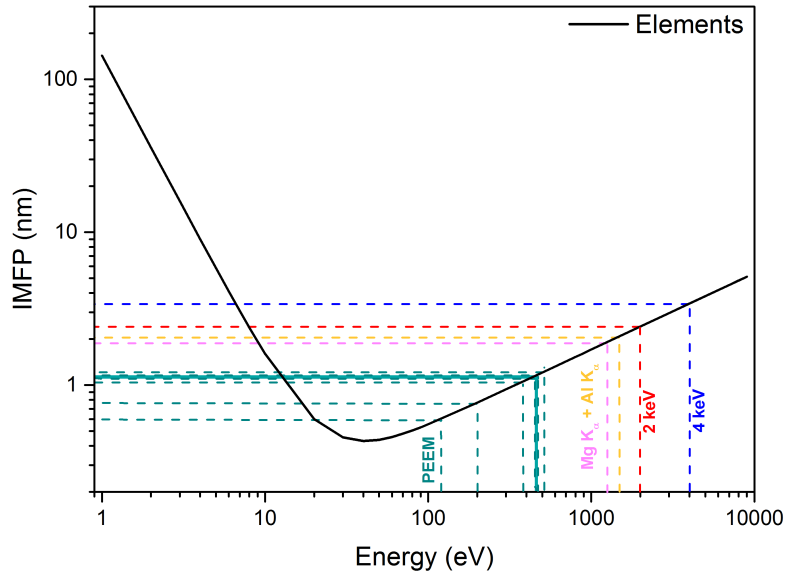


Figure 3.3.: Universal curve for pure elements according to Ref. [65], including the standard PES excitation energies used within this thesis and the different excitation energies used for PEEM.

The use of different excitation energies or different sample environments for photoelectron spectroscopy influences and results in different IMFPs for the same material according to the universal curve and therefore effects the intensity. The intensity in a XPS spectrum is limited by the IMFP of the respective photoelectron traveling from a distance d to the surface:

$$I(d) = I_0 e^{-\frac{d}{\text{IMFP}}} \quad (3.3)$$

Methods and Experimental Details

Note that equation 3.3 describes the intensity for the case that the analyzer is perpendicular to the sample surface. The actual maximum information depth for a material studied with XPS is approximated by 3 x IMFP, where 95% of the original intensity is exponentially attenuated, although the majority of the intensity ($I \sim 1/e$) originates from within one IMFP.

The material dependent IMFPs used in this thesis were calculated by using the QUASES IMFP TPP2M code [66] based on the formula from Tanuma et al. [67].

The relation described in equation 3.3 can be used to describe the attenuation of the intensity of an absorber or substrate material, when a cover layer with thickness d is grown on top. I_0 is then the intensity of the bare absorber/substrate.

The intensity increase for the cover layer on the other hand is described by the following formula:

$$I_{\text{cov}}(d) = I_{\text{ref}}^{\text{COV}} \cdot (1 - e^{-\frac{d}{\text{IMFP}}}) \quad (3.4)$$

With $I_{\text{ref}}^{\text{COV}}$ being the saturated intensity of a thick cover layer.

Both formulas 3.3 and 3.4 make the calculation of the thickness d for the cover layer possible by determining the intensity/area from the fits of the core level peaks and including the corresponding IMFP. I_0 and $I_{\text{ref}}^{\text{COV}}$ is then determined from the core level fits of a measured bare absorber/substrate (or in a close approximation) and a sample with a sufficiently thick cover layer.

3.4.3. Valence Band, Conduction Band, and Band Offset

The valence bands measured with HAXPES allow the determination of the valence band maximum (VBM) through an extrapolation of the leading edge, as shown in Ref. [68], and are always given with respect to the Fermi level E_F . Similar to the core levels, the VB/VBM values are influenced by the excitation energy through a change in photoionization cross section and IMFP.

The conduction band minima (CBM) presented in this thesis were not determined from measured CB spectra but rather estimated based on the determined VBM (from measurement) and band gap (E_G) values taken from literature, $\text{CBM} = \text{VBM} + E_G$. Ideally, CB spectra are measured by using inverse photoelectron spectroscopy (IPES) and the minimum is then determined through an extrapolation of the leading edge.

If now two materials, e.g., substrate (s) and cover layer (cov), which are differently doped (e.g., p- and n-doped) are joined together, their VBM and CBM position will change/be effected

3.5 Experimental Set-up and Details

and a heterojunction is formed with bent bands at the interface [interface induced band bending (iibb)]. How the bands align at the interface is determined by the interface and surface properties of the respective materials [69]. The band offset can have a positive or negative impact on the charge transport and therefore solar cell performance.

The valence band offset (VBO) and conduction band offset (CBO) for the substrate and cover layer material can be calculated from the VBM and CBM determined by the data analysis with

$$\text{VBO} = \text{VBM}_s - \text{VBM}_{\text{cov}} + \text{iibb} \quad (3.5)$$

$$\text{CBO} = \text{CBM}_s - \text{CBM}_{\text{cov}} + \text{iibb} \quad (3.6)$$

Note that iibb correction was not performed in this thesis due to a lack of appropriate data. For the calculation of the VBO and CBO a zero-order approximation was used assuming that $\text{iibb} \equiv 0$. Negative values of CBO describe a "cliff"-like alignment, positive values a "spike"-like alignment and zero CBO a flat band alignment, which is depicted in Figure 3.4

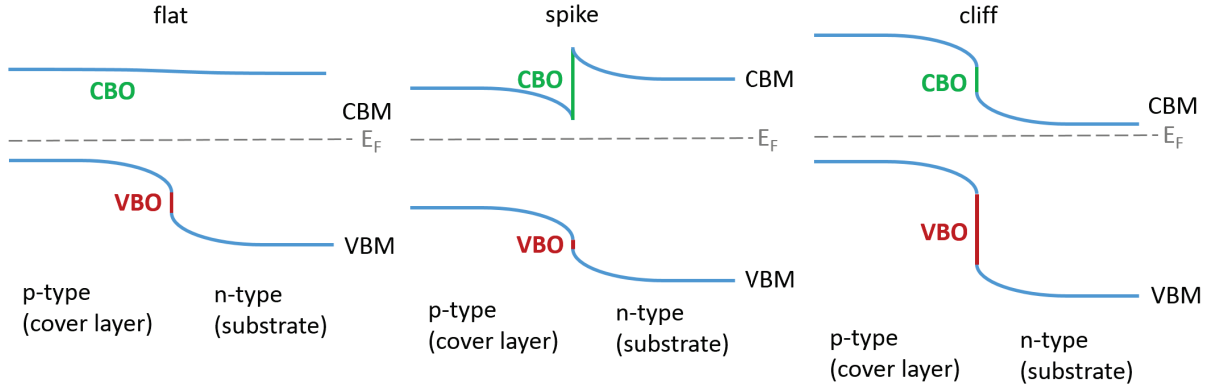


Figure 3.4.: Band alignment of a heterojunction interface for a flat, "spike"-like, and "cliff"-like CBO configuration.

3.5. Experimental Set-up and Details

3.5.1. Laboratory-based Techniques

The inorganic CsSnBr_3 samples were studied using a non-monochromatized Mg K_α and Al K_α source and the electrons were detected using a SPEC PHOIBOS 150 MCD-9 and Scienta Omicron Argus CU electron analyzer with a base pressure of the analysis chambers of $< 5 \times 10^{-10}$ mbar. All samples were measured under the magic angle and the electron analyzer SPEC

PHOIBOS 150 MCD-9 was calibrated according to Ref. [70]. The spectra were measured with a pass energy of the electron analyzer set to 30 eV which results, together with the resolution of the x-ray source, in a combined experimental resolution of ~ 1 eV. The survey spectra were always measured with a pass energy of 50 eV.

SEM images of the $\text{CH}_3\text{NH}_3\text{PbI}_{(3-x)}\text{Cl}_x$ sample surface were recorded using a commercially available Zeiss UltraPlus scanning electron microscope by measuring secondary electrons at a working distance of 47.8 mm and a primary electron beam acceleration voltage of 5 kV.

Energy dispersive x-ray spectroscopy (EDX) elemental distribution maps were acquired in the same microscope using an Oxford Instruments X-Max 80 X-ray detector and the AZtec acquisition and evaluation software. The beam energy and current were 7 keV and about 1 nA, respectively.

3.5.2. Synchrotron-based Techniques

Synchrotron Radiation

For most of the experiments conducted within the scope of this thesis, synchrotron radiation from two synchrotrons was used as a light source (i.e., excitation), the Berliner Elektronenspeicherring-Gesellschaft für Synchrotronstrahlung m.b.H (BESSY II) synchrotron in Berlin and the Advanced Light Source (ALS) in Berkeley. Both synchrotrons offer x-rays up to the hard x-ray regime, with an emphasis on the soft x-ray regime.

The generation of synchrotron radiation is based on the principle of relativistic electromagnetism, when electrons (or other charged particles) are accelerated to relativistic velocities/energies. First, electrons are produced by an electron gun and are then accelerated up to several MeV in a linear accelerator (Linac) through radio frequency (RF) cavities. Afterwards the electrons are injected into a booster synchrotron, where they are further accelerated, up to relativistic energies, by passing several times through a RF-cavity included in the ring of dipole magnets, keeping the electrons on a circular orbit, until they reached the desired end energy up to a few GeV and are injected into the storage ring. In the storage ring electrons are forced by bending magnets and different insertion devices on a curved trajectory, leading to a continuous radiation and loss of energy which is compensated by a RF-cavity.

The emitted radiation has a special radiation pattern. From electrodynamics it is known that accelerated charge behaves similar to the Hertzian dipole and emit electromagnetic waves. If the charge with a velocity v close to the speed of light c is kept by magnetic forces on a circular trajectory than radiation is emitted in a narrow collimated cone with an angle $\Theta \simeq \frac{1}{2\gamma}$ (see

3.5 Experimental Set-up and Details

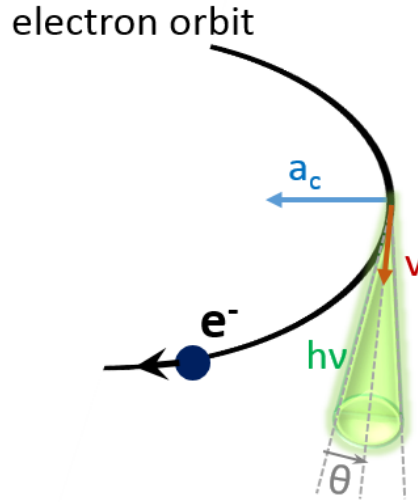


Figure 3.5.: Illustration of the radiation pattern of an electron moving with relativistic velocity v through a constant magnetic field. The electron is accelerated towards the center with a_c and is emitting the radiation in a cone with angle Θ tangential to the electron orbit. Scheme is adapted from Ref. [71].

Figure 3.5). With $\gamma = 1/\sqrt{1 - (\frac{v}{c})^2}$ being the Lorentzian factor contradicting the angle and therefore defining the shape as well as the direction of the radiation [71].

The emitted radiation of the electrons is collimated, and the resulting spectrum, when bending magnets are used, is continuous. In such a synchrotron spectrum the critical energy E_C is defined as the energy where half of the radiated power is in higher energy photons and the other half in lower energy photons [71]. The critical energy of the photons is always close to the maximum of the spectral distribution, making it a good characterization parameter for bending magnet radiation.

E_C is defined as follows [71]:

$$E_C = \frac{3ehB\gamma^2}{4\pi m} \quad (3.7)$$

where e is the charge, m the mass, h the Planck constant, B the magnetic flux of the bending magnet. The critical energy can be expressed with the electron energy E_e and $\gamma = \frac{E_e}{mc^2}$ to more practical units [71]:

$$E_C(\text{keV}) = 0.6650 \cdot E_e^2[\text{GeV}] \cdot B(\text{T}) \quad (3.8)$$

Methods and Experimental Details

E_C is a characteristic value for a specific storage ring, since for a given electron energy E_e , B is determined by the storage ring size (radius). For the synchrotrons used in this thesis electrons are accelerated in the storage ring up to 1.7 GeV (BESSY II) and 1.9 GeV (ALS), emitting light down to a critical energy of 1.9 and 2.4 keV, respectively. Similar dependent on E_e and B (radius) is the emittance ε , which describes a phase space product of the beam size and divergence. ε varies with normalized photon energy $\frac{E}{E_C}$.

So far bending magnets delivering continuous radiation were discussed. In synchrotrons also so called insertion devices, like undulators and wigglers are used for producing radiation with a characteristic spectrum. An undulator or insertion device in general consists of stacked permanent magnet arrays with alternating magnetic fields (see Figure 3.6 for more details).

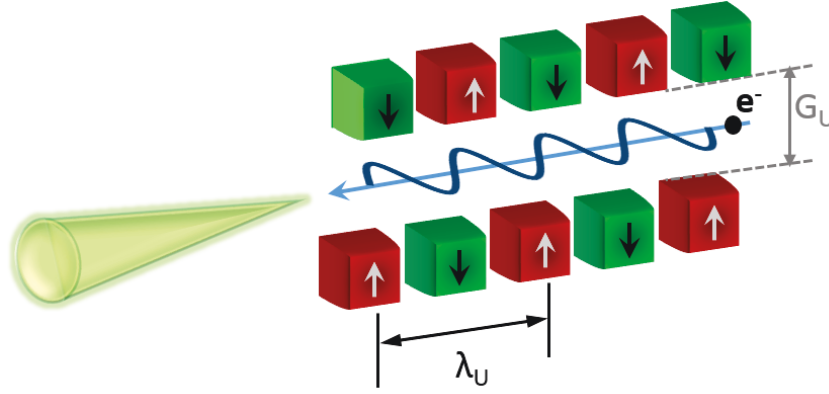


Figure 3.6.: Illustration of an insertion device with alternating polarity of permanent magnets. λ_U is the undulator period and G_U the undulator gap, which is the horizontal distance between the magnetic arrays. Scheme is adapted from Ref. [71].

An electron traveling through this periodic magnetic structure will be redirected in a way that it starts to oscillate, with a small amplitude for undulators and a larger amplitude for wigglers, and radiate. Depending on the conditions, which is described by K , the non-dimensional magnetic strength, the emitted cones can interfere constructively ($K = 1$), increasing the intensity of certain photon energies leading to intense lines in the resulting spectrum. This insertion device is then called an undulator. For a wiggler K needs to be $\gg 1$ resulting in a continuous spectrum similar to bending magnets, but with a higher photon flux.

The non-dimensional magnetic strength K is defined as follows [71]:

$$K = \frac{eB_0\lambda_U}{2\pi mc} = 0.9337 \cdot B_0[\text{T}] \cdot \lambda_U[\text{cm}] \quad (3.9)$$

with B_0 being the magnetic field and λ_U the undulator period.

3.5 Experimental Set-up and Details

The emitted photon energy of an undulator can be changed by changing the undulator gap G_U and therefore altering B_0 . For bending magnets and wigglers the use of monochromators allow the selection of the photon energy, for undulator sources monochromators are also used to improve resolution.

In the end the synchrotron radiation is guided through the beamlines to the endstation containing the experimental set-ups.

Endstations and Experimental Details

The PEEM characterization was performed in the Spectro-Microscope with Aberration correction for many Relevant Techniques (SMART) endstation installed at the UE49-PGM BESSY II beamline [59, 60]. The UE49-PGM beamline offers an excitation energy range of 100 to 1800 eV. The SMART endstation is equipped with an imaging energy analyzer allowing for spatially resolved studies of samples with in the best case a maximal spatial resolution of 18 nm and an energy resolution of 180 meV for X-PEEM. For these PEEM topography images an excitation energy of 510 eV was used.

The XPS measurements in microscopy mode (PEEM-XPS) were performed with a set photon energy by tuning the photoelectron kinetic energy detected by the analyzer through the energy range of interest. Spatially-resolved I 4d, Pb 4f, and extended valence band (i.e., shallow core level) XPS spectra were recorded in different areas of interest, using photon energies of 120, 380, and 200 eV, respectively. XAS spectra in microscopy mode (PEEM-XAS) are recorded by setting the kinetic energy detected by the electron analyzer to the range of the secondary electron induced maximum photoemission intensity [59] and tuning the photon energy through the energy range of interest (i.e., the absorption edge). To measure the Ti $L_{2,3}$ -edge XAS spectra, the photon energy was scanned from 450 to 470 eV.

The HAXPES measurement for CsSnBr_3 samples were performed with an excitation energy of $h\nu = 2$ keV at the HiKE endstation [72] of the KMC-1 BESSY II beamline [73]. The KMC-1 beamline offers an excitation energy range from 2 to 10 keV and the endstation is equipped with a Scienta R4000 hemispherical electron energy analyzer perpendicular to beam. Samples were measured near grazing incidence. The pressure in the analysis chamber was $< 1 \times 10^{-8}$ mbar. All spectra were measured with a pass energy of 200 eV, except survey spectra (500 eV). The excitation energy for the measurements were calibrated by measuring the Au 4f spectra of a clean gold foil and shifting the E_B of Au $4f_{7/2}$ to 84 eV. The resolution of the spectra is \sim

Methods and Experimental Details

0.25 eV, combining beamline and analyzer resolution.

The AP-HAXPES measurement for $\text{CH}_3\text{NH}_3\text{PbI}_{(3-x)}\text{Cl}_x$ samples were performed with an excitation energy of $h\nu = 4$ keV at the soft X-ray AP-XPS endstation of the ALS beamline 9.3.1. The beamline offers an excitation energy of 2.3 to 5.2 keV and the endstation is equipped with an Scienta R4000 HiPP-2 analyzer positioned normal to the sample surface [74]. The endstation offered the possibility to measure the sample in "vacuum" with a base pressure $< 2 \times 10^{-4}$ Torr and at ambient pressure of water vapor with a base pressure of > 14.5 Torr. All spectra were measured with a pass energy of 200 eV and the excitation energy was calibrated by measuring the Au 4f spectra of a clean gold foil and shifting the E_B of Au 4f_{7/2} to 84 eV. Note that the signal-to-noise ratio of the spectra is less for the measurements taken under ambient conditions due to the lower mean-free path λ_e of the electrons. For the illumination part of the experiment, the sample was additionally irradiated through a view port using a HAL-320 solar simulator from "Asahi Spectra" with a AM 1.5G filter.

4. Spatially-Resolved Characterization of the $\text{CH}_3\text{NH}_3\text{PbI}_{(3-x)}\text{Cl}_x/\text{TiO}_2$ Interface

Much of the content in this chapter has been published in:

- C. Hartmann, G. Sadoughi, R. Félix, E. Handick, H. W. Klemm, G. Peschel, E. Madej, A. B. Fuhrich, X. Liao, S. Raoux, D. Abou-Ras, D. Wargulski, T. Schmidt, R. G. Wilks, H. Snaith and M. Bär. "Spatially Resolved Insight into the Chemical and Electronic Structure of Solution-Processed Perovskites—Why to (Not) Worry about Pinholes". *Advanced Materials Interfaces* **2018**, 1701420. Copyright Wiley-VCH Verlag GmbH & Co. KGaA. Reproduced with permission. (Ref. [75])

Studies investigating the chemical and electronic properties of perovskite interfaces as found in perovskite solar cells are rare [53, 68, 76–79], and particularly so for spatially resolved analysis. This chapter focuses on a laterally-resolved investigation of the chemical and electronic properties of a wet-chemically deposited $\text{CH}_3\text{NH}_3\text{PbI}_{(3-x)}\text{Cl}_x$ thin-film on planar c- TiO_2 interface. The results were obtained by using scanning electron microscopy (SEM) and elemental distribution maps acquired by energy-dispersive x-ray spectroscopy (EDX) in combination with energy filtered photoemission electron microscopy (X-PEEM).

4.1. Results and Discussion

4.1.1. Morphology and Elemental Distribution Study by SEM and EDX

In the following subsection, SEM and EDX maps are discussed and used to gain first insight into coverage, morphology, and local elemental composition of $\text{CH}_3\text{NH}_3\text{PbI}_{(3-x)}\text{Cl}_x$ thin-films on

Spatially-Resolved Characterization of the $\text{CH}_3\text{NH}_3\text{PbI}_{(3-x)}\text{Cl}_x/\text{TiO}_2$ Interface

c-TiO₂, which were prepared according to 2.2.4. Figure 4.1 a) shows the SEM top-view image of the surface of a nominal 300 nm thick $\text{CH}_3\text{NH}_3\text{PbI}_{(3-x)}\text{Cl}_x$ layer on c-TiO₂. The brighter areas in the SEM image belong to the perovskite film, which does not completely cover the underlying compact c-TiO₂ substrate, and consists of large grains. The largest grains are seemingly a few μm in size. The incomplete coverage of c-TiO₂ substrates by the perovskite layers have already been reported in literature leading to concerns about shunting of the device (see subsection 2.2.1) [15, 80]. The exposed TiO₂ is visible in the SEM image as the darker areas that exhibit smaller grains/structures resembling the structure of a bare c-TiO₂ layer prepared on a FTO glass substrate [80].

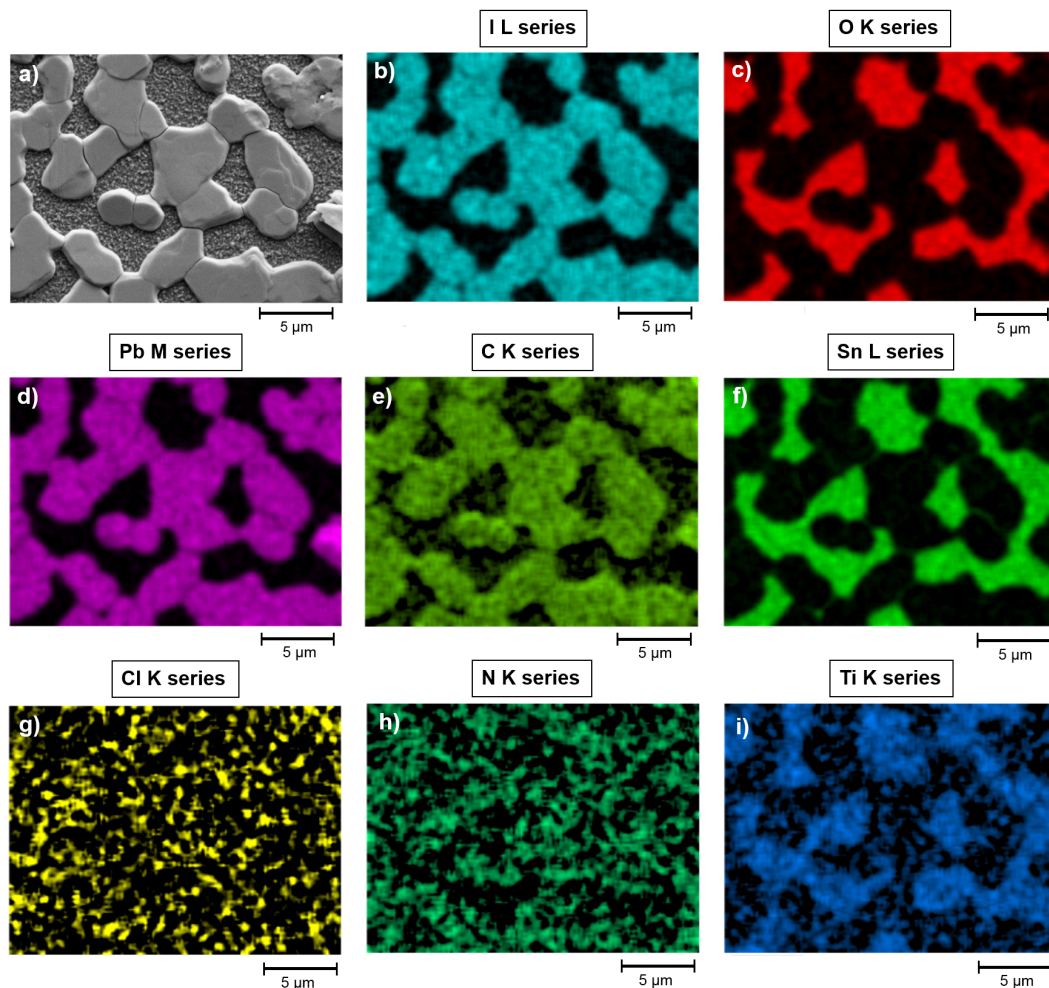


Figure 4.1.: SEM top-view image (a) and corresponding EDX maps of the I L (b), O K (c), Pb M (d), C K (e), Sn L (f), Cl K (g), N K (h) and Ti K (i) fluorescence of the same sample spot of a 300 nm thick $\text{CH}_3\text{NH}_3\text{PbI}_{(3-x)}\text{Cl}_x$ layer on c-TiO₂ on a FTO/glass substrate. Adapted from [75].

4.1 Results and Discussion

The attribution of the lighter (darker) areas to the perovskite (the TiO₂/FTO/glass substrate) is further confirmed by EDX elemental distribution maps shown in Figure 4.1 (b-i), measured in the same window as Figure 4.2. It can be clearly seen that the elements are inhomogeneously distributed. The O, Sn and Ti elements, associated with the substrate, have the highest concentration in the darker areas of the SEM image. Whereas I, Pb and C, associated with the perovskite, have the highest concentration located in the lighter areas. This shows that the distribution of O, Sn, Ti and I, Pb, C is therefore clearly anticorrelated, which supports the conclusion from the SEM image above that the perovskite does not completely cover the substrate. Note that the Sn signal stems from the FTO layer below the TiO₂. For the EDX maps in Figure 4.1 g) and h) based on the Cl K and N K fluorescence no conclusions can be drawn. The low Cl content in the sample seems to be the reason for the poorly resolved Cl K distribution map [53] and the N K signal partly overlaps with the Ti L fluorescence line, which makes a deconvolution and therefore a separation from the Ti L signal complicated.

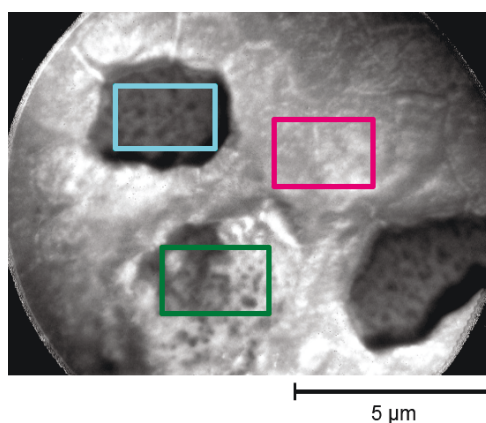


Figure 4.2.: PEEM image of a similarly prepared 300 nm thick CH₃NH₃PbI_(3-x)Cl_x layer on c-TiO₂ on a FTO/glass substrate. The field of view for the PEEM image is 12.4 μm. Different areas of interest are indicated by differently colored rectangular boxes. Adapted from [75].

Figure 4.2 shows the PEEM image of a similarly prepared sample to that used for the measurements in Figure 4.1 (a-i). The observed morphology is similar to that in the SEM image (see Figure 4.1 a)). Based on the discussion of the SEM and EDX data above, the topography in the PEEM image of the perovskite/TiO₂ sample shows three distinct regions, indicated in Figure 4.2 by differently colored rectangular boxes. The pink box denotes a sample area where the perovskite layer completely covers the TiO₂ substrate, which appears light grey in the PEEM image (hereafter called *perovskite*). The cyan box indicates a sample area in which the perovskite layer seems to not cover the substrate, leaving the c-TiO₂ exposed (hereafter, *exposed*

TiO_2) and appears dark grey in the PEEM image. Compared to the area in the cyan and pink boxes, the area defined by the olive green box reveals a more complex (hereafter, *intermediate*) topography, exhibiting a mixture of the area described by the other two boxes. For further detailed study of the chemical structure of the three different sample areas discussed above, local XAS and XPS spectroscopy (enabled by PEEM) was used.

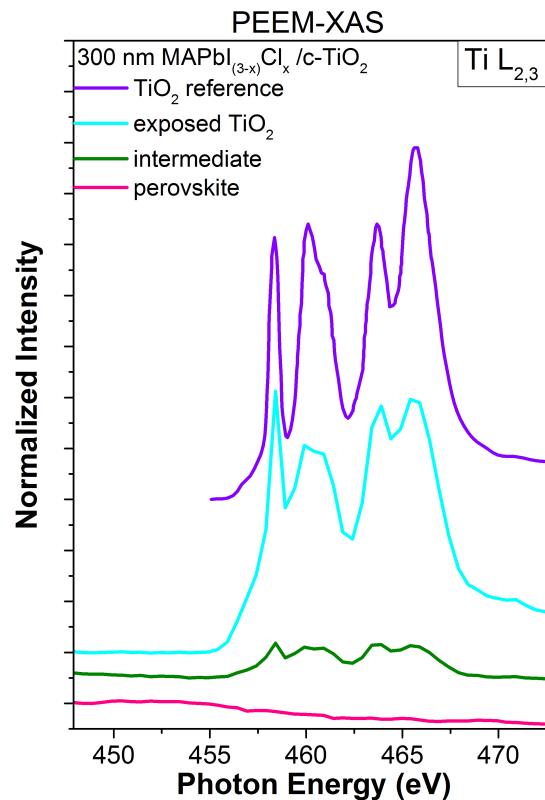


Figure 4.3.: PEEM-XAS spectra of the Ti $L_{2,3}$ -edge recorded in the three different areas of interest as defined in the PEEM image shown in Figure 4.2: *exposed* TiO_2 - cyan box; *intermediate* area - olive green box; *perovskite* - pink box. For comparison, a TiO_2 (anatase) reference spectrum digitalized from Ref. [81] is depicted in violet. Adapted from [75].

4.1.2. Chemical Structure Study by PEEM-XAS and -XPS

In this subsection, PEEM-XAS and PEEM-XPS data will be discussed to gain further insight into local coverage and chemical structure. PEEM-XAS was employed to study the local spatial distribution of Ti and (inversely) relate it to the coverage of TiO_2 by the perovskite layer. Figure

4.1 Results and Discussion

4.3 shows the Ti L_{2,3}-edge XAS spectra of the perovskite sample recorded in partial electron yield mode at the three areas of interest by measuring the secondary electrons while tuning the photon energy through the energy range of Ti L_{2,3}-edge. It can be clearly seen that no XAS Ti L_{2,3}-signal can be detected for the *perovskite* area [i.e., pink box in Figure 4.2]. This demonstrates that the TiO₂ substrate is completely covered by the perovskite layer in that area, as was already assumed from the SEM and EDX maps.

To estimate the thickness of the perovskite layer, the information depth has to be considered. The information depth of the PEEM-XAS measurements is limited by the inelastic mean free path (IMFP) of the detected photoelectrons, estimated to be in the range of around 3 nm, based on the IMFP universal curve [82] and taking into account that for the XAS measurements the electron analyzer is set to the kinetic energy of the secondary electrons (that induce maximum photoemission intensity) of only a few eV, the corresponding IMFP of these electrons include therefor multiple scattering in the material before their energy is reduced to only a few eV. It is further known that 95% of the exponentially attenuated signal originates from a "depth" of 3 x IMFP. Considering that leads to the conclusion that c-TiO₂, in the region defined by the pink box in Figure 4.2, is completely covered by the perovskite with an effective thickness of at least 9 nm (the nominal thickness is 300 nm).

For the *exposed TiO₂* area, which is indicated by the cyan box in Figure 4.2, an intense Ti L_{2,3} absorption signal can be observed, which resembles the XAS spectrum of a TiO₂ anatase reference [81]. The Ti L_{2,3} XAS reference data of anatase, which has been digitized from Ref. [81], is shown for comparison in Figure 4.3 as the violet spectrum. For a better comparison between data and reference, the PEEM-XAS data was shifted to higher photon energies by (2.91 ± 0.05) eV. The observed discrepancy (shift) in energy between reference and experimental PEEM-XAS data could be ascribed to energy miscalibration of the beamline. Aside from the shift, slight spectral differences between the Ti L_{2,3} XAS of the *exposed TiO₂* area and the reference are noticeable, which can be primarily explained by the significantly lower energy resolution and larger step size of 0.5 eV used in the PEEM-XAS data measurements. Similarly to the *exposed TiO₂* area, can also be a clear Ti L_{2,3}-edge XAS spectrum recorded for the *intermediate* sample area, indicated by the olive green box in Figure 4.2. The intensity of the olive green Ti L_{2,3} XAS spectrum is much less than the spectrum of *exposed TiO₂* (cyan in Figure 4.2), indicating an attenuation of the signal through coverage of the substrate. Since the signal is not completely attenuated, it can be again assumed that the sample area indicated by the olive green box in Figure 4.2 has a surface topography intermediate to that of the other two areas. This means for the *intermediate* sample area that the substrate is partially covered by the perovskite layer, but the coverage is either incomplete or thin enough (i.e., < 9 nm) so that a

Spatially-Resolved Characterization of the $\text{CH}_3\text{NH}_3\text{PbI}_{(3-x)}\text{Cl}_x/\text{TiO}_2$ Interface

Ti $L_{2,3}$ -signal from the exposed/underlying TiO_2 is still detectable. The spectral shape of Ti $L_{2,3}$ -edge XAS of the *intermediate* sample area also resembles the shape of the anatase TiO_2 reference, in a coarse comparison.

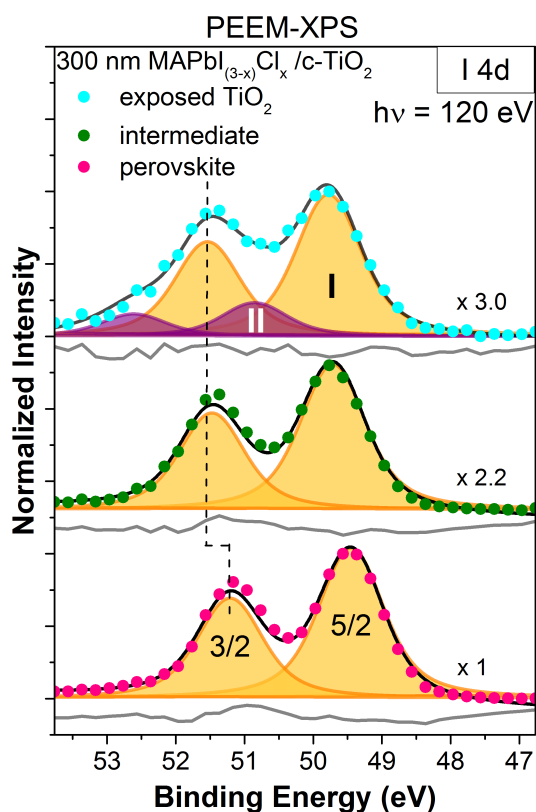


Figure 4.4.: PEEM-XPS I 4d detail spectra (including fit analysis) recorded in different areas of interest: *exposed TiO_2* - cyan box; *intermediate* area - olive green box; *perovskite* - pink box. The shown magnification factors were used to normalize the spectra to the maximum intensity of the perovskite area. Raw data is shown as solid circles and the resulting fits are given as black lines. The doublet peaks originating from the two iodine species are shown as shaded areas in orange (species I) and purple (species II). The corresponding residual of the fit is shown below each spectrum in gray. The spectral shift of the I $4d_{3/2}$ spin-orbit split component between the different spectra (areas of interest) is indicated with a vertical dashed line. Adapted from [75].

PEEM-XPS measurements were performed to gain more information on the chemical environment of the perovskite layer and its spatially inhomogeneous interface with c- TiO_2 . In Figure 4.4 the I 4d XPS spectra of the three areas of interest [as defined in Figure 4.2] is displayed and the I 4d photoemission line exhibits a spin-orbit split separation of 1.76 eV [83]. For all three

4.1 Results and Discussion

areas an I 4d XPS signal can be detected, with varying intensity as reflected by the different magnification factors. The magnification factors are indicated on the right side of Fig. 4.4 for every spectrum. The smallest I 4d XPS signal (see magnification factors) can be observed in the *exposed TiO₂* area [cyan box, Figure 4.2], which indicates in the absence of the perovskite layer (according to PEEM-XAS and EDX), that either an I-containing species is present at the substrate surface or I is incorporated into the upper region of TiO₂ substrate.

For further evaluation the measured XPS peaks were fitted by using the fitting program Fit-tyk [61] version 0.9.8. In order to determine the binding energy (E_B) of the core levels, a linear background was fitted to the spectra and Voigt profiles were used for the peaks. Additionally, the fit parameters were constrained by fixing the area ratio of the spin-orbit doublets correspondingly to the multiplicity ($2j+1$), setting the spin-orbit split separation fixed, and coupling the peak shape and width (i.e. Lorentzian and Gaussian) for every core level of the same element and subshell. The E_B axis of the PEEM-XPS data was calibrated with the help of an energy-calibrated data set (of similar prepared perovskites) measured at the High Kinetic Energy Photoelectron Spectrometer (HiKE) endstation installed at the KMC-1 beamline of BESSY II [72,73].

The shape and fits of the I 4d spectra reveal that using one spin-orbit split doublet for the I 4d spectra corresponding to the *perovskite* and *intermediate* areas seem to be sufficient. For the *exposed TiO₂* area, two spin-orbit split doublets are necessary to properly describe the shape of the spectra. This indicates the presence of multiple iodine chemical species (labeled as components I and II in Figure 4.4).

Table 4.1.: The E_B of the main (I) / secondary (II) contribution of the I 4d_{5/2} peak as measured for the *exposed TiO₂*, *intermediate* and *perovskite* areas designated in Figure 4.2

exposed TiO ₂	intermediate	perovskite
(49.78 ± 0.20) eV / (50.85 ± 0.20) eV	(49.71 ± 0.20) eV	(49.45 ± 0.20) eV

The curve fit results for the I 4d_{5/2} peaks are presented in Table 4.1. Note, that due to E_B calibration by means of a data set measured at a different experimental setup (HiKE), the here estimated experimental uncertainty on an absolute energy scale is rather large (± 0.20 eV). However, relative changes in E_B will have a significantly lower margin of error, as they will be equally effected by any calibration errors. The spectra in Figure 4.4 (and therefore the fit-derived E_B values) indicate a small shift [(0.3 ± 0.1) eV for the main contribution] of the I 4d line towards higher E_B values when going from the completely covered *perovskite* to the *exposed TiO₂* area (see dashed line in Figure 4.4). Comparing the obtained E_B values from the

Spatially-Resolved Characterization of the $\text{CH}_3\text{NH}_3\text{PbI}_{(3-x)}\text{Cl}_x/\text{TiO}_2$ Interface

fits (see Table 4.1) with E_B values of I-containing reference compounds found in literature [84] suggests that the main I 4d (I) contribution (at low E_B) can be attributed to I in an iodide/perovskite environment (i.e., $\text{CH}_3\text{NH}_3\text{PbI}_3$). By assuming further a homogeneous coverage of the TiO_2 substrate by the perovskite (for the sake of simplicity), the shift of this I 4d contribution to higher E_B with higher magnification factor (i.e., thinner cover layer), when comparing the spectra of the different topography regions, can be explained by (interface induced) band bending. Shifting of the core levels towards lower/higher E_B can reveal an upwards/downwards band bending at the interface.

As discussed above the $\text{CH}_3\text{NH}_3\text{PbI}_{(3-x)}\text{Cl}_x$ layer is thinner in the *exposed TiO_2* and *intermediate* sample area than in the *perovskite* area. The shifts can be therefore interpreted as being due to the formation of a downward band bending towards the TiO_2 , which would (in this case) accelerate electrons towards the substrate and repel holes, contributing to the perovskite/ TiO_2 contact's excellent charge selectivity [85].

The identification of the smaller I 4d (species II) contribution (at higher E_B) obtained from the fit is not straightforward. Because most reference data found in literature report on the more typical I 3d core level. So procedures were taken to derive the I 4d E_B from published I 3d E_B data in literature, which is discussed in the appendix A (see Figure A.1 for more details). Based on that, component II can be attributed to an iodite I^{+3} ($\rightarrow \text{IO}_2^-$) species. Note that this assignment is somewhat hypothetical and needs to be treated with caution, because this compound is unstable. Iodite I^{+3} does however exist as intermediate in iodide \leftrightarrow iodate reactions [86]. Considering additionally the uncertainty in the E_B interval transfer from I 3d to I 4d and the large (partially overlapping) E_B intervals, the possible formation of a hypoiodite I^{+1} ($\rightarrow \text{IO}^-$) and/or an iodate I^{+5} ($\rightarrow \text{IO}_3^-$) should also be taken into account. Since the I 4d E_B values for different iodine compounds found in literature are scarce, no unambiguous identification of species II, based on the measurements presented here, can be done. Hence, this compound will be referred to as "oxidized" iodine species in the following.

The detected "oxidized" iodine species in the *exposed TiO_2* area could be explained by the formation of I-O bonds at the perovskite/ TiO_2 interface, whose origin can be understood by considering the preparation procedure of the perovskite (see also subsection 2.2.4). Before the crystallization annealing step the degree of coverage of the perovskite precursor layer on the compact TiO_2 is significantly higher [87]. After the annealing step, some areas of the TiO_2 which have been covered with perovskite precursor solution, become exposed and reveal therefore the remaining perovskite/iodite "seed layer." From the fits a composition ratio between the

4.1 Results and Discussion

two iodine species can be derived, which in the *exposed TiO₂* sample area for I:II is approximately 4:1. Note, that iodine species I is perovskite and species II is "oxidized" iodine. For the other areas only one iodine species was derived from the fits, which doesn't exclude the presence of the "oxidized" species in these areas at the interface. The perovskite layer is just too thick to allow probing of the perovskite/TiO₂ region with PEEM-XPS. The I 4d photoelectrons excited with 120 eV have only an IMFP of approximately 0.5 nm [66, 67].

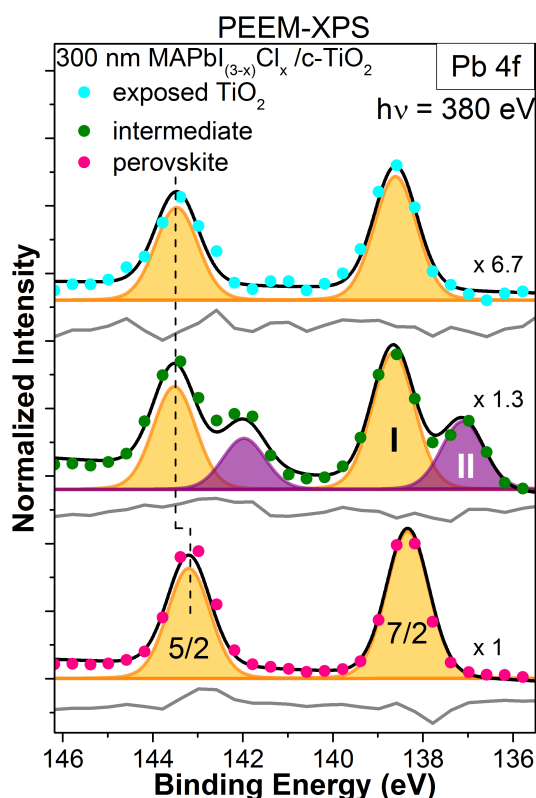


Figure 4.5.: PEEM-XPS Pb 4f detail spectra (including fit analysis) recorded in different areas of interest [as defined in the PEEM image of Figure 4.2]: *exposed TiO₂*, *intermediate* area, *perovskite*. The shown magnification factors were used to normalize the spectra to the maximum intensity of the perovskite area. Raw data is shown as solid circles and the resulting fits are displayed as black lines. The doublet peaks originating from the two Pb species are shown as shaded areas in orange (species I) and purple (species II). The corresponding residual of the fit is shown below each spectrum in gray. The spectral shift of the Pb 4f_{5/2} spin-orbit split component between the different spectra (areas of interest) is indicated with a vertical dashed line. Adapted from [75].

A similar investigation of the chemical environment of Pb with PEEM-XPS was performed.

Spatially-Resolved Characterization of the $\text{CH}_3\text{NH}_3\text{PbI}_{(3-x)}\text{Cl}_x/\text{TiO}_2$ Interface

Figure 4.5 shows the Pb 4f XPS detail spectra (including curve fit analysis) recorded in the three different areas of interest [see Figure 4.2]. The Pb 4f photoemission line exhibits a spin-orbit split separation of 4.86 eV [88]. Similar to I, Pb is detected in all three regions of interest in varying amounts (which is reflected by the magnification factors on the right side of Figure 4.5).

The fit parameters of the Pb $4f_{7/2}$ peaks are presented in Table 4.2, indicating only one doublet peak contribution for *exposed TiO₂* (cyan spectrum in Figure 4.5) and the *perovskite* (pink spectrum in Figure 4.5) areas. Further, from the Pb 4f spectra and the fit derived E_B values a shift between the *exposed TiO₂* and *perovskite* areas can be observed, which is in agreement with the shift observed in the I 4d energy region. The shift can again be explained by interface induced band bending (see discussion above for I 4d). The Pb 4f XPS spectrum of the *intermediate* area (olive green spectra in Figure 4.5) reveals the presence of two different chemical Pb species; the corresponding peaks are clearly separated. For the other two areas (*perovskite* and *exposed TiO₂*) only one Pb 4f doublet can be observed and is similar to the main (I) Pb component of the *intermediate* area attributed to Pb in a perovskite environment [84]. The additional (minor) Pb contribution II (i.e., at the lower E_B side) in the *intermediate* area (olive green spectra in Figure 4.5) can be ascribed to metallic Pb. The perovskite (I) to metallic Pb (II) ratio is determined from the fits to be approximately 2:1.

Table 4.2.: The E_B of the main (I) / secondary (II) contribution of the Pb $4f_{7/2}$ peak as measured for *exposed TiO₂*, *intermediate*, and *perovskite* areas designated in Figure 4.2

exposed TiO ₂	intermediate	perovskite
$(138.61 \pm 0.2) \text{ eV}$	$(138.66 \pm 0.2) \text{ eV}/(137.11 \pm 0.2) \text{ eV}$	$(138.34 \pm 0.2) \text{ eV}$

Although we ascribed so far the main (I) component of the I 4d and Pb 4f core levels to perovskite, it should be considered that we cannot distinguish between $\text{CH}_3\text{NH}_3\text{PbI}_3$ and PbI_2 , based on the energy resolution of the here presented I 4d and Pb 4f spectra. Since both species exhibit for I and Pb very similar E_B values [89]. Therefore a contribution of PbI_2 to the Pb 4f spectrum cannot be completely ruled out. This can be further evaluated by using the magnification (scaling) factors given in Figure 4.4 and 4.5 to form ratios of I 4d / Pb 4f. Note that the scaling factors were determined by adapting the main (I) component of the respective XPS spectra to cover the same area as the main (I) component of the spectra correlated to the *perovskite* area for the same photoemission line. Additionally, it should be kept in mind, that larger scaling factors imply stronger magnification of the small areas in comparison to each other. Further, consider that for the *intermediate* and *exposed TiO₂* areas of Pb 4f and I 4d,

4.1 Results and Discussion

respectively, additional contributions (II) exists. The factor ratios are in these cases under- and overestimated, respectively.

For the *perovskite* area a scaling factor ratio of 1 / 1, for the *intermediate* area a scaling factor ratio of 2.2 / 1.3 (i.e. I/Pb < 1) and for the *exposed TiO₂* area a scaling factor ratio of 3.0 / 6.7 (i.e. I/Pb > 1) is obtained. Therefore it can be concluded that, relative to the I/Pb ratio of the *perovskite* area, the *intermediate* sample area is I-poor or Pb-rich, which could be explained by the existence of PbI₂ in that area. Whereas the *exposed TiO₂* sample area is I-rich or Pb-poor, which might indicate the diffusion of iodine into the TiO₂ substrate.

This conclusion is further supported by the fact that I is a well-known dopant in TiO₂, in particularly for photocatalytic applications [90], with nominal doping levels up to 15 wt% [91]. The I-O-I and I-O-Ti bonds that are proposed to result from the incorporation of I into the TiO₂ structure [92] are so far in agreement with the here presented results; as they are consistent with the attribution of the high E_B component (II) of the I 4d line to an "oxidized" I species (see discussion above and Figure 4.4). Though it needs to be kept in mind, that XPS data of I-doped TiO₂ usually reports the dopant-related I 4d lines at even higher E_B values [90–92], indicating that I in literature is present in higher oxidation states than in this case.

Figure 4.5 indicated in the *intermediate* area the presence of metallic Pb as the second species, which has been already observed in perovskites [76] and will be now further discussed. Recently, the presence of metallic Pb has been related to x-ray induced degradation of the perovskite [17]. Perovskites degrade i.a. in vacuum under visible light (24 h exposure) into metallic Pb and PbI₂ [19] (see also subsection 2.2.2 for further details). For the PEEM-XPS measurement, all areas of interest on the sample were irradiated equally and simultaneously by x-rays. But metallic Pb is only detected in the *intermediate* area. Additionally indicates the scaling factor ratio discussion (see previous paragraph) that in the *intermediate* area PbI₂ is formed. Under the assumption, that the formation of metallic Pb, which is likely formed together with PbI₂, is indeed a x-ray photon-induced effect. These results then suggest that the formation (of metallic Pb) starts or appears only locally and is affected by laterally varying composition.

Next, the region of the shallow core levels is examined. Additionally to the valence band maximum (VBM), the investigated/measured energy range includes the Ti 3p, O 2s and Pb 5d lines and are shown in Figure 4.6 a) for the three areas of interest. Although a significantly lower signal-to-noise ratio is achieved for the shallow core levels than for the narrower I 4d and Pb 4f detail spectra, the spectra in Figure 4.6 a) confirm the topography and chemical structure related to the findings discussed above. The spectrum of the *exposed TiO₂* area [cyan spectrum in Figure 4.6 a)] shows explicitly three main spectral features that can be attributed to the O 2p

Spatially-Resolved Characterization of the $\text{CH}_3\text{NH}_3\text{PbI}_{(3-x)}\text{Cl}_x/\text{TiO}_2$ Interface

derived valence band states in the VBM, to O 2s at a E_B of ≈ 23 eV, and to Ti 3p at a E_B of

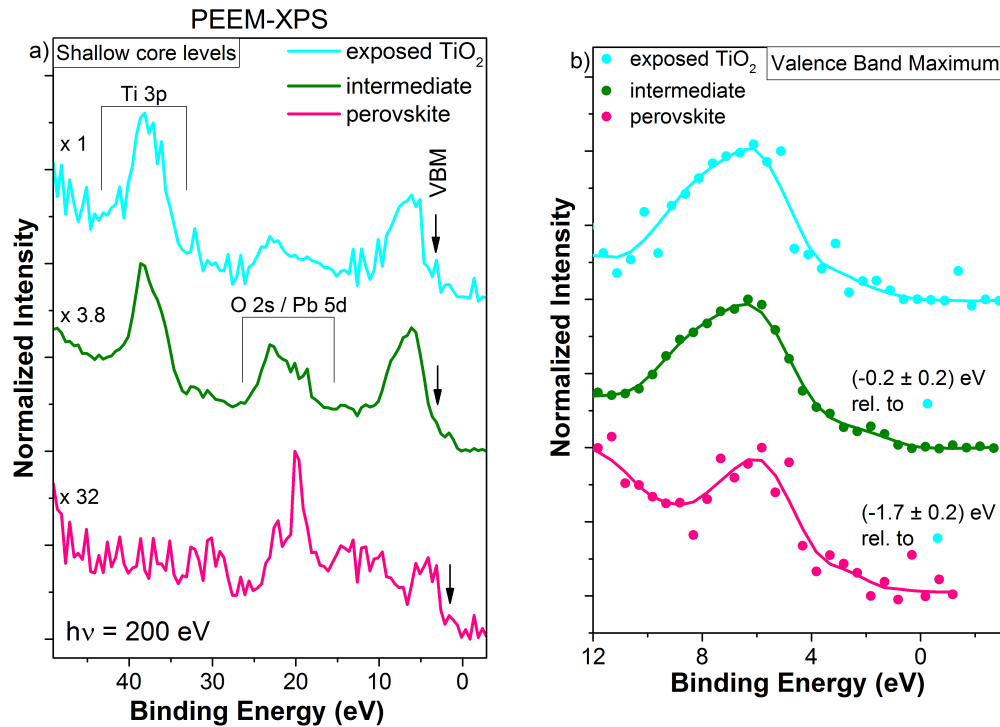


Figure 4.6.: PEEM-XPS spectra of the shallow core levels and valence band region of the different areas of interest [as defined in the PEEM image of Fig. 4.2]: *exposed TiO₂*, *intermediate* area, *perovskite*. The shown magnification factors were used to normalize the spectra to the maximum intensity of the VB of the exposed TiO₂ area. The shallow core level lines are labelled and the positions of the valence band maxima (VBM) are indicated by arrows. Adapted from [75]. Figure 4.6 b) shows the zoom in of the valence band region including the relative shift of the VBM to the VBM of the *exposed TiO₂*.

≈ 38 eV. The O 2s and Ti 3p signals that can be detected in the shallow core levels originate from the TiO₂ substrate. The Pb 5d signal, which is expected at an E_B of ≈ 21 eV, seems to be absent. This is accounted to the low signal-to-noise ratio, mentioned above, and the partially overlap with the O 2s, preventing the Pb 5d line from being clearly resolved. Nevertheless, the presence of Pb (most likely as a perovskite) in the *exposed TiO₂* sample area is clearly displayed by the Pb 4f signal (see Figure 4.5). The shallow core levels of the *perovskite* area [pink spectrum in Figure 4.6 a)] shows a clear Pb 5d doublet peak and the VB(M) of the perovskite, which is formed by hybridized Pb 6s and I 5p states [79]. Here, the perovskite layer is sufficiently thick to completely attenuate (within the signal-to-noise ratio of the background) the Ti

4.1 Results and Discussion

3p photoelectrons. For the spectrum of the *intermediate* area [olive green spectrum in Figure 4.6 a)] signals from the VB(M) and all expected shallow core levels (i.e., Pb 5d, O 2s, and Ti 3p) can be observed, corroborating an intermediate layer topography/thickness state. Note that the photoionization cross section for the Ti 3p line at this excitation energy ($h\nu = 200$ eV) is higher by a factor of about 24 than that of the Pb 5d line [63, 64], which explains some of the intensity difference that can be observed and is visualized by the magnification factors in Figure 4.6.

The strong Ti 3p signals in the cyan and olive green spectra [Figure 4.6 a)] indicate that the film in the *exposed* TiO_2 area is very thin. The thickness of the film in this area can be estimated by correlating the ratio of the scaling factors of Pb 4f (see Figure 4.5) for the *perovskite* and *exposed* TiO_2 area to an exponential intensity decrease of Pb with decreasing coverage of TiO_2 , assuming complete coverage for *exposed* and using the inelastic free mean path value of 0.87 nm of PbI_2 for an approximation [66, 67]. This results in a thickness of about 0.14 nm, which is smaller than the lattice constant of 0.64 nm for $CH_3NH_3PbI_3$ [93] and, thus, less than a monolayer of perovskite.

4.1.3. Electronic Structure

The PEEM-XAS and XPS results collected so far allow, furthermore, to get spatially resolved insights into the electronic structure at the $CH_3NH_3PbI_{(3-x)}Cl_x/TiO_2$ interface, to help explain how perovskite devices, despite exhibiting severe pin-hole densities can nevertheless result in working solar cells.

It has been reported in literature that the poorer performance of planar thin-film configurations may arise from pin-hole formation through incomplete coverage of the perovskite layer, resulting in less light absorption (limiting the current) and presumably low-resistance shunt paths (limiting the voltage) (see also subsection 2.2.1). Through the formed pin-holes, the HTM and ETM may come in direct contact, resulting in recombination paths for electrons and holes [14]. Recently, to prevent the formation of such shunting paths a transparent, insulating blocking layer preferably deposited on the uncovered ETM was introduced into the device structure [43]. As a result, the open circuit voltage was enhanced without deteriorating charge extraction.

The VBM positions, marked in Figure 4.6 a) by arrows, have been derived by shifting the VB of the *intermediate* and *perovskite* area to the VB of the *exposed* TiO_2 and make them overlap.

Spatially-Resolved Characterization of the $\text{CH}_3\text{NH}_3\text{PbI}_{(3-x)}\text{Cl}_x/\text{TiO}_2$ Interface

To better guide the shift, making the leading edge of the VB overlap, the data points have been smoothed using the Loess function in Origin Pro 9.2 [see solid lines in Figure 4.6 b)]. The states between the VBM and Fermi level in Figure 4.6 b) can be associated with metallic Pb [76], but metallic Pb can only be seen for the *intermediate* area in the Pb 4f spectra. Considering the significant appearance of these states in all three areas and the absence of the metallic Pb signal in the Pb 4f spectra in two areas, a different origin of these states is more likely. Because of the PEEM-XPS energy scale calibration (see subsection 4.1.2) and due to the low-signal-to noise ratio only relative instead of absolute VBM positions are discussed in the following. The VBM values of the *intermediate* and *perovskite* sample areas is shifted by (-0.2 ± 0.2) eV and (-1.7 ± 0.2) eV closer to the Fermi level (E_F), respectively, compared to the VBM of the *exposed TiO₂*. As discussed already above, the shallow core level region of the *intermediate* sample area is dominated by TiO₂ signals with minor Pb 5d attributed contributions [see Figure 4.6 a)]. Therefore, also the VBM position of the *intermediate* sample area is dominated by the O 2p states of the VB of the TiO₂. The small VBM shift of the *intermediate* compared to the *exposed TiO₂* area is ascribed to some marginal spectral intensity in the VB towards E_F , which is probably caused by hybridized Pb 6s and I 5p states originating from the perovskite/iodite layer. The low signal-to-noise level of the PEEM-XPS measurement prevents the linear extrapolation approach to properly account for this low-intensity signal.

For further discussion of the VBM shifts between the *exposed TiO₂* and *perovskite* area, it is assumed that the *exposed TiO₂* VBM represents the electronic structure of bare TiO₂. Regardless of the fact that I- and Pb-related XPS signals have been determined in this sample area (see Figures 4.4 and 4.5). The so observed VBM shift with respect to the *perovskite* would then to some extent describe the VB offset (VBO) at the $\text{CH}_3\text{NH}_3\text{PbI}_{(3-x)}\text{Cl}_x/\text{TiO}_2$ interface. Note that this assumption is justified by the significantly lower (factor of 4) photoionization cross sections of the Pb- and I-derived states compared to the O-derived VB states. Furthermore, in order to obtain the true VBO from the data presented here, the observed VBM shifts needs to be corrected by the interface induced band bending (iibb).

Despite the neglected iibb correction, the VBM difference between the *perovskite* and the *exposed TiO₂* sample area of (-1.7 ± 0.2) eV is in good agreement with the -1.86 eV VBO value reported by Schulz et al. [68] for the $\text{CH}_3\text{NH}_3\text{PbI}_{(3-x)}\text{Cl}_x/\text{TiO}_2$ interface.

Next, the relative energy position of the conduction band minimum (CBM) for the *exposed TiO₂* and *perovskite* areas are estimated, by using the electronic band gaps of $\text{CH}_3\text{NH}_3\text{PbI}_{(3-x)}\text{Cl}_x$ (1.7 eV) and TiO₂ (3.3 eV) reported by Schulz et al. [68] (measured by

4.1 Results and Discussion

combining ultraviolet and inverse photoemission spectroscopy). The resulting relative VBM and CBM positions are schematically illustrated in Figure 4.7 and show that the CBM position at the surface of the *exposed TiO₂* and *perovskite* sample areas are almost aligned. Again assuming that the measurement of the *exposed TiO₂* represents the properties of the bare TiO₂ substrate, and neglecting the potential impact of iibb, this zero-order approximation suggests that no significant CB offset (CBO) is formed at the CH₃NH₃PbI_(3-x)Cl_x/TiO₂ interface.

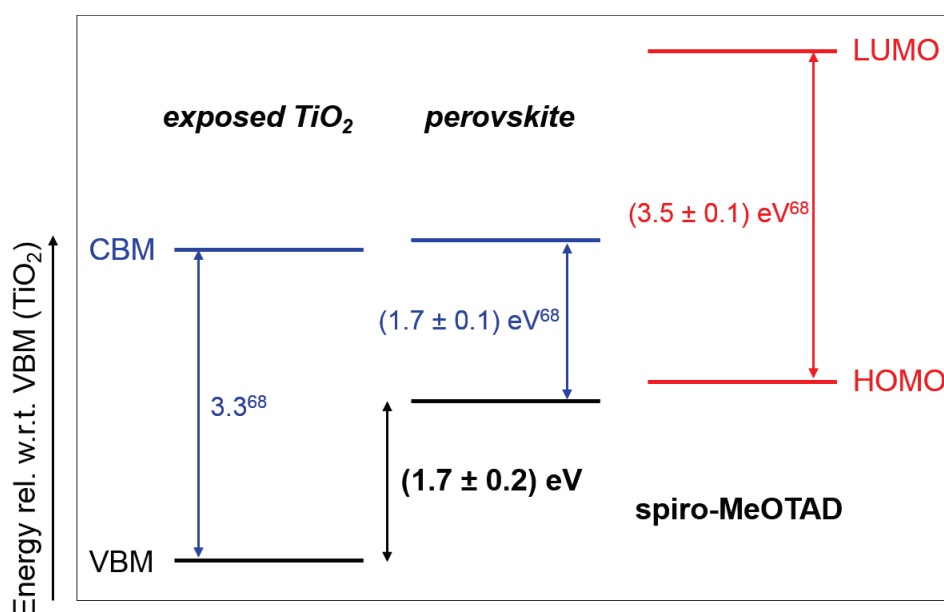


Figure 4.7.: Schematic presentation of the relative difference between the PEEM-XPS derived VBM positions of the *exposed TiO₂* and *perovskite* sample area surface (black lines). The CBM positions (blue lines) were approximated by using the electronic band gap values for TiO₂ (3.3 eV) and CH₃NH₃PbI_(3-x)Cl_x (1.7 eV) reported by Schulz et al. [68] For comparison of the electronic structure of a prominent ETM (TiO₂) with that of a prominent HTM (spiro-MeOTAD), the energy level scheme of a spiro-MeOTAD (red lines) was also taken from Ref. [68] and aligned according to the reported energy difference between the VBM position of CH₃NH₃PbI_(3-x)Cl_x and the HOMO of spiro-MeOTAD. All values are given in eV and the experimental uncertainty of the stated VBM shift between the *exposed TiO₂* and *perovskite* sample area is ± 0.2 eV. Adapted from [75].

However, in the discussion related to the Figures 4.4 and 4.5, a shift of (0.3 ± 0.1) eV of the I 4d and Pb 4f lines to higher E_B values has been observed when going from the completely covered *perovskite* to the *exposed TiO₂* sample area and was interpreted as being indicative for a downward band bending in the perovskite towards the TiO₂ interface. The aligned CB would then change into a small spike-like CBO [i.e., CBM (CH₃NH₃PbI_(3-x)Cl_x) > CBM (TiO₂)]

Spatially-Resolved Characterization of the $\text{CH}_3\text{NH}_3\text{PbI}_{(3-x)}\text{Cl}_x/\text{TiO}_2$ Interface

configuration. At the same time, the VB difference of (-1.7 ± 0.2) eV needs to be iibb corrected (by the shift of the I 4d and Pb 4f lines), resulting in a true VBO of (-1.4 ± 0.2) eV. In any case, the electronic interface structure of the $\text{CH}_3\text{NH}_3\text{PbI}_{(3-x)}\text{Cl}_x/\text{TiO}_2$ layer stack would still result in an ideal charge selective contact. The large barrier in the VB is sufficient to effectively block holes. Furthermore, the downward iibb of the perovskite towards the ETM TiO_2 will repel holes from the the $\text{CH}_3\text{NH}_3\text{PbI}_{(3-x)}\text{Cl}_x/\text{TiO}_2$ interface and accelerate electrons toward it. Even in the case that a small spike-like CBO is formed at the interface, it is not expected to be a significant hindrance for electron transport. This assumption is based on device simulations [94, 95] for chalcopyrite-based solar cells, which have shown no detrimental impact on device performance for a positive CBO of up to $+(0.3 - 0.4)$ eV. A spike-like CBO for the perovskite/ TiO_2 interface will actually result in an enhancement of the interface band gap [96]:

$$E_{g,i}(\text{CH}_3\text{NH}_3\text{PbI}_{(3-x)}\text{Cl}_x/\text{TiO}_2) = E_{g,\text{perovskite}} + \text{CBO} = \text{CBM}_{\text{TiO}_2} - \text{VBM}_{\text{perovskite}},$$

which presents the energetic barrier for charge carrier recombination across the interface.

In order to address the question whether the observed limited ETM coverage by the perovskite layer (i.e., the formation of pin-holes) will result in low-resistance shunt paths due to creation of direct recombination paths for electrons and holes [14] that are limiting efficiency [15], the derived electronic structure of the *exposed* TiO_2 to that of the most prominent HTM (spiro-MeOTAD) will be discussed in the following. Note that the energy level scheme found for the spiro-MeOTAD surface in Ref. [68] is aligned to the measurements presented here by using the reported relative shift between the VBM of $\text{CH}_3\text{NH}_3\text{PbI}_{(3-x)}\text{Cl}_x$ and the highest occupied molecular orbital (HOMO) of spiro-MeOTAD of 0.2 eV [68].

For a zero-order approximation (i.e., neglecting any impact of iibb on the electronic structure of the spiro-MeOTAD/ TiO_2 interface), Figure 4.7 indicates that there are significant energetic barriers (on the order of 2 eV) between spiro-MeOTAD HOMO and TiO_2 VBM as well as between the spiro-MeOTAD lowest unoccupied molecular orbital (LUMO) and TiO_2 CBM that would effectively avoid any direct charge carrier transport between HTM and ETM [97]. This explains why solar cells based on perovskites deposited by low-cost methods (e.g., spin-coating) on planar TiO_2 still result in working solar cells, despite the formation of pin-holes via which the HTM can directly contact the ETM. Nevertheless, the resulting interface band gap, i.e.,

$$E_{g,i}(\text{spiro-MeOTAD}/\text{TiO}_2) = \text{CBM}_{\text{TiO}_2} - \text{VBM}_{\text{spiro-MeOTAD}} \quad (4.1)$$

is probably smaller for the real device than that discussed for the perovskite/ TiO_2 interface

4.1 Results and Discussion

above. Hence, the rate/probability of charge carrier recombination at the spiro-MeOTAD/TiO₂ interface is likely to be enhanced, which would then limit the open circuit voltage. This interpretation can be further corroborated by the observed improvement in open circuit voltage through introduction of a shunt-blocking layer into the device [43],

4.1.4. Summary

A combination of different spectroscopic tools was used to spatially-resolved investigate the surface of a nominal 300 nm thick CH₃NH₃PbI_(3-x)Cl_x layer deposited on (c-) TiO₂ FTO/glass. The complementing SEM, EDX, PEEM-XPS and PEEM-XAS study displays an inhomogeneous morphology of the surface, with an incomplete coverage of the substrate by the perovskite. The perovskite layer consists of holes that seemingly reach to the substrate. From the spatially-resolved XPS measurements the presence of Pb and I in the *exposed TiO₂* area is revealed, which could not be resolved with EDX maps of the same sample type. This finding suggests that perovskite remnants are present and/or the formation of a Pb-I(-O) containing seed/interface layer on the TiO₂ substrate. Further evidence of the formation of metallic Pb and an enhanced iodine-oxidation in the proximity of the perovskite/c-TiO₂ interface were observed. Depending on the degree of coverage, different chemical compositions which cause an inhomogeneity of the absorber material is found, which is also reflected in the electronic structure. By associating the spatially-resolved VBM values determined from PEEM-XPS data and CBM values from literature, it was outlined that the energy level alignment at the HTM/perovskite and perovskite/ETM interfaces correlate to the performance level of respective solar cells. Furthermore, it is shown that the HTM (here: spiro-MeOTAD)/perovskite and the perovskite/ETM (here: TiO₂) junctions are (almost) ideal charge selective contacts for holes and electrons, respectively. In addition, the estimated energy level positions in the pin-hole areas, i.e. where the HTM and ETM can come into direct contact, reveal a sufficient high energetic barrier for avoiding high rate charge carrier recombination and which therefore allows the solar cell devices to function even with high pin-hole densities.

5. In-situ Study and Characterization of Environmental Impact on Mixed Halide Perovskite Absorbers

This chapter focuses on studying the change of the chemical properties of nominal 60 and 300 nm thick $\text{CH}_3\text{NH}_3\text{PbI}_{(3-x)}\text{Cl}_x$ absorber on c-TiO₂ under realistic environmental conditions leading to degradation. The degradation process itself is not completely understood and many papers declaring different degradation pathways under different conditions in literature can be found (see subsection 2.2.2). HAXPES is used as a powerful surface- and interface-sensitive tool to systematically study the impact of the environment on the perovskite absorber in high vacuum in the dark and under UV radiation (by using a solar simulator). The impact of water in the dark and under illumination on the perovskite absorber is studied in-situ by using AP-HAXPES to gain direct insight into the degradation process.

For AP-HAXPES the analysis chamber is filled with water vapor background present by evacuating the chamber, which contains a beaker with water, until equilibrium vapor pressure of water is reached. A small entrance aperture and differential pumping of the electron analyzer lens system keeps the analyzer in UHV. Moreover for AP-HAXPES measurements the attenuation of the intensity is enhanced in water vapor compared to UHV, since the electrons can scatter in water on the way to the analyzer.

First, ambient experiments were done on 60 nm perovskite samples by simply exposing the absorber to water vapor and performing (AP-)HAXPES measurements of the sample in UHV ($p \sim 9 \times 10^{-7}$ Torr) and water vapor ($p \sim 19.7 - 16.4$ Torr) with indirect ambient light illumination conditions (the view ports of the chamber were not covered).

For a more defined experiment and for simulating the "natural" conditions, in a second run samples with 300 nm thick perovskites were exposed in a UHV chamber to different environments. In the beginning, the viewports of the chamber were covered to keep the sample in the dark and

In-situ Study and Characterization of Environmental Impact on Mixed Halide Perovskite Absorbers

(AP-)HAXPES measurements were performed in high vacuum ($p \sim 1 \times 10^{-5}$ Torr) and water vapor ($p \sim 14.6 - 15.4$ Torr). Note that for e.g., the water experiment in the dark, the pressure in the chamber was 15.3 Torr at the beginning of the sequence measurements and slowly decreased to 14.7 Torr, likely due to a change in temperature which will lead to a small change in the equilibrium vapor pressure of water. At 17°C the equilibrium vapor pressure of water is about 14.5 Torr and at 18°C it is 15.5 Torr [98]. Therefore an averaged pressure of 15 Torr can be assumed for the 300 nm sample measurements in water vapor. "Illumination" measurements were performed in water vapor, with UV light illuminating the sample through a view port with a HAL-320 solar simulator from "Asahi Spectra" offering a solar spectrum with AM1.5G. The illumination experiment was performed in two stages: low water pressure conditions in high vacuum ($p \sim 1.8 \times 10^{-4} - 2.6 \times 10^{-5}$ Torr), where the chamber was wet but no beaker with water is included, and high water pressure conditions ($p \sim 14.6 - 15.2$ Torr) including a beaker with water in the chamber. For the first case, a film of water formed during pumping of the chamber. For the in-situ measurements of the 60 and 300 nm sample, sequences were started to track the changes of the core level spectra characteristics of the mixed-halide perovskites as a function of time under the respective conditions. During one sequence O 1s, I 3d, C 1s and Pb 4f spectra, presented in the following, were measured with an excitation energy of $h\nu = 4$ keV.

5.1. 60 nm Perovskites in UHV and Water Vapor

The impact of exposure of perovskites to water vapor was first studied on perovskite absorbers of 60 nm thickness, i.e. the perovskite was thinner than the standard thickness of 300 nm which leads to optimum device performance in solar cells [99]. The precursor solution was prepared as described in 2.2.4 for a thickness of 300 nm and then diluted with DMF to get a nominal thickness of 60 nm.

HAXPES measurements were performed in UHV and at a pressure equivalent to the vapor pressure of water to study/track changes in the core level spectra representing the perovskite under ambient conditions. Note that for UHV measurements single scans were taken and the spectra, including fit analysis, can be found in Appendix B.1 (see Figure B.1(a) to B.1(d)).

For the measurements in water vapor, sequences of the core levels were recorded and in the following Figures 5.1 to 5.4 the representative core levels O 1s, Pb 4f, I 3d and C 1s spectra of the perovskite are shown as a 2D plot in the left panel as well as some representative selected spectra in 1D, converted from the 2D plot, in the top (left) panel.

In the O 1s spectra in Figure 5.1 the presence of water can be seen as two additional peaks,

5.1 60 nm Perovskites in UHV and Water Vapor

denoted C and D, in addition to the two species A and B (identified through fitting) which were already present in UHV. Note that the zero of the time axis is set to the time of the first gold reference measurement in UHV.

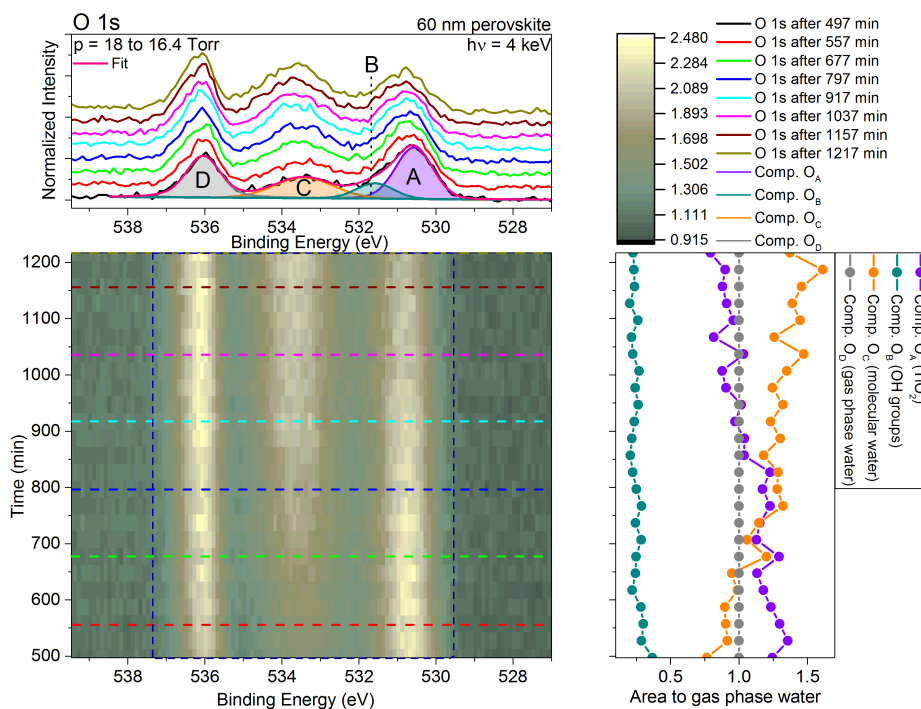


Figure 5.1.: O 1s spectra and fit results of the 60 nm sample over time in water vapor. Left bottom panel shows the measured O 1s as a 2D plot and representative selected spectra are shown in the left top panel as a 1D plot including the species from the fits labeled as A,B,C and D. The right panel shows the area of each of the four species determined from the fits divided by the area of the gas phase water contribution. The dark blue dashed line in the 2D plots indicates the fit range of the species displayed on the right.

Through fitting, the species labeled as A,B,C and D can be attributed to O_A with an average E_B of (530.7 ± 0.1) eV ascribed to O in TiO_2 , O_B with (531.7 ± 0.1) eV to OH groups, O_C with (533.6 ± 0.1) eV to adsorbed molecular water and O_D with (536.1 ± 0.1) eV to gas phase water [84, 100]. The spectra were fitted by coupling the shape and width as well as the chemical shift of the OH peak to the TiO_2 peak and setting it fixed after first iterations for batch processing. A Shirley background was used, and the gas phase and molecular water peak were freely fitted.

In general, O 1s spectra show a complex peak structure indicating different chemical species of O which can be quite complex in presence of water [101]. Changes in the shape, especially

In-situ Study and Characterization of Environmental Impact on Mixed Halide Perovskite Absorbers

for in-situ measurements, indicate changes in the distribution of species, but can as well be attributed to formation of new species. For the fitting procedure of O 1s the number of species were kept to a reasonable minimum expected for water adsorption on TiO₂ according to [100].

After the sample has been in water vapor for some time the molecular water component starts to grow, which indicates adsorption of water on the sample surface. Simultaneously the contribution of TiO₂ is decreasing, as expected for deposition of water from water vapor due to attenuation of the signal by the water film.

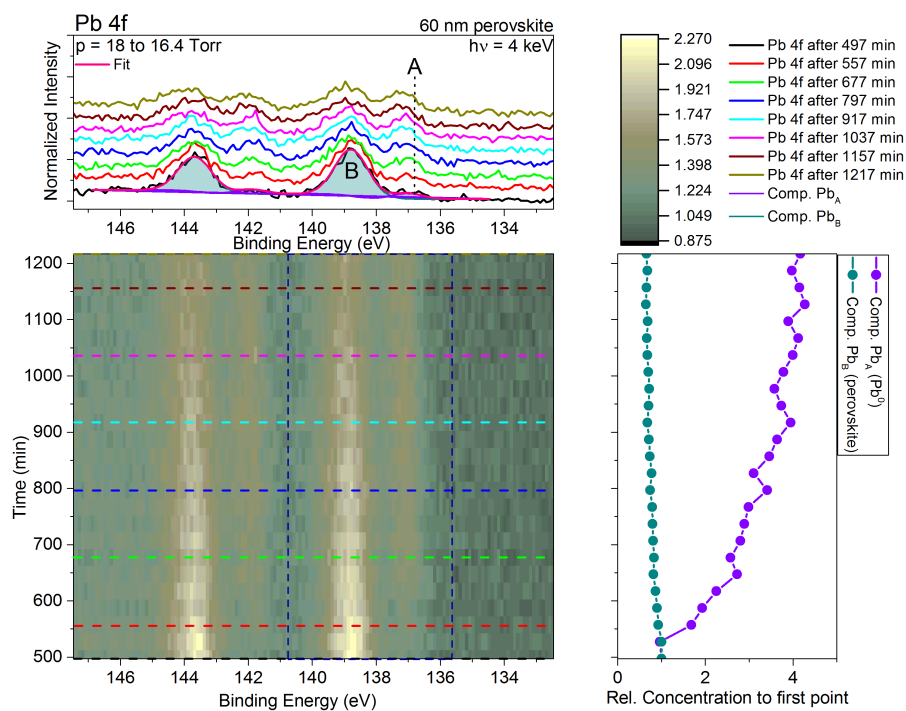


Figure 5.2.: Pb 4f spectra and fit results of the 60 nm sample over time in water vapor. Left bottom panel shows the measured Pb 4f as a 2D plot and representative selected spectra are shown in the left top panel as a 1D plot including the species from the fits labeled as A and B. The right panel shows the relative concentration of the two species determined from the fits divided by the relative concentration of the first spectrum of this sequence. The dark blue dashed line in the 2D plots indicates the fit range of the species displayed on the right.

The spectra in Figure 5.2 shows the Pb 4f measured along with the O 1s. The main peak labeled B, with an averaged E_B of (138.9 ± 0.1) eV obtained from the fits, can be attributed to Pb in perovskite. However, the published values for the chemical shift between Pb in PbI₂ and Pb in perovskite environment can be around 0.3 eV [79] for pure materials, nevertheless can

5.1 60 nm Perovskites in UHV and Water Vapor

both species coexist in the absorber resulting in a lower chemical shift and therefore can not be resolved in the experiment. Thus whenever the Pb species is ascribed to perovskite also PbI_2 might be possible and additionally present. Pb_A with an averaged E_B of (137.1 ± 0.1) eV can be attributed to metallic lead (Pb^0) [79, 84, 102].

For the fits of the 60 nm perovskite Pb 4f spectra in water vapor, the Pb 4f peaks were fitted with Voigt functions and a Shirley background and two species were assumed using Unifit [62]. The spin-orbit splitting was fixed to 4.86 eV [88] and the area ratio of the spin-orbit doublets was fixed to 3:4. The width and shape of the Pb 4f peak for perovskite and for Pb metal, as well as the chemical shift (~ 1.8 eV) between them, was fixed to averaged values obtained after some iterations of batch processing.

Figure 5.2 shows, on the right side, the relative concentrations of the two components relative to the first data point over time, and a clear increase of the metallic component Pb^0 (Pb_A) and decrease of the perovskite component can be seen. The mechanism for Pb^0 formation seems to be mostly x-ray beam driven, as can be seen especially after the sequence when a new spot is chosen and the beam is for some time on the new spot, causing an increase in the metallic component again (see appendix Figure B.2).

To determine reproducibility of the experiment, the sample was cut in half in the beginning and the second half was used as a fresh sample to repeat the measurements, including repeated exposure to water vapor. A similar trend to the first experimental run can be seen (see Figure B.3). Although for the second run the sample had a shorter exposure time to x-rays in vacuum, the increase of Pb^0 in water vapor clearly indicates an interplay between water and x-rays with the sample surface (radiolysis effect) [103].

An increase of metallic Pb would imply a decrease of I, assuming that PbI_2 is present and degrades into Pb^0 and I_2 [48], where the latter as a gas would be pumped away. Figure 5.3 shows I 3d spectra including the fit analysis. For the fit only the I $3d_{5/2}$ peak was fitted with a Shirley background and Voigt function using the batch processing function in Unifit 2016. The averaged E_B of the I $3d_{5/2}$ peak was determined to be (619.7 ± 0.1) eV and can be attributed to I in a perovskite environment [79, 84, 102].

In the I 3d spectra a clear decrease in the intensity can be seen (see Figure 5.3), indicating either the loss of I or the adsorption of water on the perovskite. The loss of I would be, under consideration of the increase in Pb^0 , an indication for radiolysis and is here likely the case. Since adsorption of water on the perovskite would also lead to an decrease of the Pb^0 signal, which is not the case. After the sequence in water vapor I 3d spectra were not measured for the new spot, but the shallow core levels give a clear indication that the growth of metallic Pb component and the decrease of I are linked (see Figure B.4), leading to a degradation of the perovskite or mainly

In-situ Study and Characterization of Environmental Impact on Mixed Halide Perovskite Absorbers

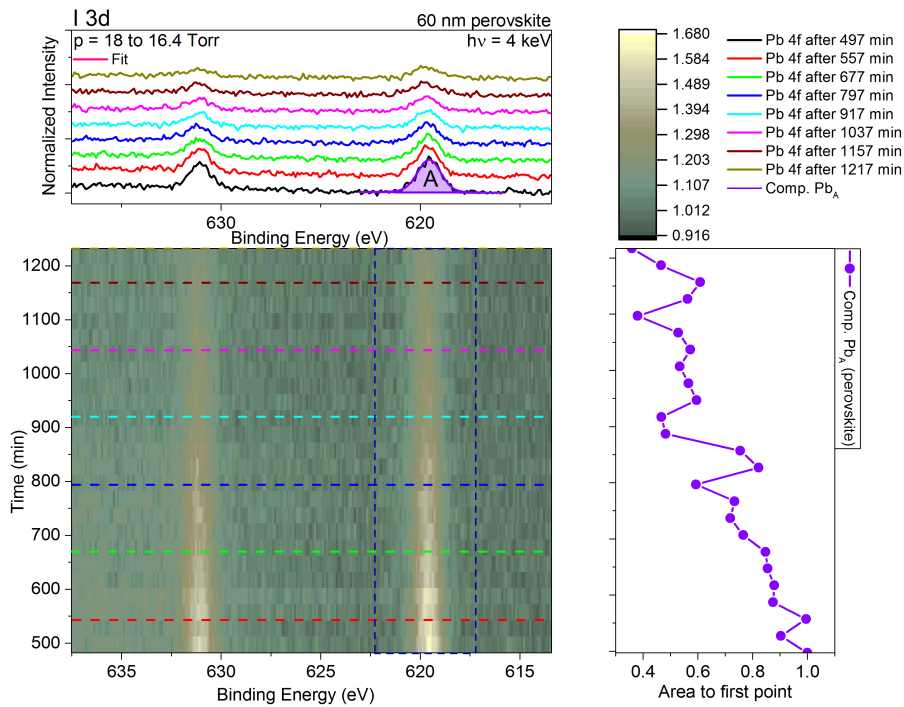


Figure 5.3.: I 3d spectra and fit results of 60 nm sample over time in water vapor. Left bottom panel shows the measured I 3d as a 2D plot and representative selected spectra are shown in the left top panel as a 1D plot including the species from the fits labeled as A. The right panel shows the area ratio of the species determined from the fits divided by the area of the first spectrum of this sequence. The dark blue dashed line in the 2D plots indicates the fit range of the species displayed on the right.

PbI₂ through radiolysis [103] as the underlying degradation mechanism. The C 1s spectra were also measured and are shown in Figure 5.4. The low appearing Methylammonium iodide (MAI, CH₃NH₃I) content (second peak) in the C 1s spectrum for UHV and similarly in water vapor (see Figure B.1(a) and 5.4) can indicate two things. Either the adventitious carbon component is relatively large to the MAI component, which might be due to contamination from air when the sample was mounted. Or the other possible explanation would be that part of the absorber was already converted into PbI₂ at the start of the measurements and/or the conversion of the precursor solution into perovskite was incomplete. Additionally is also a combination of both cases possible.

In water vapor C 1s (see Figure 5.4) seems to overall increase with time. A closer look at the relative concentration, normalized to the first data point of the sequence, indicates an increase for component C_A (adventitious carbon) with an average E_B of (285.9 ± 0.1) eV and a small increase of C_B = (287.1 ± 0.1) eV (averaged) attributed to MAI [88, 102]. However, consid-

5.1 60 nm Perovskites in UHV and Water Vapor

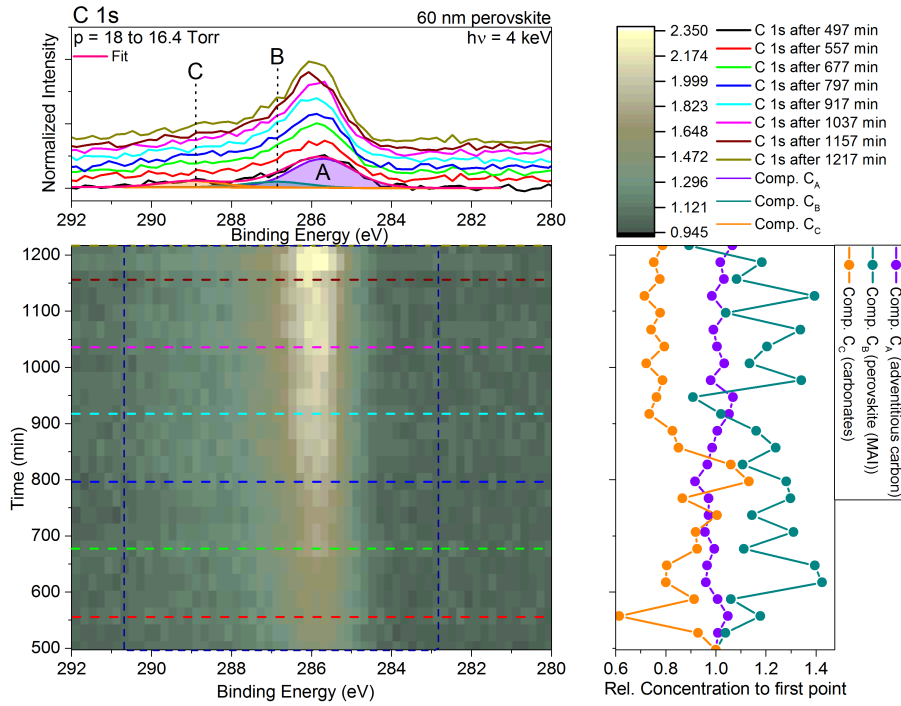


Figure 5.4.: C 1s spectra and fit results of 60 nm sample over time in water vapor. Left bottom panel shows the measured C 1s as a 2D plot and representative selected spectra are shown in the left top panel as a 1D plot including the species from the fits labeled as A, B and C. The right panel shows the relative concentration of the three species determined from the fits divided by the relative concentration of the first spectrum of this sequence. The dark blue dashed line in the 2D plots indicates the fit range of the species displayed on the right.

ering the low signal-to-noise ratio of the spectra and that the relative concentration of C_B was normalized to the first point, which might have been very low. It can be assumed that the relative concentration of the MAI stays constant within the scatter of the data. The huge fluctuation of the MAI component can be explained by the larger fitting uncertainty of the small peak through the low signal-to-noise ratio compared to component C_A . Component $C_C = (289.2 \pm 0.1)$ eV (averaged) can be ascribed to carbonates [88, 102] and seems to decrease over time, but similar to the MAI (C_B) special care has to be taken due to the low signal-to-noise ratio. It can be either assumed that carbonates (C_C) are constant over time or they are reduced by water adsorption, which is unlikely since the Pb^0 signal is not decreasing (no water adsorption on the perovskite). Note that in water vapor the measured E_B for C 1s are slightly higher compared to UHV (see appendix B.1), whereas the other core levels show similar E_B within the error margin.

The C 1s spectra of the sample in water vapor was fitted similar to Pb 4f spectra with a fixed

In-situ Study and Characterization of Environmental Impact on Mixed Halide Perovskite Absorbers

chemical shift of ~ 1.2 eV for MAI and ~ 3.3 eV for carbonates relative to adventitious carbon.

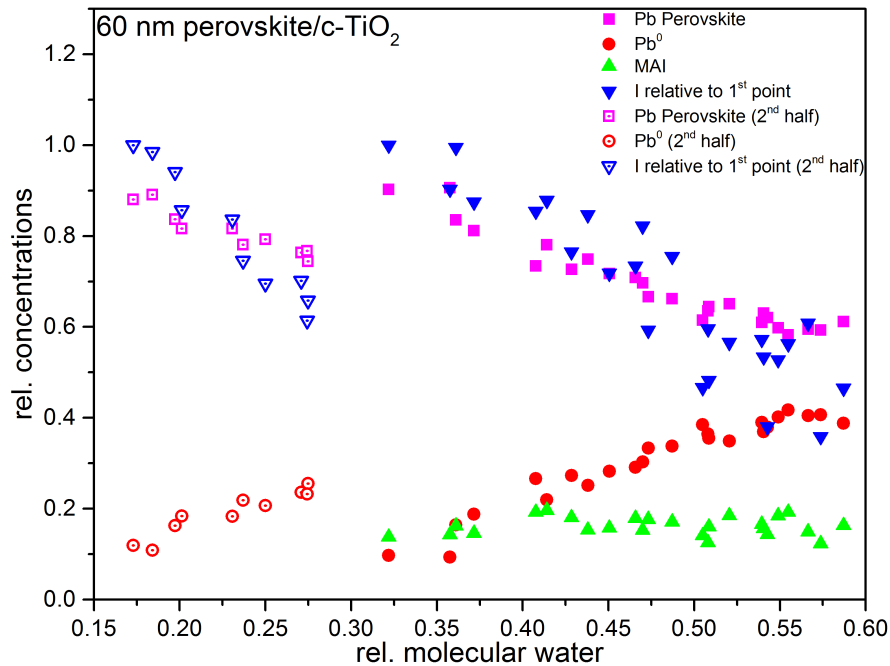


Figure 5.5.: Shows relative concentrations of Pb perovskite (PbI_2), Pb^0 , MAI and I over relative concentration of molecular water for 60 nm perovskite. Note that I is not given as relative concentration but relative to first data point (area). Open symbols with dot give the results of the second sample, which is the second half of the perovskite sample.

The results obtained from the fits so far lead to the conclusion, that radiolysis of the perovskite for the 60 nm sample seems to be enhanced by the water presence. The electrons produced in water by x-rays can reduce Pb^{2+} from PbI_2 to Pb^+ , which further disproportionate into Pb^0 [103]. This mechanism does not seem to depend on the initial amount of molecular water absorbed on the surface as it will be reasoned in the following. Figure 5.5 shows the relative concentration of the different perovskite elements (for both 60 nm samples) plotted over the relative concentration of molecular water. It can be clearly seen that in both cases I and Pb correlated to perovskite decreases and Pb^0 increases with water. The only difference is, that for the second half of the sample the same trend can already be seen for smaller amounts of molecular water and shorter x-ray exposure, which means that x-rays together with water are the driving force behind that degradation. This is further supported by Pb 4f spectra shown in Figure B.2, as already discussed above. Note that for both measurements (sample halves) zero in the time axis is set to the first gold reference measurements in UHV.

5.2. Environmental Effects on 300 nm Perovskites

In the following subsections, the results of the study of 300 nm perovskite samples under ambient conditions are presented. Compared to the 60 nm sample set, sequence measurements were also performed in high vacuum and better defined conditions w.r.t. illumination for the sample during measurements were assured. Note that for the 300 nm sample it is very likely that the TiO_2 is still not completely covered by the perovskite (see chapter 4) and therefore UV light and x-rays can reach the substrate. TiO_2 is a known photocatalyst, thus interactions of the substrate with UV light (and x-rays) need to be considered in addition to changes in the perovskite and the possible influence on them.

In Table 5.1 the possible degradation mechanism are listed, as mentioned in subsection 2.2.2 from Ref. [16, 19, 47, 48], that are expected to occur for the perovskite in high vacuum in the dark, in water in the dark, and in water under illumination, together with the expected species that could be detected with HAXPES. Note that Pb 4f of PbI_2 and perovskite has very similar E_B and can not be distinguished, hence the Pb species labeled in the following as perovskite can also be PbI_2 .

Table 5.1.: Table shows possible degradation mechanisms according to Ref. [16, 19, 47, 48] (see subsection 2.2.2) and the possible species/core levels that could be measured. The equations are labeled by letters in brackets for reference.

Environment	Possible degradation mechanism	Expected species which could be detected
Vacuum in the dark [19]	$\text{CH}_3\text{NH}_3\text{PbI}_3 \rightarrow \text{CH}_3\text{NH}_2(g) + \text{HI}(g) + \text{PbI}_2(s) + \text{V}_I^-$ (A)	MA [C] HI [I] PbI_2 /perovskite
Water vapor in the dark [16,47]	$\text{CH}_3\text{NH}_3\text{PbI}_3(s) \rightarrow \text{CH}_3\text{NH}_3\text{I}(aq) + \text{PbI}_2(s)$ (B1) $\text{CH}_3\text{NH}_3\text{I}(aq) \rightarrow \text{CH}_3\text{NH}_2(aq) + \text{HI}(aq)$ (B2)	MA [C] HI [I] PbI_2 /perovskite
Water vapor under illumination [16,19,47,48]	$\text{CH}_3\text{NH}_3\text{PbI}_3(s) \rightarrow \text{CH}_3\text{NH}_3\text{I}(aq) + \text{PbI}_2(s)$ (C1) $\text{CH}_3\text{NH}_3\text{I}(aq) \rightarrow \text{CH}_3\text{NH}_2(aq) + \text{HI}(aq)$ (C2) $\text{HI}(aq) \rightarrow \text{H}_2(g) + \text{I}_2(s)$ (C3) $\text{PbI}_2(s) \rightarrow \text{Pb}^0(s) + \text{I}_2(g)$ (C4)	MA [C] HI [I] Pb^0 PbI_2 /perovskite

In-situ Study and Characterization of Environmental Impact on Mixed Halide Perovskite Absorbers

5.2.1. Perovskite in the Dark and in High Vacuum

The first measurements on 300 nm perovskite were performed in high vacuum in the dark at a pressure of $p \sim 1.1 \times 10^{-5}$ Torr. The following Figures 5.6 to 5.9 show the representative core levels O 1s, I 3d, C 1s and Pb 4f spectra of the perovskite as a 2D plot in the left panel as well as some representative selected spectra in 1D, converted from the 2D plot, in the top (left) panel. The zero point of the timescale is the start of the first scan of the sequence of the respective core level, although the beam has been on the same spot already for 2h and 22 min to measure a survey and some core levels prior to the sequence.

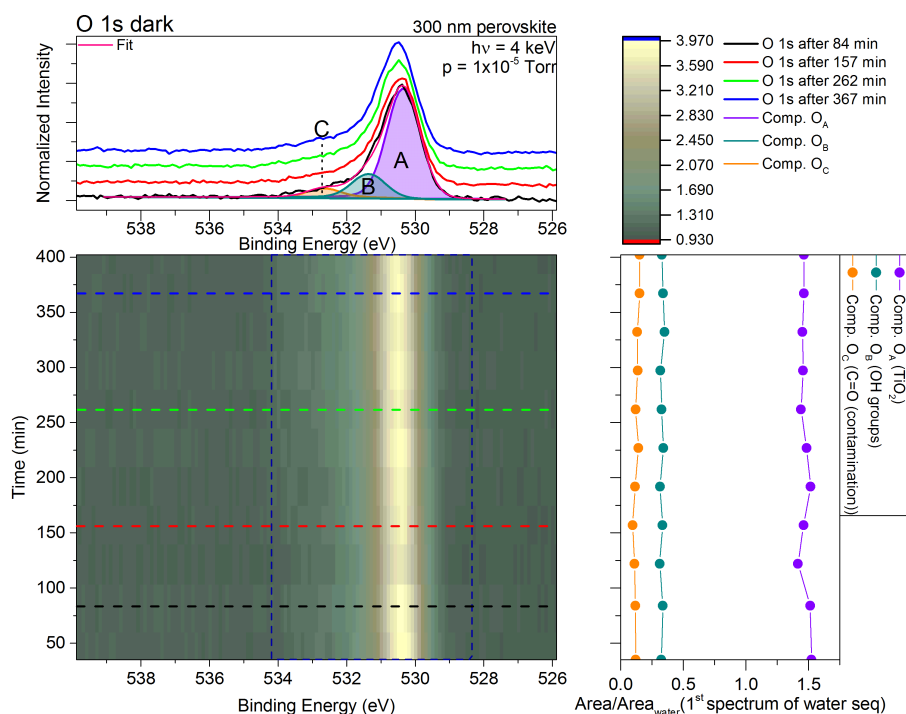


Figure 5.6.: O 1s spectra and fit results of 300 nm sample over time in the dark and in high vacuum. Left bottom panel shows the measured O 1s as a 2D plot and representative selected spectra are shown in the left top panel as a 1D plot including the species from the fits labeled as A,B and C. The right panel shows the area of each of the three species determined from the fits divided by the area of the gas phase water contribution from the first spectrum of the water sequence. The dark blue dashed line in the 2D plots indicates the fit range of the species displayed on the right.

In Figure 5.6 the O 1s 2D and 1D plot indicates that no changes occur during the measurement time window, which is confirmed by the fit results. The area of all three components O_{A,B,C} is constant over time (see right panel in Figure 5.6). From the fits the following averaged

5.2 Environmental Effects on 300 nm Perovskites

E_B for the components are obtained; $O_A = (530.4 \pm 0.1)$ eV, $O_B = (531.4 \pm 0.1)$ eV and $O_C = (532.75 \pm 0.10)$ eV which are lower in E_B than those obtained for the 60 nm sample in UHV and in water vapor (see appendix B.1 and 5.1), but still can be attributed to O in TiO_2 (A), OH groups (B) and to C=O (C) bonds in the organic component of the perovskite [84, 100]. The oxidation of the organic component can be due to different reasons; one reason could be that the sample was mounted in air, another possibility is the oxidation of the organic component at the perovskite/ TiO_2 interface. Next I 3d will be discussed, which was measured along with O 1s

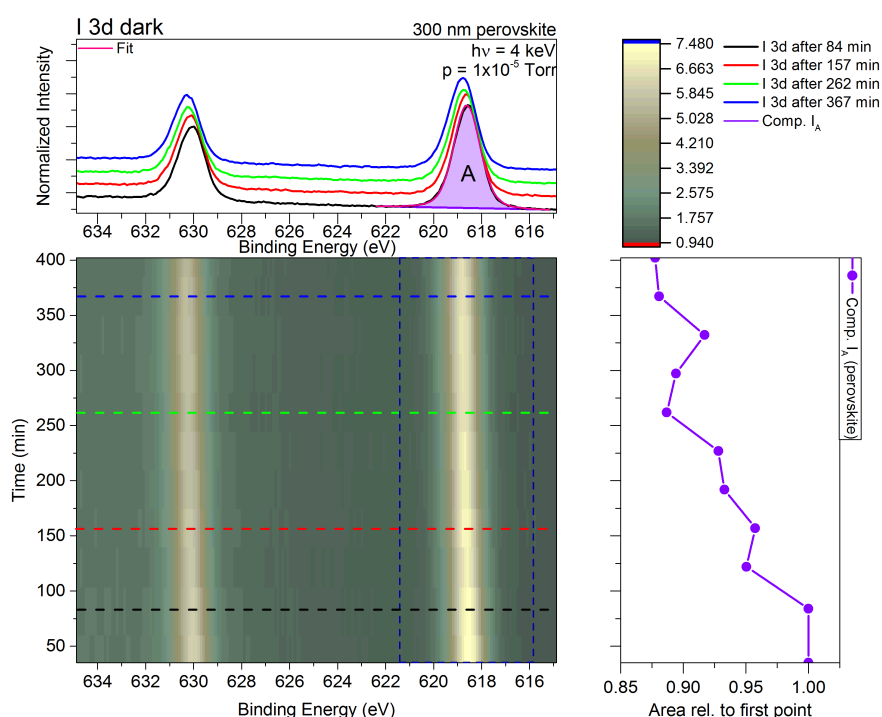


Figure 5.7.: I 3d spectra and fit results of 300 nm sample over time in the dark and in high vacuum. Left bottom panel shows the measured I 3d as a 2D plot and representative selected spectra are shown in the left top panel as a 1D plot including the species from the fits labeled as A. The right panel shows the area ratio of the species determined from the fits divided by the area of the first spectrum of this sequence. The dark blue dashed line in the 2D plots indicates the fit range of the species displayed on the right.

and is shown in Figure 5.7. The I 3d 2D and 1D spectra measured in high vacuum in the dark, (see Figure 5.7) shows only one component, as revealed by the fit of the I $3d_{5/2}$ peak. Note that for the 300 nm sample a linear background was used for fitting of the I $3d_{5/2}$ peak. Component I_A decreases by approximately 12 % over time, as can be seen in the right panel of Figure 5.7, which could be due to I loss in high vacuum. Iodine, in form of HI (g) according to equation

In-situ Study and Characterization of Environmental Impact on Mixed Halide Perovskite Absorbers

(A) in Table 5.1, may be pumped away in the system, which would be according to Tang et al. [19] the first sign of degradation, or it might come from excess iodine linked to the MAI in gas form after the perovskite absorber production. The latter is likely since for the preparation of the perovskite a molar ratio of 3:1 for MAI and PbCl_2 is used (see subsection 2.2.4) leading to possible excess of I (and Pb^{+2} vacancies [104]). However, HI does not appear in the I 3d spectrum as an additional species; the shape of the I 3d peaks clearly stays the same. The averaged E_B of the I $3d_{5/2}$ peak was determined to be (618.7 ± 0.1) eV and can be attributed to I in a perovskite environment, although the E_B for I of the 60 nm sample in UHV and water vapor is higher (see appendix B.1 and 5.1) and might be partly explained by the difference in chemical bonding of the perovskite to the substrate for thinner films [102].

Evaporation of excess I linked to MAI would also be visible in the C 1s spectra as a decrease

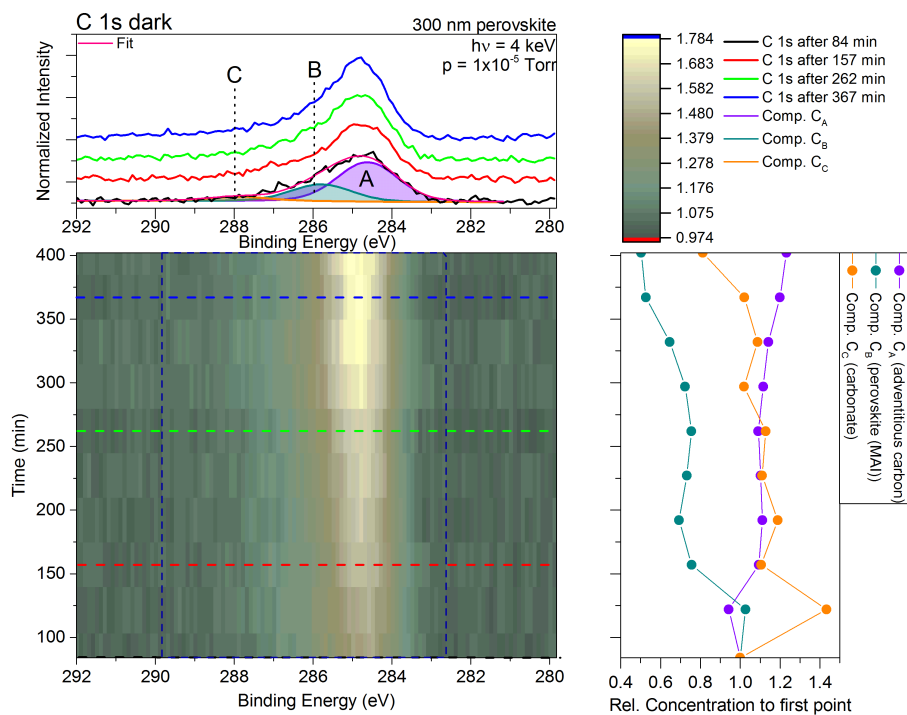


Figure 5.8.: C 1s spectra and fit results of 300 nm sample over time in the dark and in high vacuum. Left bottom panel shows the measured C 1s as a 2D plot and representative selected spectra are shown in the left top panel as a 1D plot including the species from the fits labeled as A,B and C. The right panel shows the relative concentration of the three species determined from the fits divided by the relative concentration of the first spectrum of this sequence. The dark blue dashed line in the 2D plots indicates the fit range of the species displayed on the right.

5.2 Environmental Effects on 300 nm Perovskites

of the MAI component. Figure 5.8 shows the C 1s spectra in the dark, and three species can be identified through fitting, which can be attributed to C_A (adventitious carbon) with an average E_B of (284.7 ± 0.1) eV, to $C_B = (285.9 \pm 0.1)$ eV (averaged) attributed to MAI and to $C_C = (288.0 \pm 0.1)$ eV (averaged) ascribed most likely to carbonates [88, 102]. Similar to the other core levels, the E_B for the carbon species of the 300 nm sample in high vacuum in the dark is at a lower E_B compared to the 60 nm sample.

In high vacuum, the component for adventitious carbon (C_A) increases over time compared to the first data point (see right panel in Figure 5.8), whereas the components for carbonates and MAI decrease. The decrease of C_B indicates a loss of MAI over time, e.g., being pumped away in vacuum.

The last core level presented here for the sequence measured of a perovskite in high vacuum

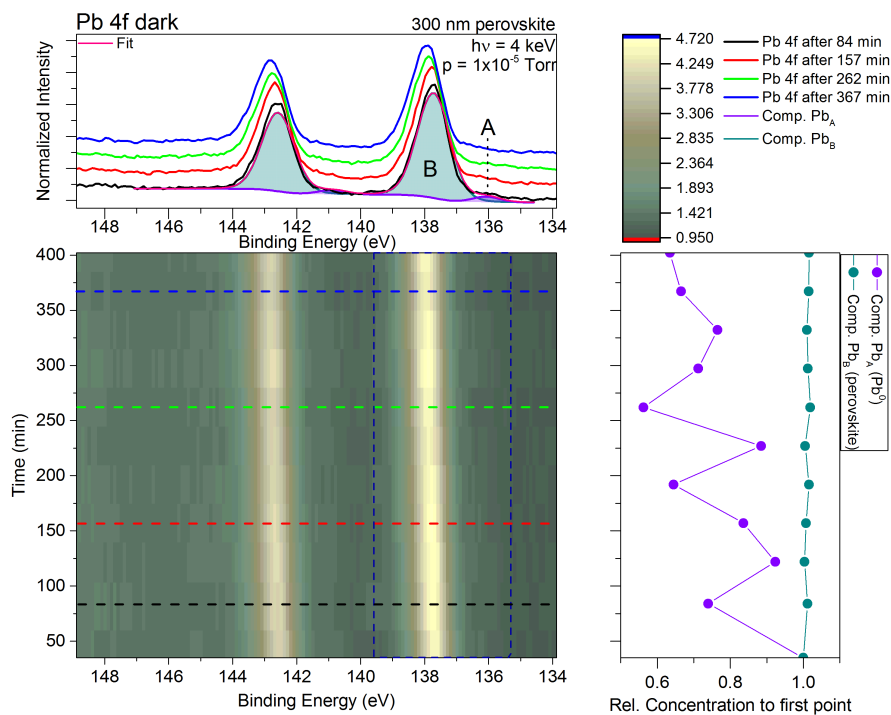


Figure 5.9.: Pb 4f spectra and fit results of 300 nm sample over time in the dark and in high vacuum. Left bottom panel shows the measured Pb 4f as a 2D plot and representative selected spectra are shown in the left top panel as a 1D plot including the species from the fits labeled as A and B. The right panel shows the relative concentration of the two species determined from the fits divided by the relative concentration of the first spectrum of this sequence. The dark blue dashed line in the 2D plots indicates the fit range of the species displayed on the right.

In-situ Study and Characterization of Environmental Impact on Mixed Halide Perovskite Absorbers

in the dark is Pb 4f. Figure 5.9 shows the Pb 4f spectra on the left side (top is 1D presentation, bottom 2D presentation) measured in high vacuum. The species determined from the fits (chemical shift fixed to 1.7 eV) are labeled as A and B in the left top panel. An averaged Pb 4f_{7/2} E_B of (136.2 ± 0.1) eV for Pb_A and of (137.9 ± 0.1) eV for Pb_B can be determined, which can be attributed to metallic lead (Pb⁰) and Pb in a perovskite environment (or PbI₂), respectively [79, 84, 102]. Similar to the other core levels, the E_B for the sample in high vacuum in the dark is lower compared to the E_B of Pb in the 60 nm samples. Although Pb_B is here and in the following subsections denoted as Pb in perovskite, the presence of PbI₂ in the absorber can not be excluded, since the chemical shift between Pb in PbI₂ and Pb in perovskite environment is usually smaller than 0.3 eV [79] given for pure materials in literature and therefore both species can coexist in the absorber but can not be resolved separately. The possible presence of PbI₂ in the absorber can be explained by precursor solution remainders due to incomplete conversion into the perovskite or as a product of degradation.

The right panel in Figure 5.9 shows the relative concentration of the two species over time and indicates a constant behavior for component Pb_B, whereas Pb metal decreases, demonstrating no degradation of the sample (in high vacuum in the dark), which also suggests that the decrease in I area (see Figure 5.7) might come from evaporation of excess MAI.

For the fit of Pb 4f spectra, part of the extensive plasmonic loss structure extending over 20 eV at higher E_B needs to be considered, since the structure partly overlaps with the main Pb 4f peaks affecting the obtained areas from the fit [76]. Moreover, for the sequence measurement, the complete plasmonic loss structure was cut to a E_B of ~ 149 eV and therefore only relative changes of the areas of the Pb 4f spectra can be given, due to unequal plasmonic contributions to Pb_A and Pb_B. Hence the significant decrease of the metallic component might partly come from a higher fitting uncertainty for the small peak compared to the perovskite peak, due to the fixed chemical shift between the two Pb species and the adjusting of the Shirley background for the fit due to the missing plasmonic contribution.

Further, Figure 5.9 shows a shift in the 2D plot to higher E_B over time, which could be interpreted as a conversion of perovskite into PbI₂. Since PbI₂ would be in the Pb spectra located at the higher E_B side of the perovskite. But a closer look at the other core level spectra (O 1s, C 1s and I 3d) of this subsection shows a similar shift for all in the order of 0.2 eV to higher E_B indicating, in this case a shift in excitation energy of the x-ray beam as underlying reason is more likely. Note that a shift in photon energy leads to equal shifts for all core-levels, which is here the case.

5.2.2. Perovskite in the Dark and Water Vapor

After the measurements in high vacuum and in the dark were complete, water vapor was introduced and a fresh spot was chosen on the sample for the next sequence measurements to avoid changes in the spectra due to possibility of a prior beam damaged sample surface. The timescale continues from the high vacuum measurements, including the break between the measurements for introducing the beaker with water into the chamber.

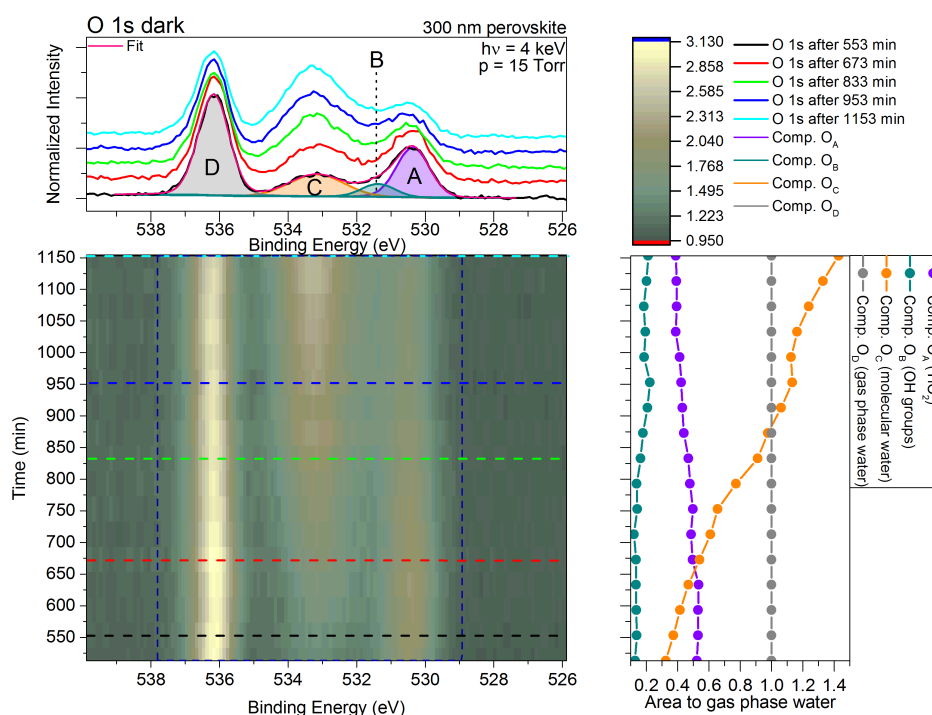


Figure 5.10.: O 1s spectra and fit results of 300 nm sample over time in the dark at 15 Torr. Left bottom panel shows the measured O 1s as a 2D plot and representative selected spectra are shown in the left top panel as a 1D plot including the species from the fits labeled as A,B,C and D. The right panel shows the area of each of the four species determined from the fits divided by the area of the gas phase water contribution. The dark blue dashed line in the 2D plots indicates the fit range of the species displayed on the right.

In the following the core levels measured in the sequence will be discussed in the same order as it was done for 5.2.1, starting with the O 1s spectra in Figure 5.10. The presence of water vapor in the chamber can be related to peak C and D in the O 1s spectra (see Figure 5.10). Through fitting, in total four species can be identified, labeled again as A,B,C and D, similar to the ones in 5.1. The main Peak O_A with a E_B of (530.4 ± 0.1) eV can be attributed to O in TiO_2 , O_B

In-situ Study and Characterization of Environmental Impact on Mixed Halide Perovskite Absorbers

with (531.4 ± 0.1) eV to OH groups, O_C with (533.2 ± 0.1) eV to molecular water and O_D with (536.2 ± 0.1) eV to gas phase water [84, 100]. The determined E_B are lower than the one obtained for the 60 nm sample (see section 5.1 and B.1), except for the gas phase water, being similar in both cases. Compared to the sample in high vacuum (see subsection 5.2.1) the E_B are similar.

From the 2D plot and right panel in Figure 5.10 a clear decrease in intensity can be seen for the TiO_2 component (O_A), whereas molecular water (O_C) increases and gas phase water (O_D) is constant (chosen by normalization), indicating an increased adsorption of molecular water. The small increase of component O_B (OH groups) indicates that the water molecules not only adsorb on the surface but also partly dissociate. The presence of OH groups at the perovskite/water interface agrees with Weinhardt et al. [105], they reported that there is always an OH component in x-rays of liquid water due to proton dynamics.

With equation 3.3 the thickness of the layer of water growing on TiO_2 can be estimated, where I_0 is the averaged area of TiO_2 in high vacuum and $I(d)$ the area of TiO_2 in water vapor. For the last spectrum in water vapor a film thickness of 8.4 nm is determined. However the intensity decreases in water vapor, and therefore I_0 , used from high vacuum, is overestimated and it can be only stated that during the measurements in water vapor the film thickness increases by 3 nm. A thin layer of water adsorbed on the surface from vapor is very likely through the constant resupply of water vapor from the beaker, filled with water and the temperature decrease in the chamber by $< 1^\circ C$ corresponding to a decrease of 0.6 Torr in 10 h. Note that the actual thickness of the water film can be higher, if the water starts to adsorb on the perovskite surface (see morphology in chapter 4) and adsorbs later on the *exposed* TiO_2 , leading to a slower intensity decrease in equation 3.3 and therefore underestimation of the water film thickness. Also according to Ketteler et al. [100] nucleation sites first need to be formed on TiO_2 before water adsorbs on the surface, indicated by the presence of OH groups acting as such.

Figure 5.11 shows the I 3d spectra and the fit results, which indicate a clear decrease of I 3d intensity as well as a shift in E_B , first to lower E_B and then back to higher E_B . This "curve" behavior can not be clearly seen in O 1s in Figure 5.10 because the broadness of the peaks and the decrease/increase of the TiO_2 /molecular water peak makes it difficult, but the determined E_B from the fits show a small shift of max. 0.1 eV to lower E_B which is still within the error margin.

The averaged E_B for I_A is (619.3 ± 0.1) eV, which is still consistent with I in a perovskite environment. But shifted to higher E_B by 0.6 eV compared to the E_B of I_A in high vacuum, (see subsection 5.2.1) and is still lower than the E_B of I_A in the 60 nm sample (see section 5.1

5.2 Environmental Effects on 300 nm Perovskites

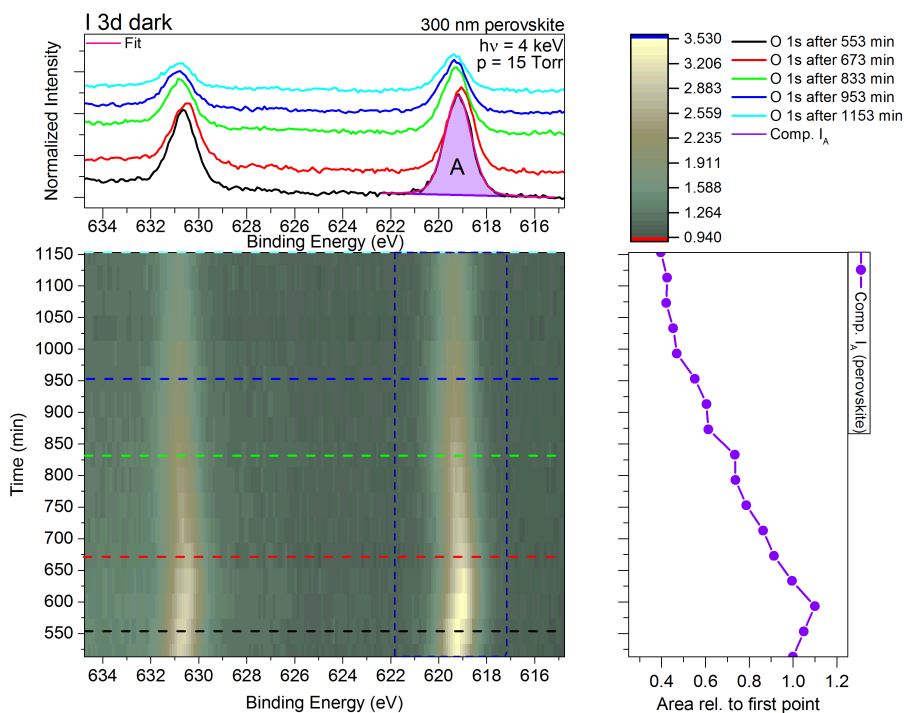


Figure 5.11.: I 3d spectra and fit results of 300 nm sample over time in the dark at 15 Torr. Left bottom panel shows the measured I 3d as a 2D plot and representative selected spectra are shown in the left top panel as a 1D plot including the species from the fits labeled as A. The right panel shows the area of the species determined from the fits divided by the area of the first spectrum of this sequence. The dark blue dashed line in the 2D plots indicates the fit range of the species displayed on the right.

and B.1). The E_B shift in water vapor compared to the sample in high vacuum might be due to the water adsorbing on the surface. This would also partly explain the accelerated decrease of I intensity due to attenuation of electrons (energy loss) in the additional water film according to equation 3.3. In high vacuum the I $3d_{5/2}$ signal decreases by a factor 3.1×10^{-3} per min whereas in water vapor it decreases by a factor of 4.3×10^{-3} per min indicating an additional mechanism to water growth, which might be also partly due to iodine loss from launching of the degradation process. According to equation (B2) in Table 5.1 an additional species (HI) should be detected; the absence of the corresponding signal might be due to the dilution of HI in water below the detection limit (which would be higher than in conventional XPS due to the low signal-to-noise ratio).

Similar to the discussion of the E_B shift over time for the high vacuum measurements (see subsection 5.2.1), the E_B shift of I with time might be explained by a change in energy of the

In-situ Study and Characterization of Environmental Impact on Mixed Halide Perovskite Absorbers

x-ray beam; since all core levels for the 300 nm sample in water vapor in the dark exhibit this shift first to lower E_B and then to higher E_B . But O 1s show a small shift of max 0.1 eV which is in the error margin, whereas the perovskite related core levels shows a shift of max 0.2 eV to lower E_B . This small difference in shifts excludes therefore the instability of the x-ray beam energy as the cause. Which means in this case two other possibilities exists to explain the shift in E_B : one would be the chemical shift by adsorption of water on the surface, usually leading to shift to higher E_B . Another possible explanation for that shift would be the formation of a dipole or Helmholtz layer in the presence of water at the perovskite surface.

If it is assumed that the perovskite sample is (becomes) n-doped after preparation, because it has an I deficiency (I^- vacancies) due to I loss [104,106], then ions can be present at the surface. They might also be partly created by decomposition of the perovskite in contact with water [21] or move to the surface by ion migration [107]. Additionally water begins to adsorb on the surface by first dissociating water molecules, forming OH^- groups, which then act as bridging groups for molecular water to adsorb/grow on the surface [100]. The adsorbed water together with the ions of the perovskite at the surface forms then the Helmholtz layer at the perovskite liquid water interface inducing a shift to lower E_B . The shift continues until the area to gas phase water (see Figure 5.10) of adsorbed water molecules becomes equal to the normalized area of TiO_2 after 633 min. Then the peak starts to shift to higher E_B probably due to the water film inducing a chemical shift and/or covering the dipole layer.

The loss of I linked to MAI (or Methylammonium [MA , $CH_3NH_3^+$]) according to equation (B1) and (B2) in Table 5.1 can again be seen in the C 1s spectra. Figure 5.12 shows the C 1s spectra, including the fit results consisting of four species: C_A (adventitious carbon) with an average E_B of (285.6 ± 0.1) eV, $C_B = (286.7 \pm 0.1)$ eV (averaged) attributed to MAI and $C_C = (288.8 \pm 0.1)$ eV (averaged) ascribed most likely to carbonates [88, 102], which are higher in E_B compared to C species of the 300 nm perovskite sample in high vacuum (see subsection 5.2.1) and of the 60 nm sample in UHV (see appendix B.1), but lower in E_B compared to C species of the 60 nm sample in water vapor (see section 5.1). The peak K with an averaged E_B of (293.2 ± 0.1) eV is a K 2p attributed to K adsorbed on the TiO_2 (K/ TiO_2) [84] and is likely a contamination originating from the chamber walls (unrelated experiments involving KOH were carried out in the same chamber prior to this experiment). This contamination increases over time (see right panel Figure 5.12), indicating that K (on TiO_2) is adsorbing on the surface. [Note that for K/ TiO_2 the relative concentration is not normalized to the one of the first data point, but to the second.] Along with K/ TiO_2 (K), the carbonate component (C_C) also increases, whereas adventitious carbon stays constant. The

5.2 Environmental Effects on 300 nm Perovskites

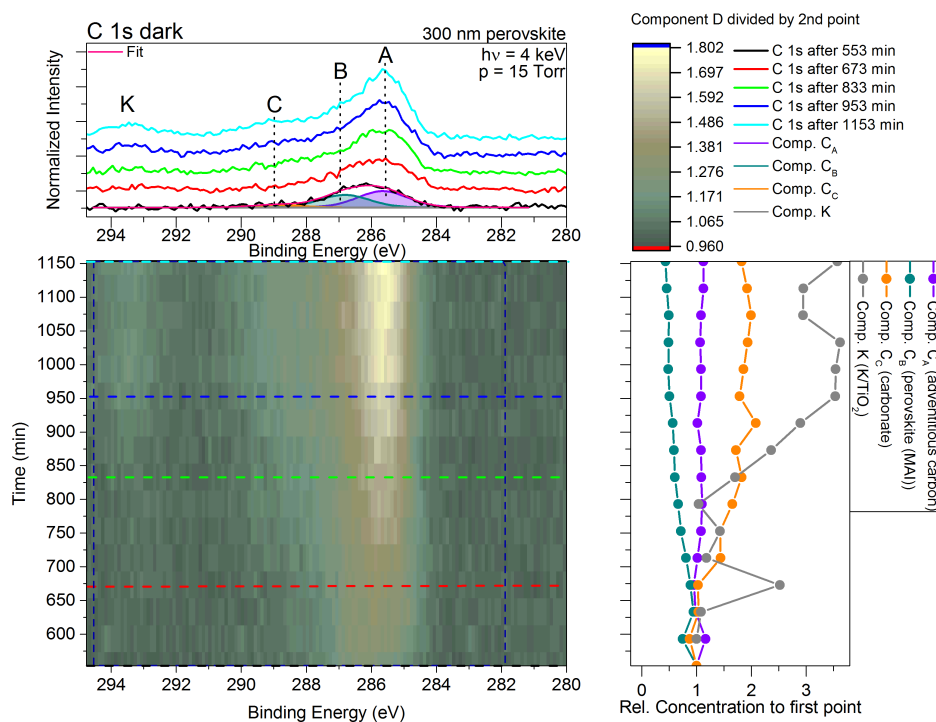


Figure 5.12.: C 1s spectra and fit of 300 nm sample results over time in the dark at 15 Torr. Left bottom panel shows the measured C 1s as a 2D plot and representative selected spectra are shown in the left top panel as a 1D plot including the species from the fits labeled as A, B, C and K. The right panel shows the relative concentration of the four species determined from the fits divided by the relative concentration of the first spectrum of this sequence. The dark blue dashed line in the 2D plots indicates the fit range of the species displayed on the right.

component related to MAI decreases significantly indicating a coverage and signal attenuation by water and/or a loss of MAI. The MAI loss may be due to dilution of the aqueous degradation products in water to a degree that they can not be detected in HAXPES.

In Figure 5.13, Pb 4f spectra including the fit results are displayed. Similar to I 3d, a shift of E_B first to lower and then to higher E_B can be seen, caused perhaps first by a formation of a dipole layer and later by a chemical shift induced by the water film. From the fits, two species can be identified with the following averaged E_B , $Pb_A = (136.85 \pm 0.20)$ eV and $Pb_B = (138.5 \pm 0.2)$ eV, which could be attributed to Pb^0 and Pb in perovskite (or PbI_2), respectively [79, 84, 102]. Considering that the shift between the water and high vacuum Pb species of 0.65 and 0.6 eV for Pb^0 and Pb in perovskite, respectively is due to water adsorption on the surface. Further are the E_B of Pb determined for the 300 nm sample in the dark in water

In-situ Study and Characterization of Environmental Impact on Mixed Halide Perovskite Absorbers

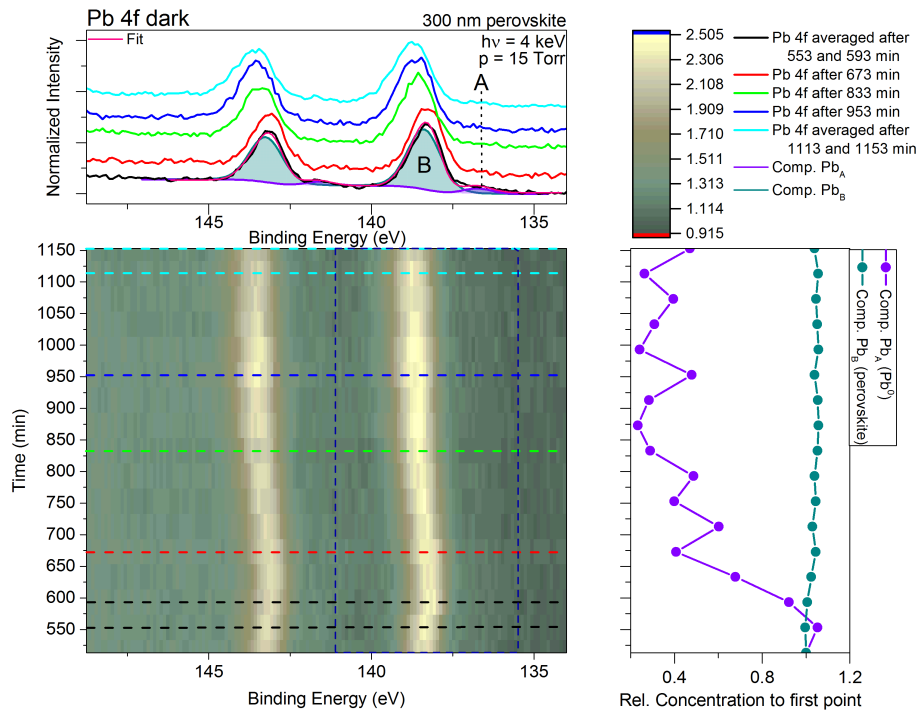


Figure 5.13.: Pb 4f spectra and fit results of 300 nm sample over time in the dark at 15 Torr. Left bottom panel shows the measured Pb 4f as a 2D plot and representative selected spectra are shown in the left top panel as a 1D plot, where the first two and the last two Pb 4f spectra of the sequence were averaged to increase the signal-to-noise ratio. The left panel includes the species from the fits labeled as A and B represented for the first spectra of the sequence not shown in the top panel. The right panel shows the relative concentration of the two species determined from the fits divided by the relative concentration of the first spectrum of this sequence. The dark blue dashed line in the 2D plots indicates the fit range of the species displayed on the right.

vapor lower than for the 60 nm samples. Aside from that the fit reveals also a constant behavior of the relative concentration of perovskite Pb which could be explained by the formation of (more) PbI_2 through dissolving of the perovskite according to equation (B1) in Table 5.1 and the adsorption of water on the sample attenuating the increase of the correlated PbI_2 contribution. The decrease of Pb^0 over time might be due to e.g., formation of PbO , which is expected in E_B between Pb perovskite (or PbI_2) and Pb^0 in Figure 5.13 and might not be resolved due to the low signal-to-noise ratio. Further should the formation of e.g., PbO result in an increase of the Pb perovskite (PbI_2) contribution with time, but this contribution might be partly attenuated due to the growth of a water film. This indicates altogether with the E_B shift to higher energies

5.2 Environmental Effects on 300 nm Perovskites

of the core levels from the perovskite, that molecular water first adsorbs on the perovskite, and then, under consideration of the PEEM results in chapter 4, might spill onto the TiO₂ substrate, slightly decreasing the corresponding O 1s signal. Once the surface (including the pin-holes) is fully covered it stops spreading in a lateral direction after some time and starts to get thicker.

After the sequence, two more Pb 4f spectra, with a better resolution, were measured, indicating a continuation of the trend for the first Pb 4f spectrum; the last Pb spectrum was measured at a different sample spot (spot was changed after 1306 min) showing slightly less perovskite Pb and more Pb⁰ compared to the previous spot (see appendix B Figure B.15 for Pb 4f spectra and Figure B.16 for extended relative concentration plot).

5.2.3. Perovskite in the Light and Water

For the measurements performed under UV illumination with a solar simulator a fresh sample was mounted in air and introduced into the chamber, which was still wet from the previous water in the dark experiment (see subsection 5.2.2). Allowing us to first perform water exposure experiments at low water pressure excluding the water beaker. Later, in order to increase the water amount, a beaker with water was introduced into the chamber; a new spot was chosen and illumination experiments with the sample at a pressure equivalent to water vapor (high water pressure) were performed, the corresponding results can be found in the appendix B (see subsection B.2.2). The results of the low water pressure and illumination experiment will be presented in the following. The zero point of the timescale given in the following spectra is the start of the first scan of the sequence of the respective core level. For the illuminated sample the sequence measurements started immediately after spot optimization. During the experiment in low water pressure the light was turned on after 35 min, after 223 min the measurements continued on a new spot, the light stayed on in total for 293 min and was turned off with measurements continued for another 105 min. These regions are indicated in the figures.

Figure 5.14 shows the measured O 1s spectra and fit results at low water pressure ($p = 1.8 \times 10^{-4}$ to 2.6×10^{-5} Torr) with and without illumination. In the spectra a clear second peak next to the main peak (A) is seen, which was not present in the O 1s spectra recorded in high vacuum in the dark (see Figure 5.6). Through fitting three species could be identified: $O_A = (530.6 \pm 0.1)$ eV (averaged) attributed to TiO₂, $O_B = (531.6 \pm 0.1)$ eV to OH groups and $O_C = (533.15 \pm 0.10)$ eV to molecular water. The presence of molecular water is most likely due to the incompletely dried chamber from the previous water exposure experiment for the perovskite in the dark; during the pump-down sequence some water apparently adsorbed on the sample surface. Therefore it is preferred to speak of perovskite at low water pressure instead of high

In-situ Study and Characterization of Environmental Impact on Mixed Halide Perovskite Absorbers

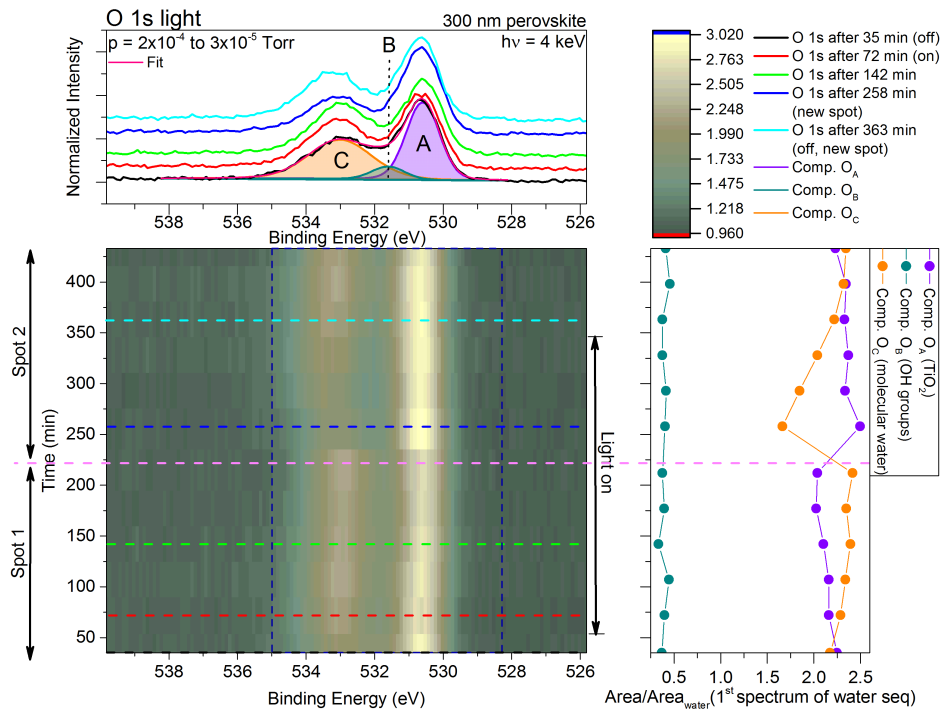


Figure 5.14.: O 1s spectra and fit results of 300 nm sample over time under UV illumination at low water pressure. Left bottom panel shows the measured O 1s as a 2D plot and representative selected spectra are shown in the left top panel as a 1D plot including the species from the fits labeled as A,B and C. The right panel shows the area of each of the three species determined from the fits divided by the area of the gas phase water contribution from the first spectrum of the water sequence. The dark blue dashed line in the 2D plots indicates the fit range of the species displayed on the right. The light magenta dashed line shows the change to a new sample position and the arrow between the left and right panel indicates the time frame were the sample was illuminated.

vacuum. The determined E_B for O 1s at low water pressure and under illumination are slightly higher than for the 300 nm sample in high vacuum (see subsection 5.2.1) and water vapor in the dark (see subsection 5.2.2), likely caused by the chemical shift of adsorbed water.

With elapsing time, molecular water (O_C) increases (see right panel in Figure 5.14), whereas O related to TiO_2 (O_A) slightly decreases, and the component related to OH groups (O_B) stays constant. The same trend is evident when the sample position is changed after 223 min. The new spot, shows after 258 min, a higher TiO_2 related O signal than molecular water, but over time molecular water seem to adsorb again on the surface and the related signal increases. Since the increase/adsorption of molecular water seems to happen under x-ray irradiation, it is

5.2 Environmental Effects on 300 nm Perovskites

very likely that x-rays accelerates the superwetting effect of TiO_2 which happens under UV illumination [108].

Figure 5.14 also indicates a small shift in E_B to lower values over time for the TiO_2 and molecular water peak. When a new spot is illuminated, opposite behavior is observed. The shifts can be ascribed to surface photovoltage (SPV) occurring in photoactive materials under illumination [109], where the direction of the shift in E_B depends on the direction of the dipoles at the perovskite/water interface. Therefore the shift to lower E_B for the first spot might be explained by a difference in surface dipole, caused by the adsorbed water, compared to the new spot with a "drier" sample surface. The new spot is assumed to be drier, since it seems that x-rays are assisting the wetting of the sample surface. The same shift behavior in E_B over time can be

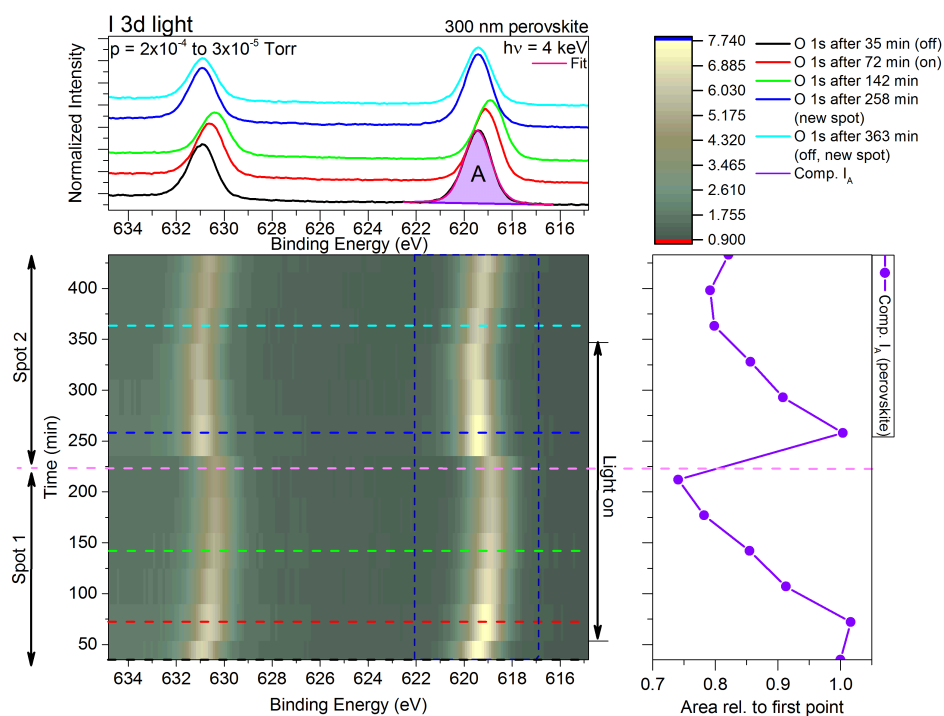


Figure 5.15.: I 3d spectra and fit results of 300 nm sample over time under UV illumination at low water pressure. Left bottom panel shows the measured I 3d as a 2D plot and representative selected spectra are shown in the left top panel as a 1D plot including the species from the fits labeled as A. The right panel shows the area ratio of the species determined from the fits divided by the area of the first spectrum of this sequence. The dark blue dashed line in the 2D plots indicates the fit range of the species displayed on the right. The light magenta dashed line shows the change to a new sample position and the arrow between the left and right panel indicates the time frame were the sample was illuminated.

In-situ Study and Characterization of Environmental Impact on Mixed Halide Perovskite Absorbers

seen for I 3d under illumination (see Figure 5.15), but more pronounced compared to O 1s. That this shift is caused by illumination and therefore by SPV can be clearly seen here: After the light is turned off, the peak starts to shift back to lower E_B and continues to shift for the 105 min probed by x-rays.

Aside from that, the I $3d_{5/2}$ signal decreases for both measured spots; only after turning off the light a slight increase can be seen (see right panel in Figure 5.15). The decrease of the signal might be, as already discussed for the I 3d spectra in the dark in water vapor, due to the degradation of the sample according to equation (C1) and (C2) in Table 5.1. (I can also decrease due to iodine gas being pumped away; I gas results as a degradation product of equation (C4) by formation of Pb^0 , which will be discussed later.) Note that attenuation of the I intensity due to water remnants adsorbing on the surface is in addition to the previously mentioned mechanism happening in the sample. Although the peaks shifts due to SPV, the E_B of I_A can be given in a range between 618.9 and 619.6 eV which is still assumed to be I in a perovskite environment and not a pure chemical shift. Still it has to be considered that for equation (C2) the HI species is supposed to be present in Figure 5.15 as a second additional species, which might be similar for the water and dark case (see subsection 5.2.2), strongly diluted and therefore the corresponding signal below the detection limit. The lower E_B in the given range of I_A is slightly higher than the E_B determined for I_A in high vacuum in the dark, which can be explained by the presence of water remainders.

Figure 5.16 shows the C 1s spectra, which are also affected by the SPV. However compared to the other core level spectra, the C 1s peak shifts for the new spot again to lower E_B under illumination and continues even with light turned off. This behavior might be explained by the loss of the MAI (or MA) contribution and the associated chemical shift canceling out the E_B shift from the SPV. Further, through fitting of the C 1s spectra three species can be identified which can be attributed, similar to the C species of the 300 nm sample in the dark in water vapor and the 60 nm perovskite sample in UHV, to C_A (adventitious carbon) in a E_B range between 284.9 and 285.5 eV, to MAI (C_B) between 286.05 and 286.65 eV and to carbonates (C_C) between 288.1 and 288.7 eV. The component related to MAI (C_B) is decreasing over time, which is expected due to the loss of MAI (or MA) according to equation (C1) and (C2) in Table 5.1, as it has been already discussed for the sample in water vapor in the dark (see subsection 5.2.2). For the new spot, where the light was already on, the MAI component decreases only slightly. For adventitious carbon the opposite behavior to MAI can be seen for both spots. Moreover, the attenuation of the MAI intensity might be partly ascribed to water remnants adsorbing on the surface in addition to the previously mentioned mechanism happening in the

5.2 Environmental Effects on 300 nm Perovskites

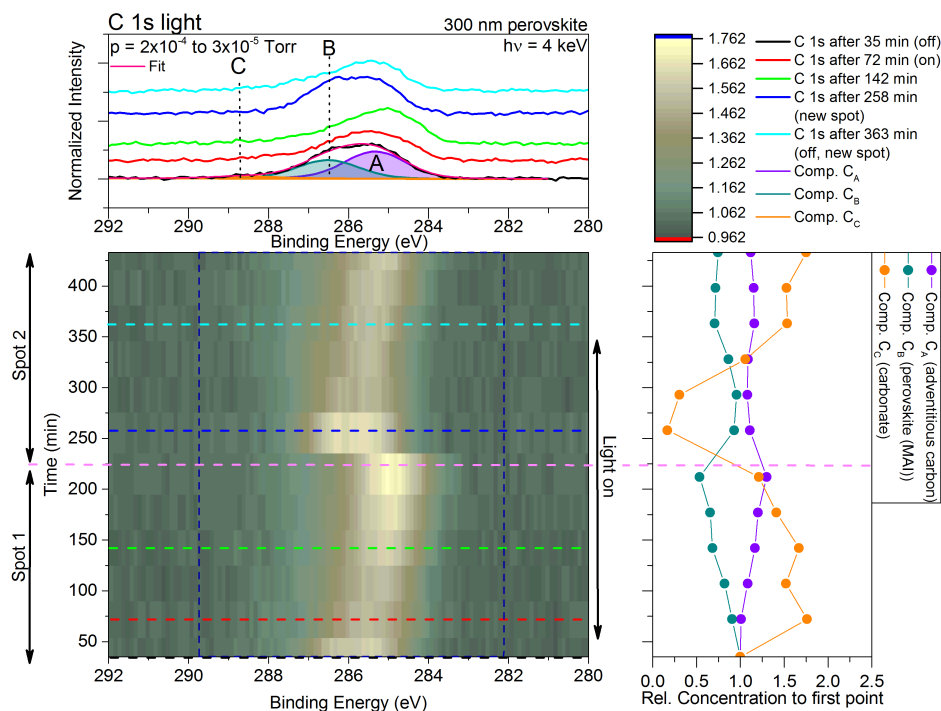


Figure 5.16.: C 1s spectra and fit results of 300 nm sample over time under UV illumination at low water pressure. Left bottom panel shows the measured C 1s as a 2D plot and representative selected spectra are shown in the left top panel as a 1D plot including the species from the fits labeled as A,B and C. The right panel shows the relative concentration of the three species determined from the fits divided by the relative concentration of the first spectrum of this sequence. The dark blue dashed line in the 2D plots indicates the fit range of the species displayed on the right. The light magenta dashed line shows the change to a new sample position and the arrow between the left and right panel indicates the time frame where the sample was illuminated.

sample.

The component for carbonates shows a completely different behavior: first the relative concentration is decreasing and then increasing for the new spot. The decrease might be explained by the presence of the adsorbed water film, which covers the already adsorbed carbonates as it grows. The new spot (see discussion of O 1s in low water pressure and under illumination above) had less molecular water and therefore an incomplete water film, allowing the adsorption of carbonates together with molecular water on the surface.

The C 1s spectra show for two different spots, including three different species, the complex interplay between illumination, water, and x-rays. The changes on the sample seem to depend

In-situ Study and Characterization of Environmental Impact on Mixed Halide Perovskite Absorbers

on the "pre-conditions" of the sample spot when it gets probed with x-rays.

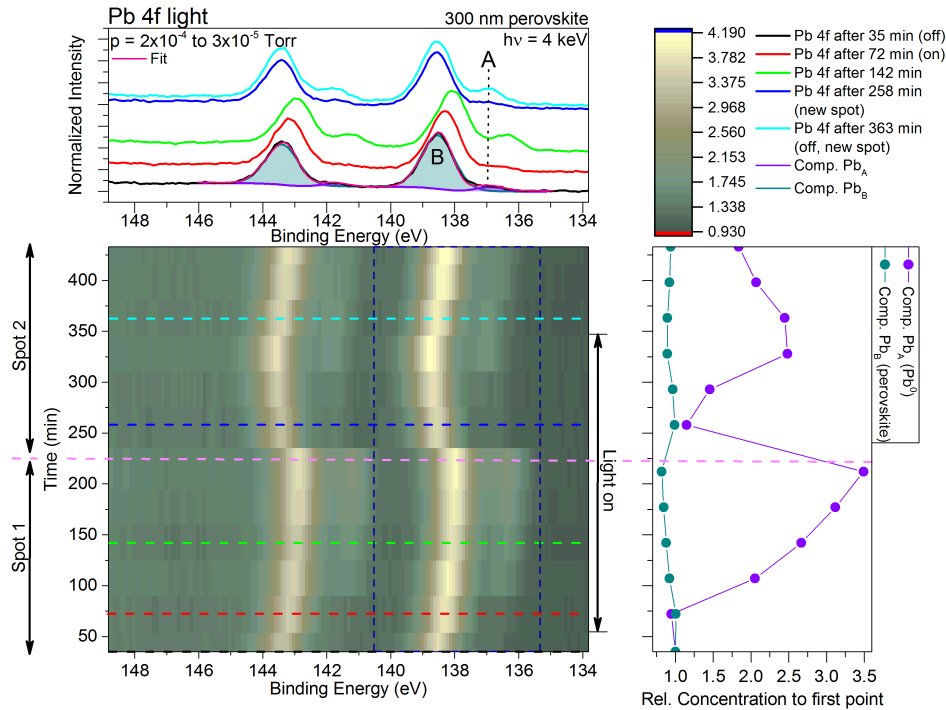


Figure 5.17.: Pb 4f spectra and fit results of 300 nm sample over time under UV illumination at low water pressure. Left bottom panel shows the measured Pb 4f as a 2D plot and representative selected spectra are shown in the left top panel as a 1D plot including the species from the fits labeled as A and B. The right panel shows the relative concentration of the two species determined from the fits divided by the relative concentration of the first spectrum of this sequence. The dark blue dashed line in the 2D plots indicates the fit range of the species displayed on the right. The light magenta dashed line shows the change to a new sample position and the arrow between the left and right panel indicates the time frame were the sample was illuminated.

The Pb 4f spectra in Figure 5.17 show a clearer correlation between illumination, x-rays, and water. Fitting of the spectra shows two species which can be attributed, as before, to Pb^0 for Pb_A in a E_B range from 136.4 to 137.1 eV and to perovskite Pb for Pb_B from 138.0 to 138.7 eV. Similar to O 1s and I 3d shifts the E_B of the Pb 4f over time due to SPV. Note that identical to the other core levels, the lower E_B range given for Pb is slightly higher than for Pb in high vacuum in the dark, due to the presence of water. Aside from the shifts, a clear increase of metallic Pb can be seen as soon as the light is turned on, indicating degradation of the PbI_2 into Pb^0 and I_2 according to equation (C4) in Table 5.1. That is further supported

5.2 Environmental Effects on 300 nm Perovskites

by the decrease of the perovskite Pb (PbI_2) signal, which behaves opposite to Pb^0 , but its decrease is much less than the increase of Pb^0 . The difference might be partly explained by the lower contribution of the plasmonic loss structure in Pb^0 , relative to PbI_2 , perovskite, or Pb oxide, which is not included in the fits. In addition, for the formation of Pb^0 , part of the perovskite needs to have already degraded into PbI_2 and MAI. These processes, observed in Pb 4f, seems to be accelerated/mediated by x-rays, since the new spot shows a lower initial relative concentration of metallic Pb which increases with time. As soon as the light is turned off, metallic Pb decreases. Therefore a clear correlation between x-rays and UV induced formation of Pb^0 can be identified. The formation of the Pb^0 species in this case appears to be a non-permanent change, after the light is turned off the corresponding contribution decreases likely due to e.g., PbO formation similar to the perovskite in water vapor in the dark (see subsection 5.2.2).

Moreover, the contributions of I, MAI (C) and Pb perovskite decrease with increasing molecular water contribution under illumination due to degradation and additional water adsorption. The O 1s signal, related to TiO_2 , decreases solely due to water adsorption. This makes it difficult to estimate where the water adsorbs on the sample, which is even further hindered by the fact that water before the illumination experiment could have adsorbed on the perovskite surface in the absence of light according to subsection 5.2.2. Therefore it is assumed that for the low water pressure experiment water was already adsorbed on the perovskite and might under illumination preferentially adsorb on the TiO_2 . The TiO_2 signal is slowly decreasing due to the low water pressure in the chamber. Nevertheless, additional water may absorb on the perovskite surface.

5.2.4. Degradation of 300 nm Perovskite in Ambient Environment

In this subsection the possible degradation mechanism will be further discussed. Figure 5.18 shows an overview of all relative compositions for the relevant perovskite core levels over the relative concentration of molecular water. Only for Figure 5.18 a) the plot over relative concentration of C=O bonds is given, since this sample had no measurable water adsorbed.

In the previous sections, the behavior of the components depending on the time of exposure to vacuum/water and illumination as well as spot change have been described, creating a complex picture of the overlapping and competing interactions of the material with UV light, water vapor and x-rays. The additional illumination with UV light and the growing water film do not only shift the peaks due to SPV, the water film also influences the intensity, hindering the identification of a degradation through a decrease/increase in intensity of the respective core level peaks. The composition plot (see Figure 5.18) allows the decoupling of the intensity

In-situ Study and Characterization of Environmental Impact on Mixed Halide Perovskite Absorbers

variations from the illumination, assuming that the fluctuation in intensity affects all core levels similarly. The plot further allows comparison of the relative compositions of the core levels for all experimental runs using a common factor (molecular water). Starting with Figure 5.18 a),

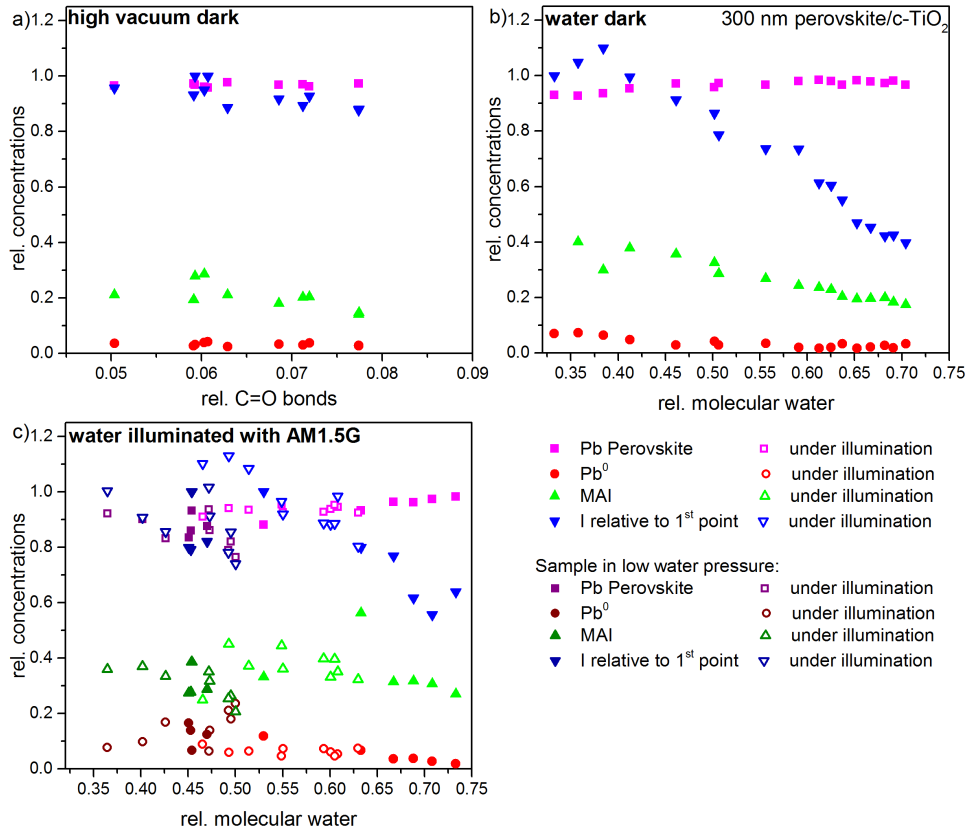


Figure 5.18.: Shows relative concentrations of Pb perovskite (PbI_2), Pb^0 , MAI (carbon) and I over relative concentration of molecular water (or for "a)" of C=O bonds) for 300 nm perovskite in a) high vacuum and dark, b) water vapor and dark, c) water and under illumination at AM1.5G. Note that I is not given as relative concentration but relative to first data point (area) as there is only a single I 3d species. The open symbols mark the illuminated data points for c).

a constant behavior (within the scatter of the data) of Pb perovskite (or similar PbI_2), Pb^0 , I and MAI over the relative concentration of the C=O species can be seen. According to equation (A) in Table 5.1, it is expected to see the formation of $\text{CH}_3\text{NH}_2(\text{g})$, $\text{HI}(\text{g})$ and PbI_2 , where the gaseous components are assumed to be pumped away. The latter would result in a decrease of the I and MAI (or MA) related component, which is not seen in Figure 5.18 a), indicating that the perovskite is stable in high vacuum in the dark. This is further corroborated by the absence of the HI species in the I 3d spectra (see Figure 5.7), disagreeing with proposed degradation

5.2 Environmental Effects on 300 nm Perovskites

mechanism in equation (A).

For the sample in water vapor (high water pressure) in the dark it is expected, according to equation (B1) and (B2) in Table 5.1, that the final reaction products are $\text{CH}_3\text{NH}_2(\text{aq})$, $\text{HI}(\text{aq})$ and PbI_2 . In Figure 5.18 b)), a fast decrease of I and a slow decrease of MAI (or MA) can be seen, indicating the loss of CH_3NH_2 and HI with increasing relative concentration of molecular water, which can be explained by the likely dilution of the aqueous degradation products in water to a degree that they can not be detected in HAXPES. This would also explain why the corresponding species do not show up in Figure 5.11 and 5.12, because their contribution to the spectra would be below the detection limit. Pb in the perovskite environment (or similar PbI_2) is constant within the scatter, and Pb^0 is slightly decreasing with increasing relative concentration of molecular water. The constant behavior of the perovskite (or similar PbI_2) can be explained by the transition from perovskite to PbI_2 , which are likely indistinguishable in this experiment and the adsorption of water on the sample attenuating partly the increase of the PbI_2 contribution. Thus the experiment in water vapor in the dark is consistent with degradation according to equation (B1) and (B2) in Table 5.1. Further, Pb^0 was already present on the sample, and its decrease in water vapor might be explained by some back reaction, e.g., formation of PbO. The PbO line would be found between the metallic and perovskite Pb 4f peaks in Figure 5.13. Due to the low signal-to-noise ratio and the (probably) low amounts of PbO (see slight decrease of Pb^0), the corresponding signal contributing to the spectra would be very low and therefore might not be resolved in the spectra.

Figure 5.18 c) shows the results of the experiment under illumination in water, which can be split into contributions from the low water pressure experiment, presented by the darker colored data points (see legend in Figure 5.18), and the high water pressure experiment, where the beaker was introduced, in order to increase the water amount. Additionally, the data points related to illumination are marked by open symbols and solid symbols present the data points where the light was turned off. In Figure 5.18 c) it can be clearly seen that the low water pressure data points have lower molecular water on the surface, as expected by the experiment, and they then overlap with the data points from the high pressure water experiment, with increased water content, at higher molecular water contributions. Note that the dip around 0.46 for Pb^0 (and a spike for the other core levels) belongs to the values of the measurements at the beginning of the sequence and for a new spot with light turned off. Aside from that, for low water pressure Pb from perovskite (or PbI_2) and I decrease. MAI (or MA) shows only a slight decrease at higher molecular water contributions, and Pb^0 significantly increase. According to equation (C1-C4) in Table 5.1, the formation of Pb^0 is expected and can be confirmed, further supported by the decrease of Pb perovskite (or similar PbI_2) corresponding to the degradation according

In-situ Study and Characterization of Environmental Impact on Mixed Halide Perovskite Absorbers

to equation (C1) and (C4). The degradation of MAI according to equation (C2) is reflected by the decrease of I (HI) and the related MAI (or MA) contribution being diluted, whereas the degradation products according to (C3), which are H_2 and I_2 , might not be distinguishable in Figure 5.15. Additionally, the degradation of PbI_2 according to equation (C4) would also lead to a decrease in I, since iodine gas can be pumped away. It therefore seems that the data are in agreement with the proposed degradation mechanism for water and illumination in Table 5.1. For the higher water pressure experiment (see corresponding data in the appendix B.2.2), it can be stated that the behavior of the core levels with the light off at high molecular water contribution correlates with the behavior of the water in the dark experiments, and therefore the same degradation mechanism takes place. For the high water pressure exposure experiment under illumination, formation of Pb^0 is again expected according to equation (C1) and (C4) in Table 5.1, but it appears that Pb^0 decreases and Pb perovskite (or PbI_2) stays constant within the scatter of the data in Figure 5.18 c). This could be due to reduction of the formed Pb^0 according to equation (C4) through reaction with water to form e.g., PbO , accounting to the Pb perovskite (or PbI_2) relative concentration and resulting further in a constant Pb perovskite (or PbI_2) contribution in Figure 5.18 c) (under consideration of additional water adsorption). Additionally, it can be seen that I decreases, which is expected by the degradation of MAI, HI and PbI_2 according to equation (C2-C4) in Table 5.1, whereas no conclusion can be drawn from MAI (or MA) Figure 5.18 c) since it scatters too much. It might be possible for MAI (or MA) to be diluted and still be present on the sample surface, slowing down the decrease of that contribution with increasing molecular water contribution. Therefore, for the high water pressure experiment under illumination the degradation according to Table 5.1 for water vapor under illumination can not be confirmed, but cannot be excluded either.

5.3. 60 nm vs. 300 nm Perovskite

In this chapter the degradation of perovskite in UHV(or high vacuum)/water and in the dark/under illumination was studied. For the 60 nm sample the degradation of the perovskite in water vapor with non-defined illumination was mainly driven by the x-rays (radiolysis) forming Pb^0 , in which the initial relative concentration of molecular water on the surface and the exposure time were not the primary influence on the degradation. This indicates that the 60 nm perovskite is not stable in a water vapor environment when interacting with x-rays.

The 300 nm perovskite sample shows a different behavior than the 60 nm sample: The degradation of the 300 nm samples is mainly driven by the decomposition of the perovskite into MAI

5.3 60 nm vs. 300 nm Perovskite

and PbI_2 in the presence of water. Further, PbI_2 decomposes into Pb^0 in the presence of UV light and x-rays for low water pressures.

The difference in the degradation pathways between the samples described here might not only be ascribed to the difference in thickness alone, but also to the morphology. The morphology for the 300 nm sample is shown in Figure 4.1 and was already discussed in chapter 4. The 60 nm sample the surface (see Figure B.7 in the appendix B.1) shows approximately the same coverage of the substrate compared to the 300 nm sample, but with smaller islands and a lower thickness. This could lead to the conclusions that island diameter plays a role in the stability of the perovskite or that the precursor solution was not completely converted into perovskite, representing a sample with an intermediate surface similar to the *intermediate* area described in chapter 4 for thinner parts of the 300 nm sample, where Pb^0 was detected and the correlated presence of PbI_2 was suspected. It might be possible that TiO_2 as a photocatalytic material and ETM supports the degradation of the sample in water, which means for the 60nm that the lower thickness and different morphology offers a higher interaction volume for the x-rays with the TiO_2 at the TiO_2 /perovskite interface.

6. Inorganic Pb-free CsSnBr₃ Perovskites

Completely inorganic CsSnX₃ based-perovskites (with X = e.g., I, Br or Cl) are a relatively new absorber class attempting a different approach for solving two problems: UV light and humidity instability of hybrid organometallic perovskites, and the toxicity of Pb. At the moment this new class leads to low efficiencies due to the fast oxidation of Sn [28, 29]. Adding SnF₂ to the precursor solution seems to (partially) inhibit the oxidation of Sn, improving the performance of the resulting solar cell [25], but its impact on the chemical and electronic structure as well as on the chemical composition is not fully understood.

In this chapter, HAXPES results of wet-chemical deposited CsSnBr₃/c-TiO₂/FTO/glass samples with and without SnF₂ additive are presented, and the role of SnF₂ treatment and halide composition is discussed. HAXPES measurements with $h\nu = 2$ keV were performed to gain insight into the electronic and chemical properties of the Pb-free perovskite absorber materials.

6.1. Results and Discussion

6.1.1. Chemical Structure of CsSnBr₃ Perovskites

Figure 6.1 shows the shallow core levels of CsSnBr₃/c-TiO₂/FTO/glass without (sample set A) and with (sample set B) SnF₂ for five different batches, where the index in Figure 6.1 correspond to the batch number. The five batches for each sample set were prepared sequentially at the Weizmann Institute of Science (group of G. Hodes and D. Cahen) in Israel according to the same recipe presented in Ref. [25] (see also subsection 2.3.1) to test reproducibility of the measurements and randomize effects from sample shipping/handling.

The shallow core level spectra in Figure 6.1 show all expected CsSnBr₃ core levels, including the core levels associated with the c-TiO₂ substrate. Despite some variation between the batches, comparing the two sample sets (A and B) shows that adding SnF₂ to the precursor

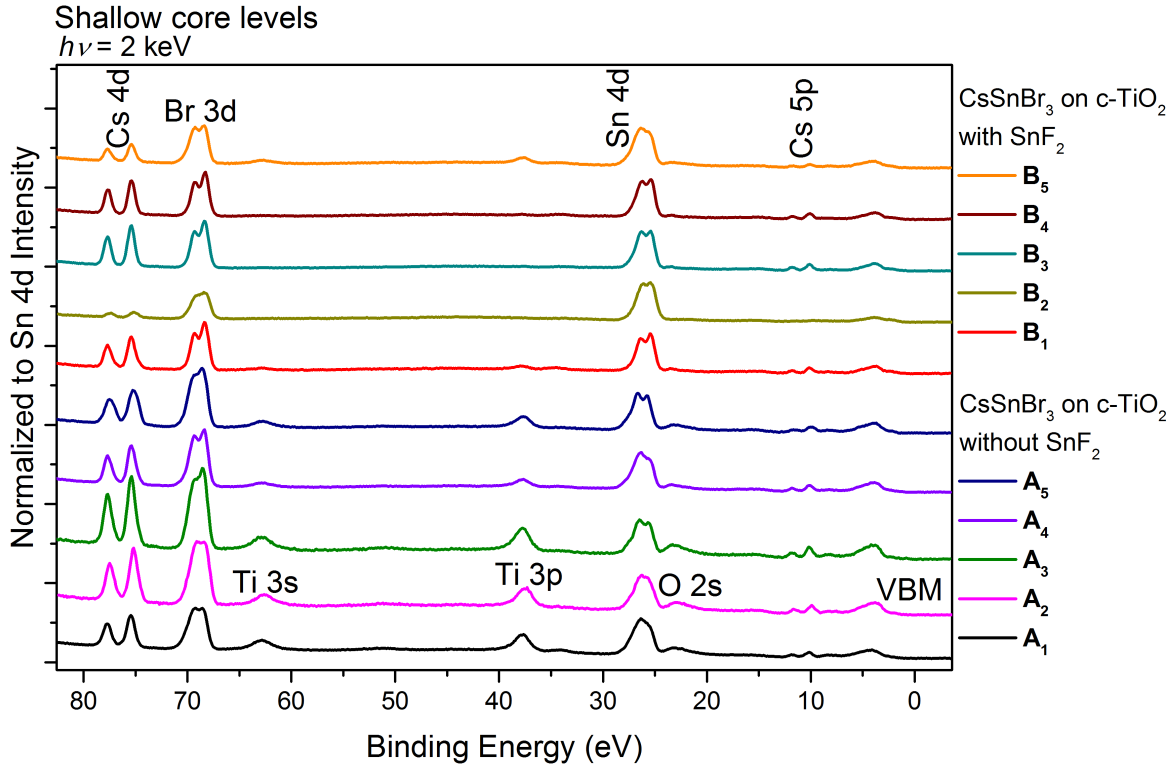


Figure 6.1.: HAXPES spectra of the shallow core level, of wet-chemically deposited CsSnBr₃ measured with an excitation energy of $h\nu = 2$ keV, respectively. Spectra have been background subtracted and then normalized to Sn 4d peak height, vertical offsets are added for clarity.

solution seems to increase coverage, as indicated by a decrease of the Ti 3p signal relative to the core levels of the absorber.

In the following, only the data of samples from batch 1, 3 and 5 will be further discussed. Due to the absence/presence of the F 1s signal for sample B₂/A₄ it is concluded that something went wrong during sample preparation or transport (see Figure C.1 a) in the appendix C). The detail spectra excluded from discussion in this chapter can be found in the appendix C for completeness.

Differences in the peak shapes of the Sn 4d, Br 3d and Cs 4d shallow core levels (see respective detail spectra in Figures 6.2, 6.3 and 6.4) indicate the existence of multiple species which is confirmed by fitting the core levels with Voigt functions using Unifit 2016 [62], by keeping the Lorentzian and Gaussian full width half maximum (FWHM) fixed for the same core levels and setting the spin-orbit splitting fixed to 1.1 eV for Sn 4d [110], to 1.05 eV for Br 3d [88] and to 2.3 eV for Cs 4d [111]. In addition, a Shirley background was used for fitting.

6.1 Results and Discussion

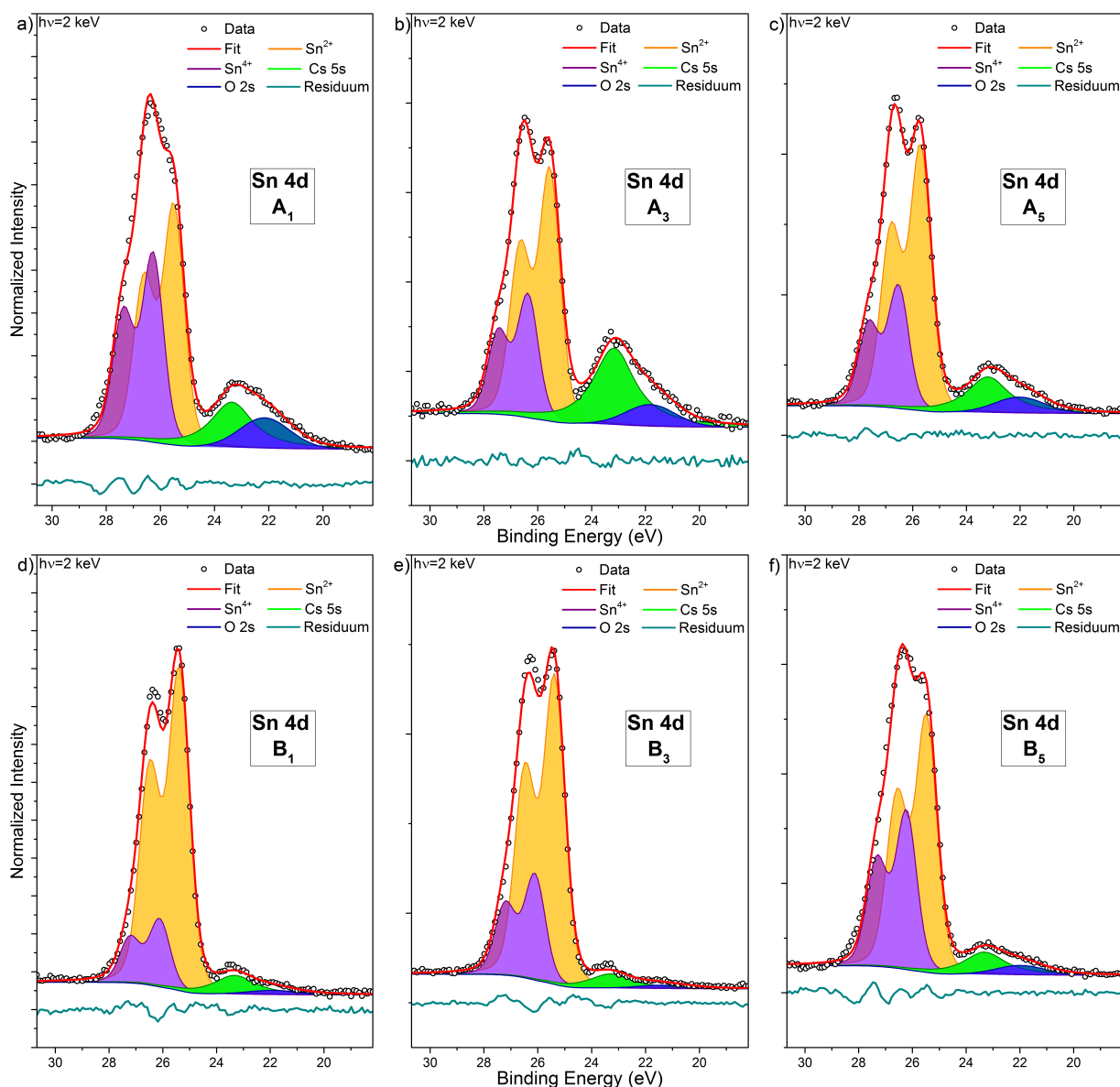


Figure 6.2.: HAXPES Sn 4d detail spectra (including fit analysis) of the CsSnBr₃ samples without SnF₂ (A₁, A₃, A₅) and with SnF₂ (B₁, B₃, B₅) from the shallow core levels in Figure 6.1. The raw data is shown as open circles, the spectra were normalized by the background intensity at the lower E_B around E_F and the resulting fits are given as red lines. The different contributions due to spin-orbit splitting and different Sn species are given as shaded areas in orange (Sn²⁺) and purple (Sn⁴⁺). The corresponding residuum is shown below each spectrum and the spectral background fitted using the Shirley background.

Note that the shallow core level spectra in Figure 6.1 were normalized by subtracting the background around E_F , since the background above E_F arises from scattering of photoemission lines excited by third order (6 keV) photons. Afterwards the spectra were normalized to the Sn 4d line. For the fits used to calculate relative contributions the shallow core levels were normalized differently; they were normalized by the background intensity around the Fermi level. For comparison of the ratios between the different shallow core levels of one sample the contribution from scattering to the background stays constant and thus cancels out.

Figure 6.2 shows the curve fit results for the Sn 4d spectra of the different batches of sample set A and B, respectively, clearly indicating two species of Sn (a non- and oxidized component) [110], with varying contribution of the components to the spectrum over the batches. The main contribution of Sn 4d_{5/2} (orange area in Figure 6.2) for sample set A and B at an averaged E_B of (25.59 ± 0.10) eV and (25.42 ± 0.10) eV respectively, can be attributed to Sn²⁺ of CsSnBr₃. The secondary species, at an averaged E_B of (26.39 ± 0.1) eV and (26.15 ± 0.1) eV for sample set A and B respectively, can be ascribed to oxidized Sn (Sn⁴⁺) [110]. The chemical shift between both Sn 4d species seems to vary between sample sets A and B, being in average (0.80 ± 0.10) eV and (0.73 ± 0.10) eV, respectively. Considering a fitting error of ± 0.10 eV, the chemical shift is in agreement with the value of (0.73 ± 0.05) eV [110] reported in literature for the chemical shift between Sn²⁺ and Sn⁴⁺ in Sn oxides. For sample set A and B, the O 2s signal around 22 eV (averaged) can be attributed to O from the TiO₂ substrate and the peak around 23.2 eV to Cs 5s states from the perovskite (despite the slightly higher E_B compared to CsBr) [84]. Note that CsSnBr₃ tends to form metallic Sn under x-ray radiation as it is reported by Gupta et al. [25]. The metallic Sn 4d component (Sn⁰) would be then found in the O 2s and Cs 5s region, overlapping with the respective core levels. However no Sn⁰ signal can be observed in the more prominent and not overlapping Sn 3d spectra (see Figure C.2 in the appendix), indicating an absent or insignificant contribution of Sn⁰ to the Sn 3d spectrum.

The resulting E_B for every batch from the Sn 4d fits presented in Figure 6.2 and the other shallow core levels (see Figure 6.1) are summarized in Table C.1 (see appendix C).

The peaks of the Sn²⁺ states, in Figure 6.2, are represented by an orange area, and the Sn⁴⁺ states by a purple area. The Sn⁴⁺ is less predominant (relative to the orange area) for sample B₁ and B₃, indicating that oxidation is suppressed by adding SnF₂ to the precursor solution [29]. However, sample B₅ has a slightly higher Sn⁴⁺ area than A₅, indicating an increased oxidation which will be further discussed below.

In addition to the Sn species, in Figure 6.2 O 2s and Cs 5s states contribute to the spectrum. The presence of O 2s mainly relates to the incomplete coverage of the c-TiO₂, since it scales with coverage (Ti 3p) (see Figure 6.1) and not with Sn⁴⁺. This can be seen from the Sn 4d fits,

6.1 Results and Discussion

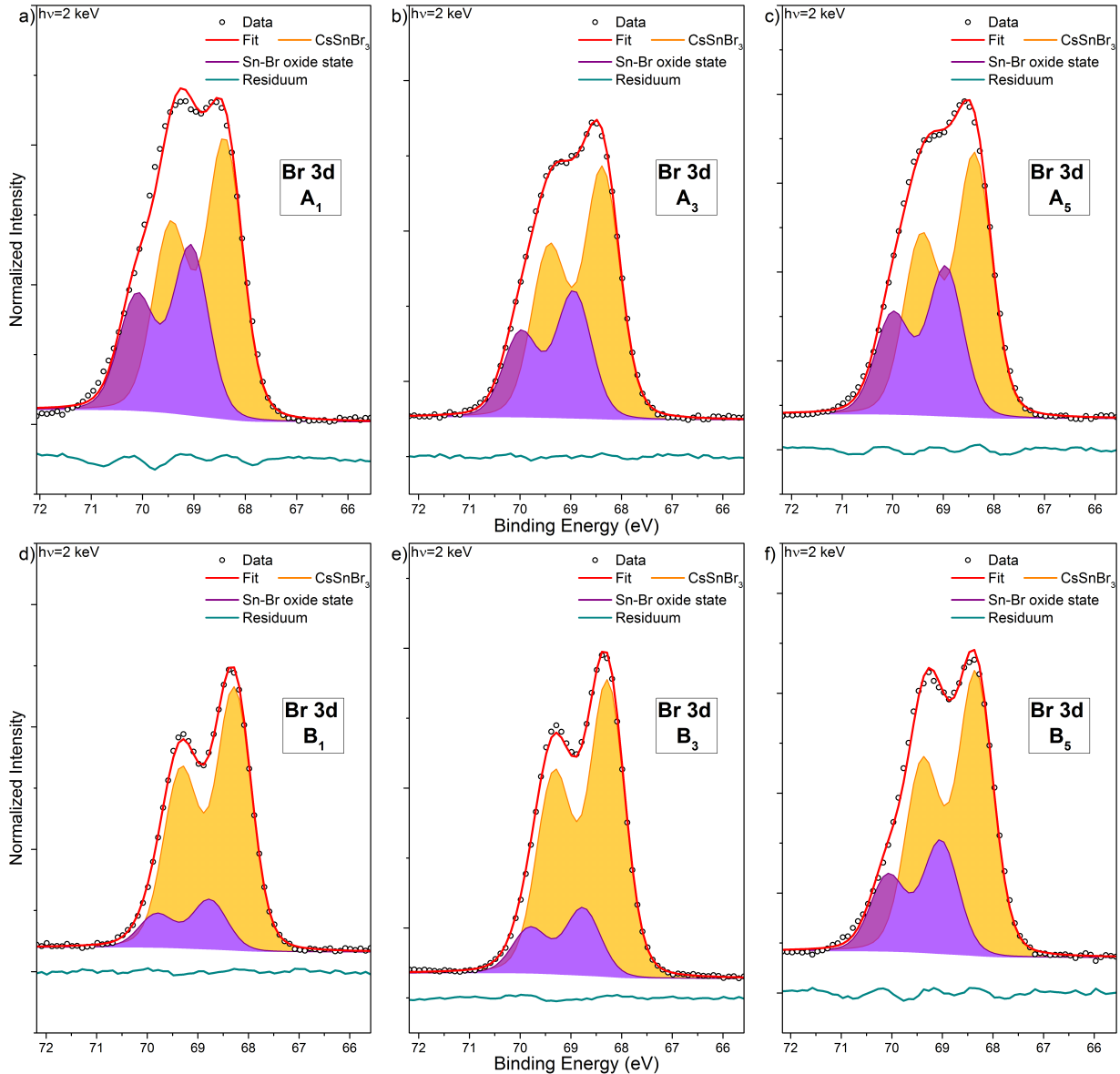


Figure 6.3.: HAXPES Br 3d detail spectra (including fit analysis) of the CsSnBr_3 samples without SnF_2 (A_1 , A_3 , A_5) and with SnF_2 (B_1 , B_3 , B_5) from the shallow core levels in Figure 6.1. The raw data is shown as open circles, the spectra were normalized by the background intensity at the lower E_B around E_F and the resulting fits are given as red lines. The different contributions due to spin-orbit splitting and different Br species are given as shaded areas in orange (CsSnBr_3) and purple (Sn-Br oxide state). The corresponding residuum is shown below each spectrum and the spectral background fitted using the Shirley background.

O 2s (blue area) is for sample set B reduced compared to A (relative to Sn 4d) independent from the change of Sn⁴⁺. Similar to O 2s, the Cs 5s signal (green area) for sample set B is reduced, indicating less Cs compared to Sn for sample set B. Suggesting that adding SnF₂ leads either to a Cs depletion or Sn accumulation at the sample surface. A trivial explanation would be the SnF₂ being majority present at the sample surface, attenuating the CsSnBr₃ photoemission lines, since the Cs/Sn⁴⁺ ratio also changes, the reality is likely to be more complex.

In Figure 6.3 the Br 3d detail spectra (including fit analysis) is shown. The main (I) contribution of Br 3d_{5/2} (orange area), at an averaged E_B of (68.4 ± 0.1) eV and (68.3 ± 0.1) eV for A and B respectively, can be ascribed to a Cs-Br chemical environment (as in CsSnBr₃) [84]. The second (II) species (purple area) at an averaged E_B of (69.0 ± 0.1) eV and (68.85 ± 0.10) eV for A and B respectively, is attributed to a Sn-Br oxide [112]. Similar to the Sn 4d spectra, the purple area attributed to an oxide is reduced for sample set B, implying that SnF₂, which inhibits the oxidation of Sn (i.e., the conversion of Sn²⁺ to Sn⁴⁺), also seems to affect the formation of the second (oxidized) species of Br (II) (i.e., reduces/limits). As discussed before, sample B₅ shows a higher Sn⁴⁺ component as for A₅, but the fit analysis of Br 3d indicates a decrease of the purple area for B₅ (Br component related to Sn⁴⁺), suggesting that an additional surface contamination/oxidation is attributing to the Sn⁴⁺ contribution to Sn 4d. Nevertheless sample B₅ has the highest Sn-Br oxide contribution among series B. Further, the Br 3d spectrum of sample A₁ shows a slight deviation between fit and data, in particular at high E_B, pointing to the possible presence of a third species as suggested by Jung et al. [112].

For Cs 4d_{5/2} in Figure 6.4 the main (I) contribution (orange area) at an averaged E_B of (75.4 ± 0.1) eV for Sample set A and B might be attributed to Cs-Br bonds as in CsSnBr₃ [84]. The identification of the secondary (II) contribution at the lower E_B site (purple area) at an averaged E_B of (74.9 ± 0.1) eV and (74.8 ± 0.1) eV for sample set A and B respectively, is not that straight forward. A Cs oxide could be expected in analogy to Sn and Br, but according to literature its E_B would be at the higher E_B site of the Cs (I) component [84]. However, it has also been reported that in O₂-dosing experiments the Cs core level shifts to lower E_B [113]. Therefore it is proposed that Cs(II) is an oxidized species.

To further evaluate the impact of SnF₂ on the chemical compositions, the elemental ratios were calculated by correcting the areas of Sn 4d_{5/2}, Br 3d_{5/2} and Cs 4d_{5/2}, determined from the fits, by the respective photoionization cross section of the corresponding element [63, 64]. In Table 6.1 the averaged elemental ratios for CsSnBr₃ without and with SnF₂, including the expected theoretical values, are given. The elemental ratios for the single batches can be found in the appendix C (see Table C.2) for completeness.

6.1 Results and Discussion

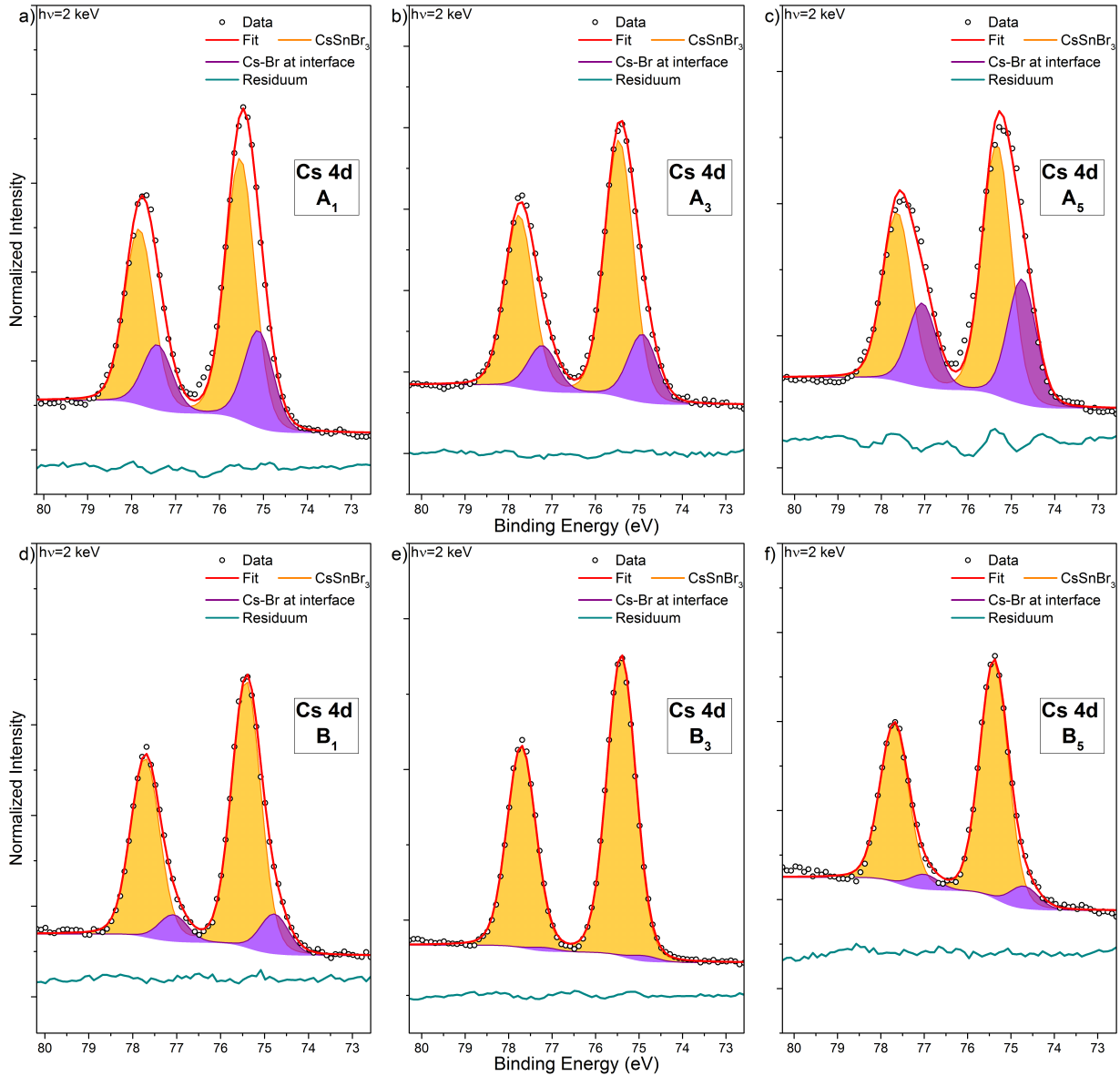


Figure 6.4.: HAXPES Cs 4d detail spectra (including fit analysis) of the CsSnBr₃ samples without SnF₂ (A₁, A₃, A₅) and with SnF₂ (B₁, B₃, B₅) from the shallow core levels in Figure 6.1. The raw data is shown as open circles, the spectra were normalized by the background intensity at the lower E_B around E_F and the resulting fits are given as red lines. The different contributions due to spin-orbit splitting and different Cs species are given as shaded areas in orange (CsSnBr₃) and purple (Cs-Br interface species). The corresponding residuum is shown below each spectrum and the spectral background fitted using the Shirley background.

The Cs/Sn and Br/Sn ratios show an overall decrease when SnF₂ is added, which is in agreement with the decrease of the theoretical values. Nevertheless, the Cs/Sn ratio seems to decrease more than the Br/Sn ratio when SnF₂ is added, comparing a decrease by 44% for Cs with 36% for Br. This difference indicates a possible deficiency or inhomogeneous distribution of Cs at the surface. Further, it can be seen that the experimental determined ratios deviate from the theoretical ratios differently for Cs and Br of sample A: Cs/Sn has a deviation of 46% from the theoretical value, whereas Br/Sn has only a deviation of 23%. This indicates that the surface is already Cs deficient for CsSnBr₃ without SnF₂, which is further enhanced when SnF₂ is added. Further the F/Sn ratio seems to be smaller by 61% compared to the theoretical value, indicating that less F of the initial 20 mol% SnF₂ used in the precursor solution (see subsection 2.3.1) is left in the sample. The F/Sn ratios presented here were calculated similar to the other elemental ratios, but data from the lab (see appendix C) were used for the fits of F 1s and Sn 3p_{3/2}. Note that the experimental ratios are always smaller than the theoretical ratios, the reason for this deviation is, especially for Br, uncertain.

Table 6.1.: Averaged chemical compositions, calculated from the fits of wet-chemically deposited CsSnBr₃ samples without (A) and with (B) SnF₂ prepared sequentially in different batches. The expected theoretical values are given in squared brackets.

	Cs/Sn	Br/Sn	F/Sn
A	(0.54 ± 0.25) [1]	(2.31 ± 0.73) [3]	-
B	(0.30 ± 0.12) [0.83]	(1.47 ± 0.12) [2.5]	(0.128 ± 0.089) [0.33]

6.1.2. Electronic Structure of CsSnBr₃

The results of the chemical analysis of the CsSnBr₃ allows us to further discuss the electronic structure of this absorber class. Figure 6.5 a) shows the VB spectra of the CsSnBr₃ samples, formed by hybridized Br 4p and Sn 5s states [114]. The VBM were determined by linear extrapolation of the leading edge in the VB spectra and are given in Figure 6.5 a) as well for the different sample sets. The VBM of the bare c-TiO₂ was determined to be (3.5 ± 0.1) eV, which is higher than the value of 3.3 eV in literature for c-TiO₂ [68] and is nearer to that of mesoporous TiO₂ which can have a VBM of 3.6 eV [115]. A possible explanation for the discrepancy would be that the c-TiO₂ layer is composed of nano crystalline TiO₂ and has therefore a higher VBM (and band gap), since the latter depends on the grain/crystal size [116]. The comparison between sample sets A and B demonstrates some spectral differences. All VB spectra of sample set A have a more pronounced feature around 8 eV compared to B. This

6.1 Results and Discussion

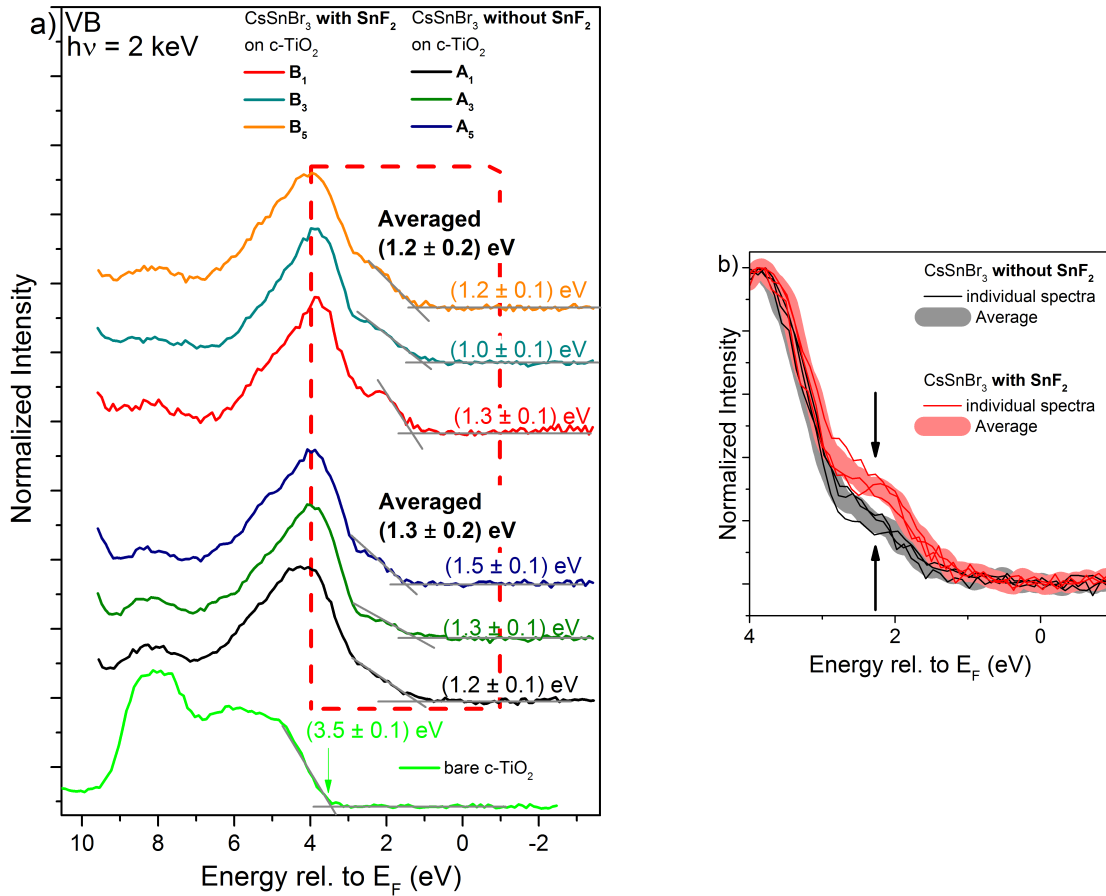


Figure 6.5.: a) VB spectra of wet-chemically deposited CsSnBr₃ and bare c-TiO₂ (including linear extrapolation of VBM). b) Magnified view of the VBM onset for the CsSnBr₃ samples A and B, already including subtraction of the TiO₂ signal and averaged spectra of sample set A and B. All spectra are normalized to the maximum.

feature is ascribed to the O 2p derived density of states (DOS) of TiO₂ [117] [see bare c-TiO₂ spectra in Figure 6.5 a) for comparison] and are visible in the VB spectra due to incomplete coverage by the perovskite. The decrease of this feature in the spectra of sample set B is, like the decrease of the Ti 3p signal, an indication of a thicker layer or better coverage of the substrate, which corroborates the attribution to O 2p derived states from the substrate.

Another feature around 2 eV is enhanced for sample set B compared to A (indicated by black arrows in Figure 6.5 b)). The increase of DOS around 2 eV can be related to the SnF₂ treatment. This can be clearly seen in Figure 6.5 b), which shows a magnified view of the VBM (with substrate signal subtracted¹) for all three batches from sample set A and B without the offset

¹The substrate signal was eliminated by subtracting a scaled TiO₂ VB spectrum from all the VB spectra of

including an averaged spectra for both sample sets. According to literature [114], these valence states around 2 eV are dominated by Sn 5s and influenced by changes in the oxidation state of tin [110, 118]. In our case, an increase of Sn 5s-dominated DOS when reducing the oxidation (Sn⁴⁺ states) can be observed.

The increase of Sn 5s states by adding SnF₂ can be explained by a redistribution of DOS of unoccupied Sn 5s derived levels from the bottom of the conduction band (as e.g., observed for SnO₂ [Sn⁴⁺]) to the occupied VB (as e.g., observed for SnO [Sn²⁺]) to include the additional electrons located at the tin cation [118, 119]. This however shifts the VB(M) closer to the Fermi level, which is reflected in Figure 6.5 a) by the (small) averaged shift to lower VBM when going from sample set A to B. This trend is in agreement with literature [25]. Furthermore the VBM shift closer to the Fermi level seems to correspond to a shift to smaller E_B of Sn²⁺ (see Figure C.6 in appendix C) which can be again attributed to a change in oxidation/chemical environment. Note that the determined averaged VBM of sample set A and B differ only by 0.1 eV, which is within the standard deviation. To verify a clear shift of the VB(M) closer to the Fermi level for sample set B, as expected according to literature [25], more VB measurements are necessary.

Still, the here presented VBM values are closer to the Fermi level (see Figure 6.6) than those presented in [25] with 1.7 eV and 1.6 eV for CsSnBr₃ without and with SnF₂, respectively, which may be related to the different techniques used to measure the VB and determination of VBM. In Ref. [25], Ultraviolet Photoemission spectroscopy (UPS) measurements were used to determine the VBM positions. UPS is more surface sensitive than HAXPES, which means that the literature results reflect the VB(M) of the surface states (including possible surface adsorbates or in this particular case more "oxidation" as compared to the bulk). Considering this and assuming that the CsSnBr₃ perovskite is a n-doped semiconductor, the bands seem to bend down towards the surface region leading to an accumulation of electrons at the surface of the perovskite [57]. This effect might result in an enhanced recombination of the electrons with the holes at the HTM/perovskite interface.

Although an improvement in efficiency can be seen for the absorbers treated with SnF₂, as discussed in [25]; the shift in the VBM (considering also the standard deviation) induced by the addition of SnF₂ and its effect on the band alignment of the solar cells might be minimal

sample set A and B normalized to the background. The TiO₂ VB spectrum was scaled to the O 2p DOS feature at 8 eV of the perovskite spectra.

6.1 Results and Discussion

or null. Nevertheless in the following the band alignment of both sample set A and B, under consideration of the small shift in VBM, will be discussed in order to try to clarify the origin of the improved performance of the absorber with SnF_2 .

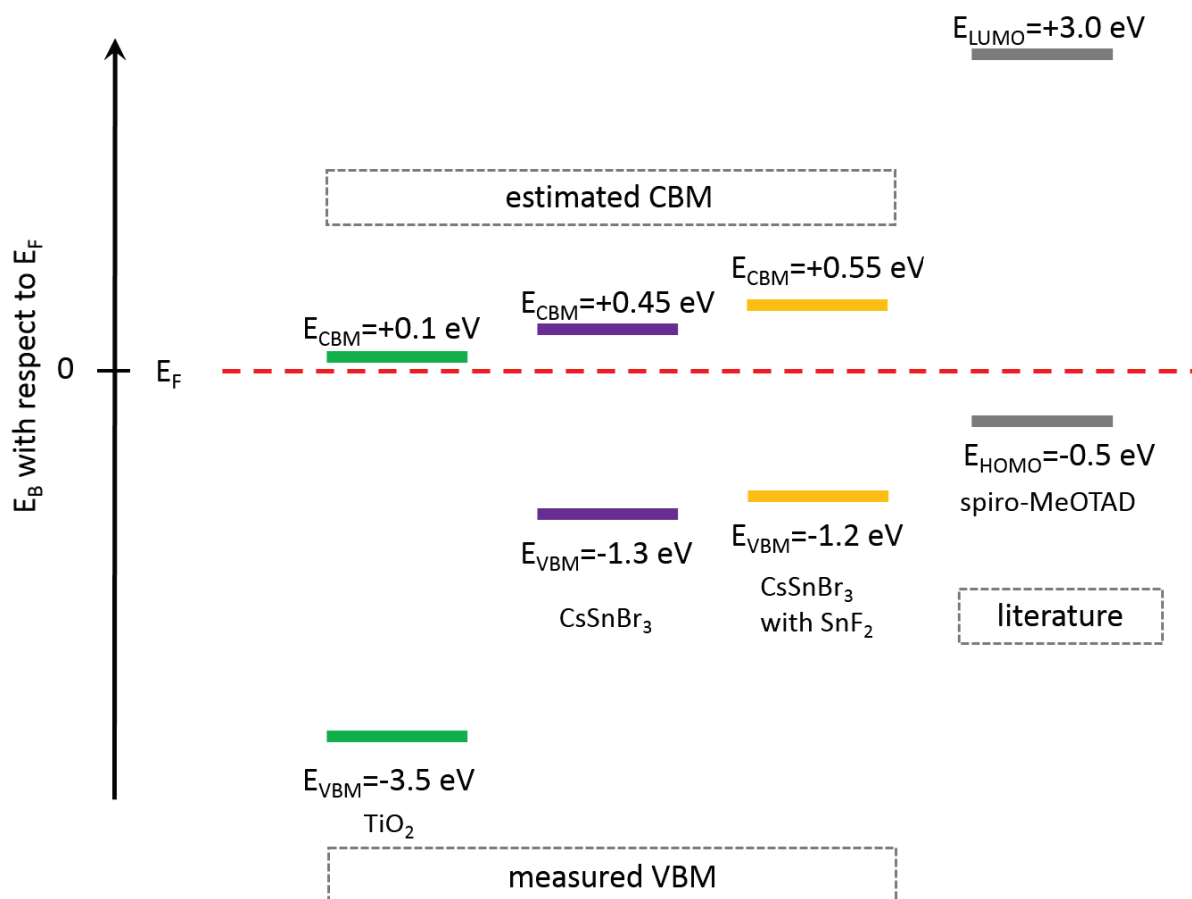


Figure 6.6.: Energy positions of the VBM (from HAXPES experiments except for spiro-MeOTAD) and CBM for c-TiO_2 , CsSnBr_3 without and with SnF_2 relative to the Fermi level. CBM values were calculated from band gap, given in Ref. [25, 68, 116, 120]. Note that the determined VBM of TiO_2 from the measurements has an estimated error of 0.1 eV. The averaged VBM of CsSnBr_3 without and with SnF_2 have an error of 0.2 eV.

Figure 6.6 shows the estimated band alignment of TiO_2 and CsSnBr_3 with (and without) SnF_2 , as well as spiro-MeOTAD with respect to the Fermi level. To align the HOMO level of spiro-MeOTAD with respect to the Fermi level, the ionisation energy (IE) of the spiro-MeOTAD from Ref. [68] and the work function of CsSnBr_3 with SnF_2 from Ref. [25] were used. The CBM and LUMO of the perovskite and spiro-MeOTAD were calculated from the band gap in [25, 68], assuming that SnF_2 does not influence the band gap of CsSnBr_3 . Since TiO_2 has a higher

VBM than expected a band gap of 3.6 eV is assumed, which is in the possible energy range for larger grain sizes of TiO₂ [116, 120]. The CBO between TiO₂ and CsSnBr₃ is in average -0.35 eV (for sample A) and -0.45 eV (for sample B) in zero order approximation (neglecting iibb), leading to "cliff"-like configurations for both sample sets allowing an unhindered electron movement from the perovskite CB to the TiO₂ CB. However, a "cliff"-like band alignment of the CB leads to a decreased hole barrier at the interface between the absorber and ETM, leading to an increased recombination of electrons with holes at the interface reducing the resulting open circuit voltage. Therefore the slightly higher CBO for CsSnBr₃ with SnF₂ might increase the electron injection into the transporting material, but also the recombination at the interface. The VBO of CsSnBr₃ VBM and spiro-MeOTAD HOMO level is in average -0.8 eV (for sample A) and -0.7 eV (for sample B) leading in both cases to a "spike"-like band alignment in zero order approximation as well. Limiting the V_{OC} of the respective solar cell due to the huge "spike"-like VBO. Adding SnF₂ slightly reduces the VBO, which might increase the V_{OC} , but on the other hand the resulting higher CBO with SnF₂ might lead to an increased recombination at the interface, canceling out the beneficial effect obtained by the shift in VBM. Therefore the improved efficiency may result mainly from the decrease in Sn vacancies (Sn⁴⁺), which might lead to a reduced recombination and thus increase of the V_{OC} . Further shows the band alignment that spiro-MeOTAD is not suited as an HTM for the CsSnBr₃ sample.

6.1.3. Summary

HAXPES investigations of wet-chemical deposited CsSnBr₃ without and with SnF₂ on c-TiO₂/FTO/glass were performed to study the influence of SnF₂, as an oxidation inhibitor of Sn, on the chemical and electronic properties of the absorber. The result shows that SnF₂ indeed limits, but is not able to completely suppress, the oxidation of Sn²⁺ to Sn⁴⁺. Furthermore SnF₂ increases the coverage of the substrate and changes the composition, leading to a decrease of Br and Cs relative to Sn in the sample.

Additionally affects the reduced oxidation of Sn also the VB states. Part of the unoccupied Sn 5s states that are empty in the CB for Sn⁴⁺ are filled for Sn²⁺ and form part of the VB, leading to a small shift of the VBM towards the Fermi level.

7. Conclusion and Outlook

For hybrid organometallic perovskites ($\text{CH}_3\text{NH}_3\text{PbI}_{(3-x)}\text{Cl}_x$) the surface of a wet-chemically deposited $\text{CH}_3\text{NH}_3\text{PbI}_{(3-x)}\text{Cl}_x$ layer on c- TiO_2 /FTO/glass was studied with lateral resolution by combining complementary SEM, EDX, PEEM-XPS and PEEM-XAS, revealing an inhomogeneous morphology of the surface, with an incomplete coverage of the substrate by the perovskite, in which holes (*exposed TiO_2 sample area*) reach to the TiO_2 . Further, spatially resolved XPS revealed the presence of Pb and I in the holes and metallic Pb (Pb^0) and enhanced I oxidation close to the perovskite/c- TiO_2 interface. The presence of Pb and I in the holes indicates remnants of the perovskite precursor solution from the preparation step and/or the formation of a Pb-I(-O) containing seed/interface layer on the substrate. The changes in chemical composition depend on the degree of coverage and are also reflected in the electronic structure.

Relative to the *exposed TiO_2 sample area* (pin-hole) the VBM of the perovskite layer is shifted closer to the Fermi level by (-1.7 ± 0.2) eV. Together with the CBM values taken from literature, the energy level alignment is sketched, and shows that the spiro-MeOTAD(HTM)/perovskite and perovskite/c- TiO_2 (ETM) junctions are nearly ideal charge selective contacts for holes and electrons, respectively. For the pin-hole area, where the HTM and ETM could come in direct contact due to the absent absorber, the estimated energy level positions imply sufficiently high energetic barriers to suppress high rate charge carrier recombination and prevent the short circuiting of the solar cell device, explaining why these devices still function despite high pin-hole densities.

(AP)-HAXPES measurements were performed on 60 and 300 nm thick $\text{CH}_3\text{NH}_3\text{PbI}_{(3-x)}\text{Cl}_x$ perovskites on c- TiO_2 FTO/glass to study in-situ the impact of "vacuum", water and illumination (UV light) on the absorber, revealing different degradation mechanism depending on the environment and the thickness of the sample. For the 60 nm perovskite sample, without defined illumination, the formation of metallic Pb through radiolysis was observed in water vapor.

For the 300 nm sample in high vacuum in the dark, no decrease of the I, Pb^0 , Pb perovskite

Conclusion and Outlook

(PbI₂) and MAI-related component with increasing C=O contribution can be observed, nor can the expected species HI in the I 3d spectra, indicating that 300 nm perovskite are stable in high vacuum in the dark.

For the 300 nm sample in water vapor (high water pressure at 15 Torr) in the dark, decreases of the I, Pb⁰ and MAI-related components can be observed over time and with increasing adsorbed molecular water contribution, whereas the Pb perovskite/PbI₂ contribution stays constant. These findings agree with the proposed degradation mechanism, stating that the perovskite dissolves into its organic and inorganic components, according to Ref. [16,47].

The (AP)-HAXPES measurement of the 300 nm sample at low water pressure (in high vacuum with residual water) under illumination shows a different behavior than the previous exposure experiments. In addition to water adsorption on the sample, a decrease of the I, Pb perovskite and MAI-related components can be observed. In contrast, the Pb⁰ component increases significantly under illumination, confirming the proposed [16, 19, 47, 48] degradation, where the perovskite is dissolved into its organic and inorganic component (PbI₂), with subsequent degradation of PbI₂ to Pb⁰ under illumination. Under illumination, a shift due to SPV in E_B was also observed with the direction of the shift depending on the surface conditions, i.e., wet or dry (dipoles).

The 300 nm sample in water vapor (high vapor pressure at 15 Torr) under illumination does not show unambiguous evidence for a specific degradation mechanism under illumination, such as those according to Ref. [16, 19, 47, 48]. However, similar behavior (i.e., degradation) as for the sample in the dark in water vapor has been observed after the light has been turned off.

Moreover, the 300 nm sample was more stable under x-rays (no Pb⁰ formation) in water vapor (in the dark) than the 60 nm sample, which could be partly ascribed to the difference in thickness and morphology.

For studying the impact of SnF₂ as an oxidation inhibitor on the chemical and electronic structure of purely inorganic wet-chemically deposited CsSnBr₃ absorbers on c-TiO₂/FTO/glass, HAXPES and lab-based XPS measurements have been performed and revealed that CsSnBr₃ samples with SnF₂ have a better coverage of the substrate, lower Sn⁴⁺ contribution to the Sn 4d, as well as the reduced contribution of oxidation-related species of Br and Cs compared to the CsSnBr₃ samples without SnF₂. These observations confirm the oxidation inhibiting properties of SnF₂. Furthermore, a change in composition of the absorber is observed (i.e., Cs/Sn and Br/Sn ratios decrease), as expected, when SnF₂ is added to the precursor solution. However, the experimentally determined Cs/Sn, Br/Sn and F/Sn ratios are much lower than the expected

elemental ratios. Further, there is an influence of the oxidation of Sn on the electronic structure, i.e. VB states, of the CsSnBr₃ absorber observed: For reduced oxidation of Sn, an increase of Sn 5s-dominated DOS is observed, which is related to redistribution of the unoccupied Sn 5s states in the CB for Sn⁴⁺ to the filled VB for Sn²⁺.

Based on the findings of the CH₃NH₃PbI_(3-x)Cl_x absorbers, the next step would be to complete the degradation mechanism picture, by performing further (AP)-HAXPES measurements of the 300 nm sample in UHV under illumination (i.e. in a "dry" environment), while monitoring the core levels of the perovskite, to unambiguously verify that for the degradation under illumination both light and water are necessary, since no degradation in high vacuum in the dark was observed. Alternatively, pin-hole free CH₃NH₃PbI_(3-x)Cl_x absorber could be studied with (AP)-HAXPES under different conditions, by monitoring the perovskite related core levels, to decouple the impact of the morphology of the absorber from the degradation mechanism. Ultimately, the organic cation methylammonium could be replaced by more stable organic cations e.g., formamidinium, or by inorganic cations e.g., Cs to perform, first, laterally resolved investigation by PEEM to study morphology and chemical composition and then further (AP)-HAXPES to study the impact of water and light on these absorbers to confirm their enhanced stability. Inorganic, Cs-based perovskite have been proposed to be more stable in humid environments (and UV light) making this absorber the next candidate for future (AP)-HAXPES measurement. The increase in long-term stability is therefore compelling.

For the Pb-free inorganic perovskite samples, the current results shows that oxidation is inhibited by SnF₂ in wet-chemically deposited CsSnBr₃ samples, but it is not suppressed completely. The next step would be, as alternative for adding SnF₂ to the precursor solution, a change of deposition environment/technique to minimize the risk of Sn oxidation. Sn is more likely to oxidize when CsSnX₃ is prepared wet-chemically (e.g., via spin-coating in a glovebox) than if it is prepared by thermal evaporation under vacuum conditions. For the latter, depositing the absorber in ultra-high vacuum (UHV) would allow preparation of films without Sn oxidation. The first thermal deposition test runs of CsSnCl₃ on Mo/glass in UHV have been performed and the chemical structure was studied using HAXPES, hinting that Sn is already in a nearly pure Sn²⁺ state. The resulting chemical composition was non-ideal (small Cs/Sn and Cl/Sn ratios) requiring further deposition optimization of the material to achieve the required stoichiometry. Moreover, with an optimized in-UHV deposited CsSnCl₃ sample, additional HAXPES mea-

Conclusion and Outlook

measurements should be performed to test for reproducibility and to confirm in-UHV deposition as a means of preparing samples with reduced or no oxidation of Sn. A SnF_2 treatment of the CsSnCl_3 absorber should be considered, to study with HAXPES the impact of SnF_2 on the chemical composition and electronic structure, similar to wet-chemically deposited CsSnBr_3 . Ideally, the in-UHV prepared CsSnCl_3 sample would be compared to a wet-chemically deposited CsSnCl_3 sample with and without SnF_2 , resulting in better insight into the impact of the preparation route on the material properties and composition. The prevention of oxidation of Sn is critical to the functioning of the resulting solar cell devices.

Perovskite-based solar cells have so far demonstrated rapid growth and remarkable achievements in performance. As their physical and electronic properties are studied further, and their limiting factors are identified and overcome, they promise to contribute to future energy needs.

A. Appendix A

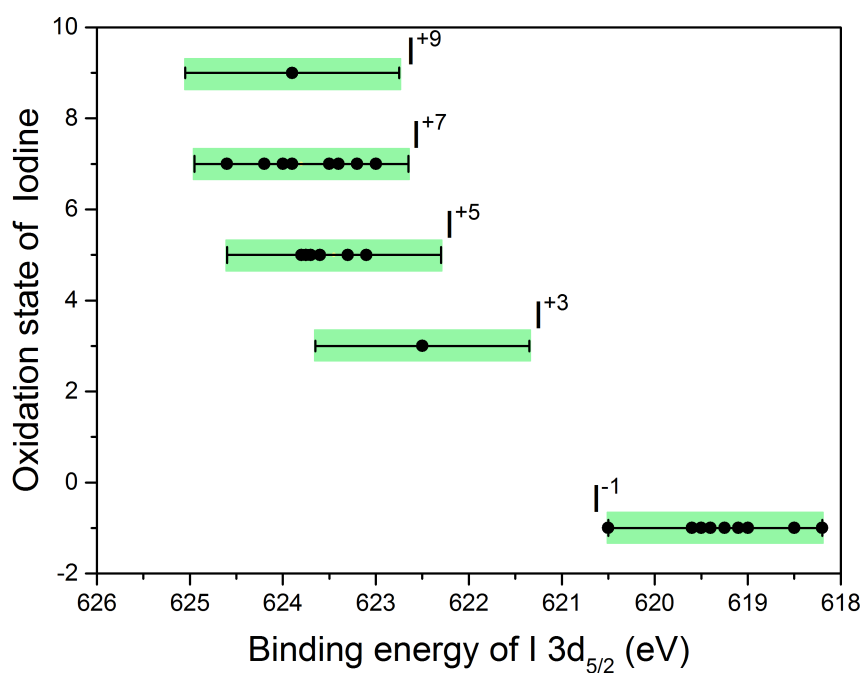


Figure A.1.: Oxidation states of I plotted over E_B of I $3d_{5/2}$ for different iodine compounds from literature [121–125]. Adapted from [75].

For the identification of the second iodine species in the I 4d XPS spectra, denoted as I 4d (II) in chapter 4, reference energies from literature for the more prominent I 3d photoemission line were examined, under the assumption that the separation between I 3d and I 4d lines will not vary significantly between compounds. For iodine, oxidation states of -1, +1, +3, +5 or +7 are possible.

Figure A.1 shows a general shift to higher binding energies as the oxidation state increases. Error bars and the corresponding light green boxes were defined by the range of possible BEs for I^{-1} , which has the most data points and is transferred to other oxidation states with less data

Appendix A

points. If the separation between I 3d and I 4d lines for oxidation states is constant, then the E_B regions defined in Figure A.1 can be translated to the energy scale of the I 4d spectra shown in Figure A.2. The light green boxes in Figure A.2 represent the relevant E_B regions for the purple I $4d_{5/2}$ peak, suggesting the presence of an iodite I^{+3} ($\rightarrow IO_2^-$) as a second species.

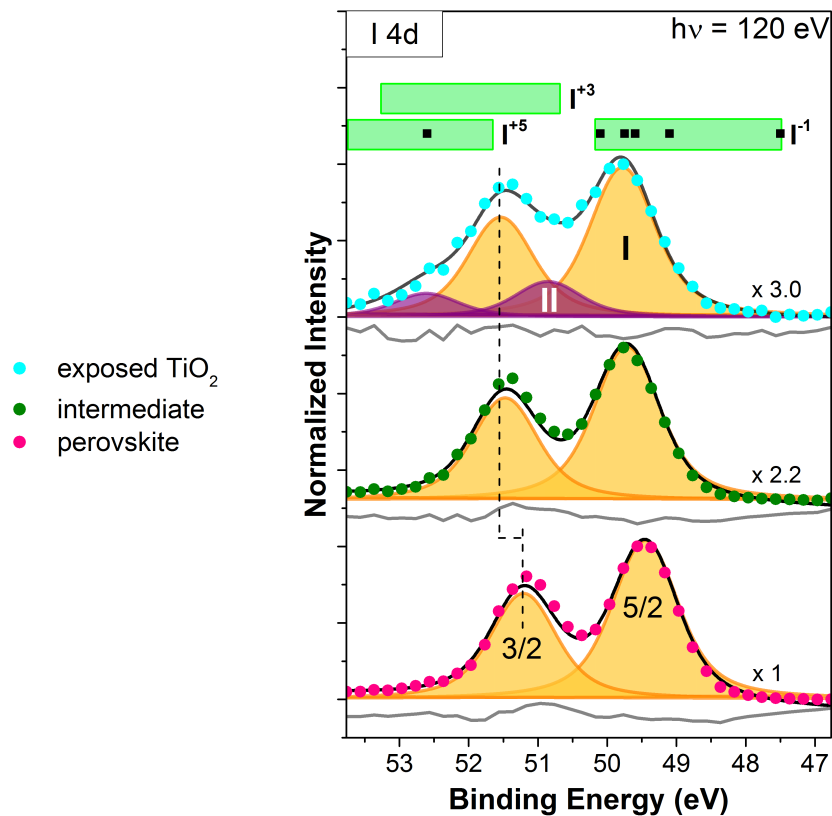


Figure A.2.: PEEM-XPS I 4d detail spectra recorded in different areas of interest including I $4d_{5/2}$ E_B values from literature [121–125] for different iodine compounds (black squares) and light green boxes transferred from the oxidation state plot in Figure A.1. Adapted from [75].

B. Appendix B

B.1. 60 nm Perovskite

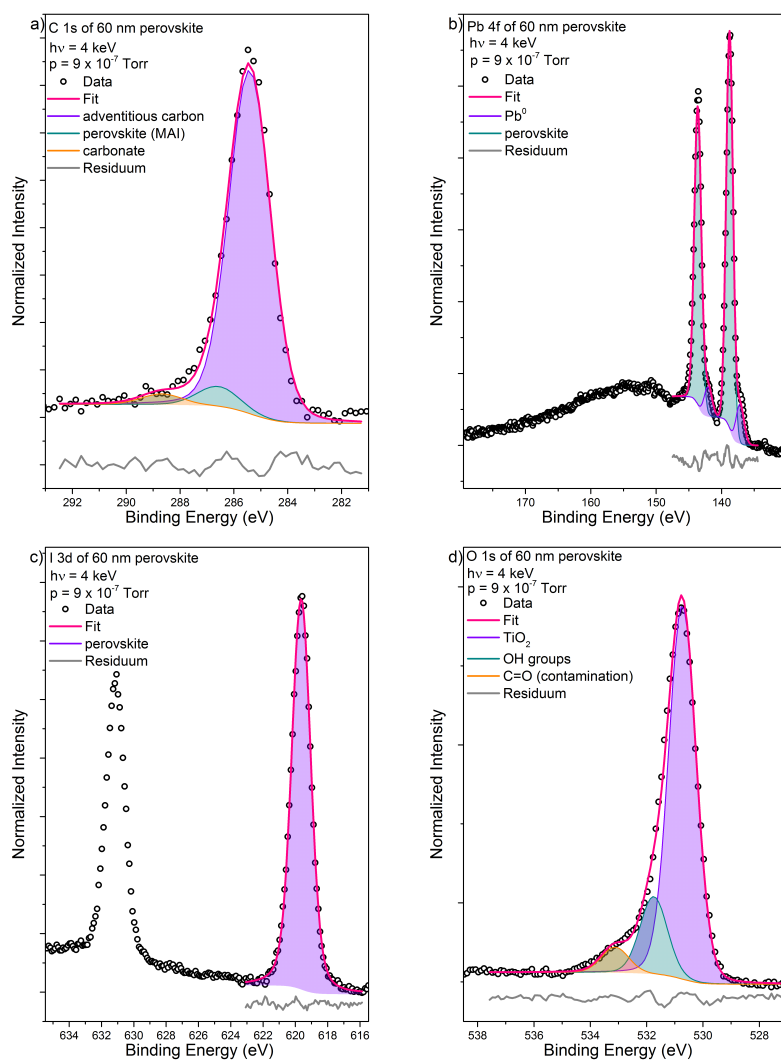


Figure B.1.: XPS detailed spectra (including fit analysis) of a) C 1s, b) Pb 4f, c) I 3d and d) O 1s of 60 nm perovskite measured in UHV (first half of the sample).

Appendix B

Figures B.1(a) - B.1(d) shows the representative core levels of the perovskite sample measured in UHV. From the fits the following E_B were obtained for C 1s $C_A = (285.4 \pm 0.1)$ eV, $C_B = (286.6 \pm 0.1)$ eV and $C_C = (288.7 \pm 0.1)$ eV which can be ascribed to adventitious carbon, MAI and carbonates respectively [88, 102]. For Pb 4f and I 3d the E_B for $Pb_A = (137.0 \pm 0.1)$ eV, $Pb_B = (138.75 \pm 0.10)$ eV and $I_A = (619.6 \pm 0.1)$ eV can be ascribed to Pb^0 , Pb and I in perovskite environment, respectively [79, 84, 102]. For O 1s the E_B are $O_A = (530.7 \pm 0.1)$ eV, $O_B = (531.75 \pm 0.10)$ eV and $O_C = (533.1 \pm 0.1)$ eV and can be attributed to O in TiO_2 , OH groups and to C=O bonds [84, 100].

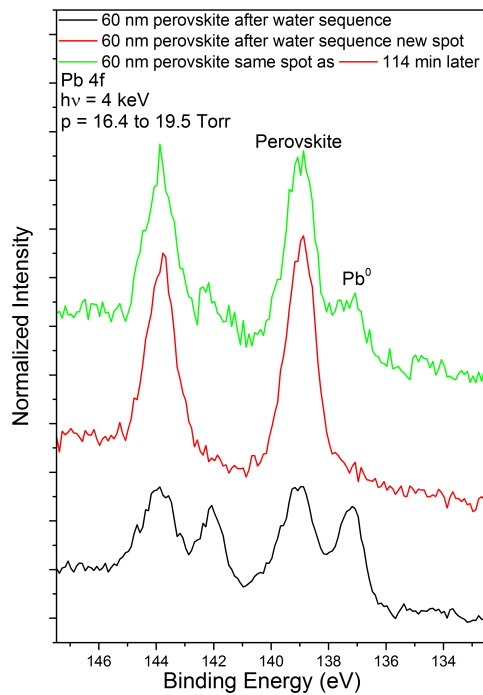


Figure B.2.: Pb 4f spectra of 60 nm perovskite measured after the sequence in water vapor (first half of the sample). Shown with an offset for clarity.

Figure B.3 shows the Pb 4f spectra and fit results of the repeated measurements with a fresh sample (second half). From the fits an averaged E_B of $Pb_A = (136.9 \pm 0.1)$ eV and $Pb_B = (138.7 \pm 0.1)$ eV can be attributed to metallic lead (Pb^0) and Pb in a perovskite environment [79, 84, 102].

B.1 60 nm Perovskite

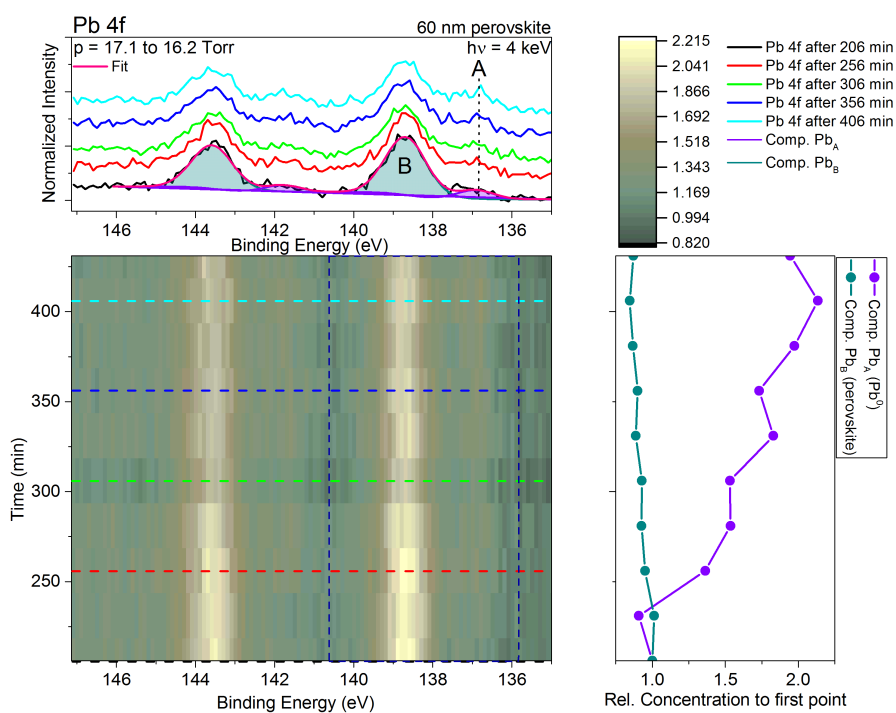


Figure B.3.: Pb 4f spectra and fit results of 60 nm sample over time in water vapor for the repeated measurement. Left bottom panel shows the measured Pb 4f as a 2D plot and representative selected spectra are shown in the left top panel as a 1D plot including the species from the fits labeled as A and B. The right panel shows the relative concentration of the two species determined from the fits divided by the relative concentration of the first spectrum of this sequence. The dark blue dashed line in the 2D plots indicates the fit range of the species displayed on the right.

Appendix B

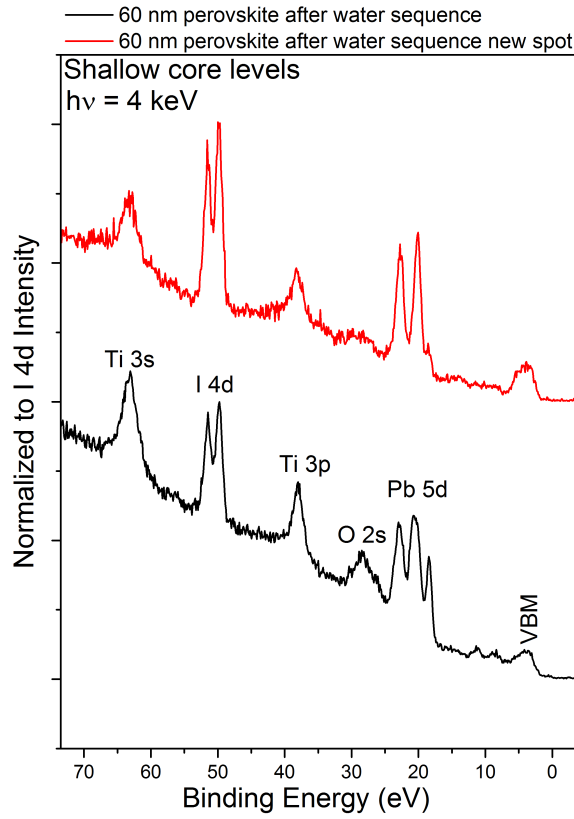


Figure B.4.: Shallow core levels of 60 nm sample measured in water vapor after the sequence for the old and new spot normalized to I 4d intensity (first half of the sample). Shown with an offset for clarity.

Figure B.5 and B.6 show the O 1s and I 3d spectra, respectively, measured during the sequence in water vapor for the repeated measurements of the second half of the sample. From the fits the following averaged E_B for O 1s of $O_A = (530.6 \pm 0.1) \text{ eV}$ can be attributed to O in TiO_2 , O_B with $(531.6 \pm 0.1) \text{ eV}$ to OH groups, O_C with $(533.4 \pm 0.1) \text{ eV}$ to molecular water and O_D with $(535.9 \pm 0.1) \text{ eV}$ to gas phase water [84, 100]. For I 3d an averaged E_B of $I_A = (619.5 \pm 0.1) \text{ eV}$ can be attributed to I in a perovskite environment [79, 84, 102].

B.1 60 nm Perovskite

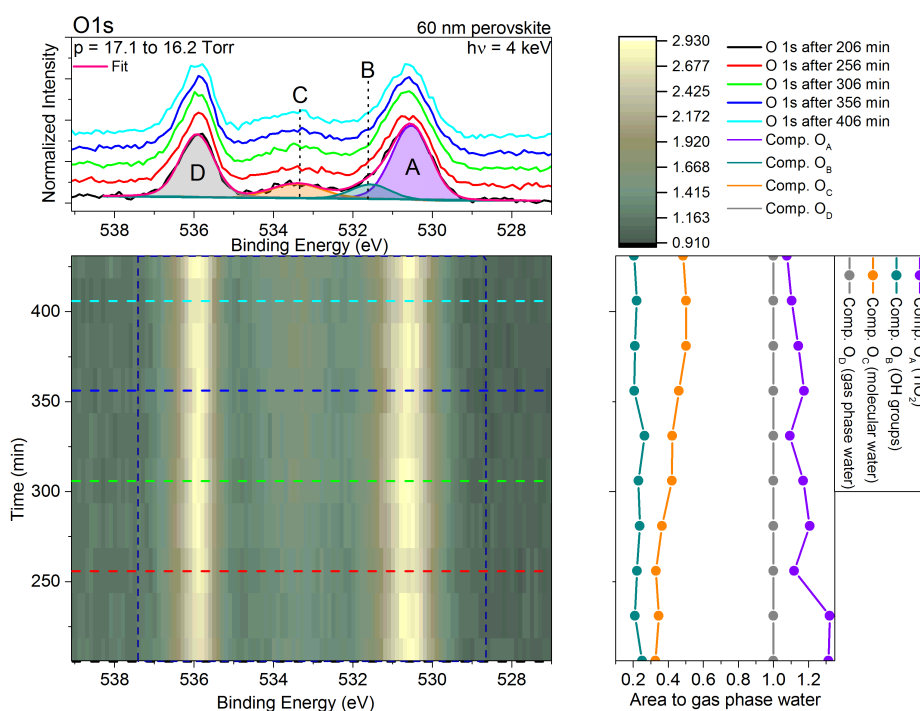


Figure B.5.: O 1s spectra and fit results of 60 nm sample over time in water vapor for the repeated measurement. Left bottom panel shows the measured O 1s as a 2D plot and representative selected spectra are shown in the left top panel as a 1D plot including the species from the fits labeled as A, B, C and D. The right panel shows the area of each of the four species determined from the fits divided by the area of the gas phase water contribution. The dark blue dashed line in the 2D plots indicates the fit range of the species displayed on the right.

Appendix B

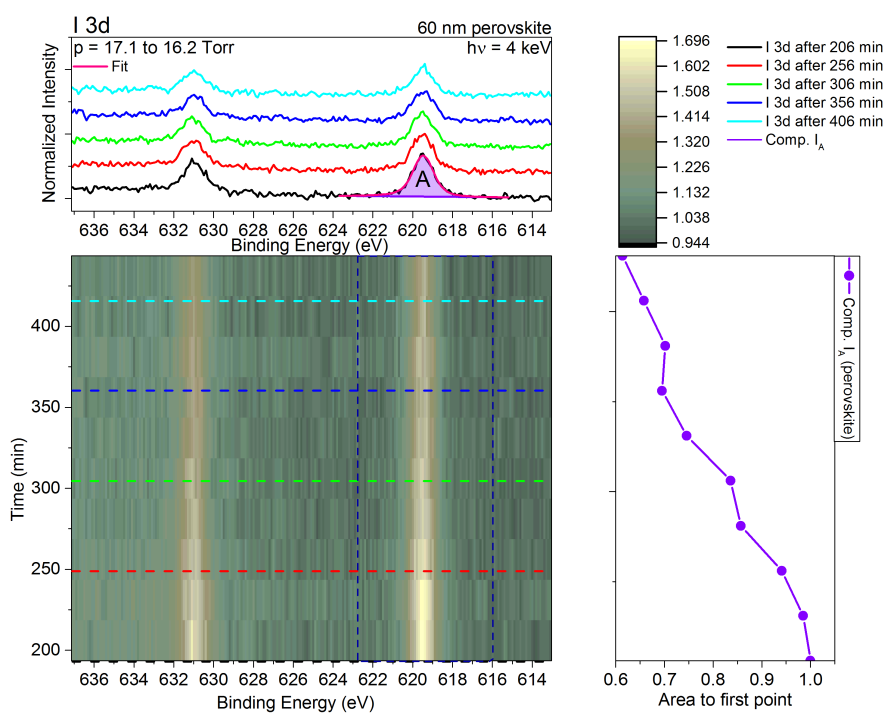


Figure B.6.: I 3d spectra and fit results of 60 nm sample over time in water vapor for the repeated measurement. Left bottom panel shows the measured I 3d as a 2D plot and representative selected spectra are shown in the left top panel as a 1D plot including the species from the fits labeled as A. The right panel shows the area ratio of the species determined from the fits divided by the area of the first spectrum of this sequence. The dark blue dashed line in the 2D plots indicates the fit range of the species displayed on the right.

B.1 60 nm Perovskite

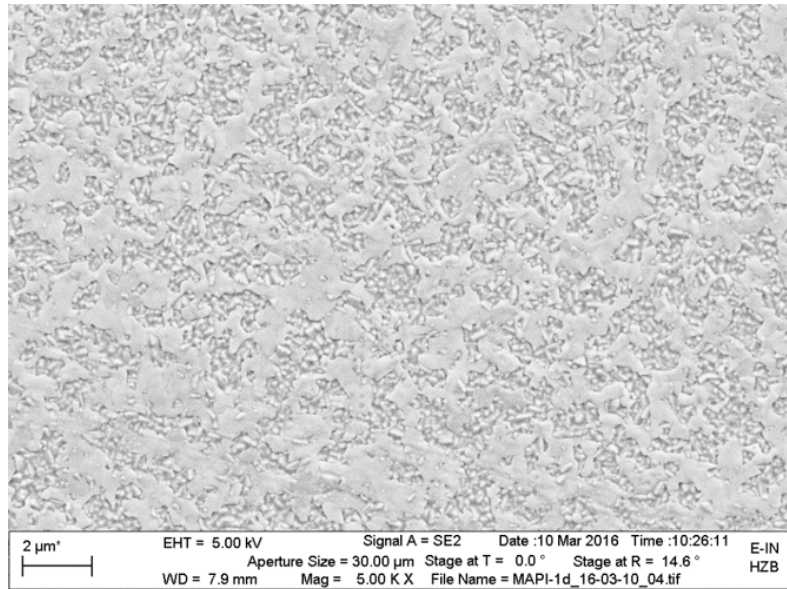


Figure B.7.: SEM image of the surface of a 60 nm thick $\text{CH}_3\text{NH}_3\text{PbI}_{(3-x)}\text{Cl}_x$ layer on $c\text{-TiO}_2$.

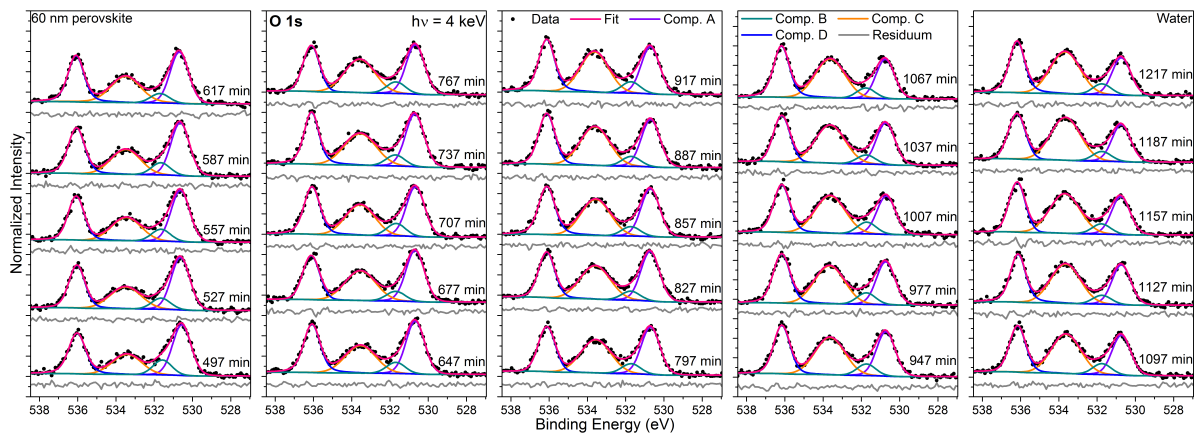


Figure B.8.: O 1s fits of the 60 nm perovskite sample in water vapor.

Appendix B

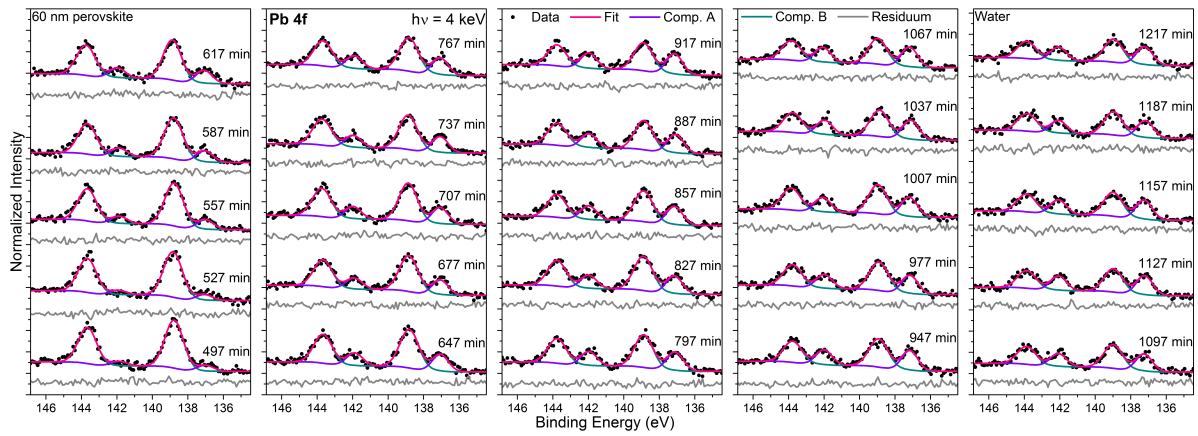


Figure B.9.: Pb 4f fits of the 60 nm perovskite sample in water vapor.

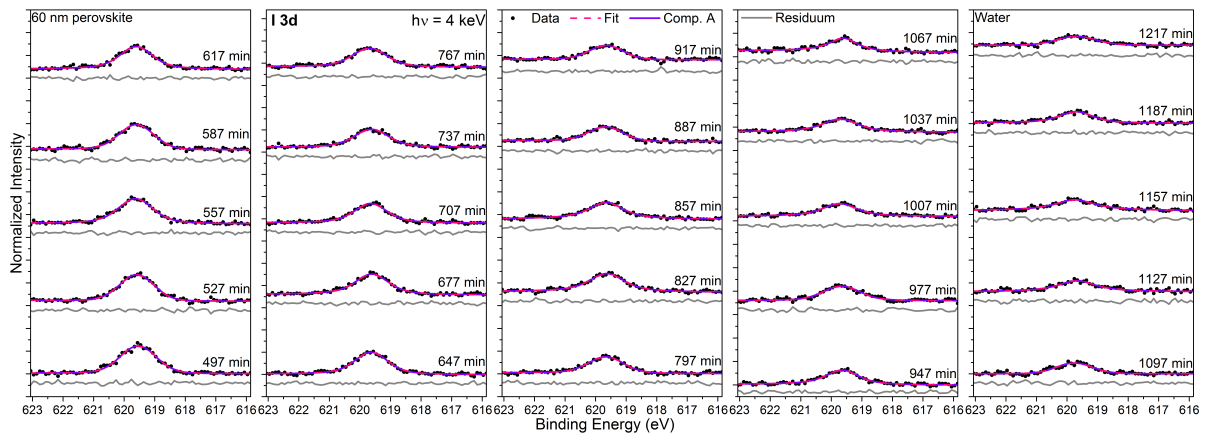


Figure B.10.: I 3d fits of the 60 nm perovskite sample in water vapor.

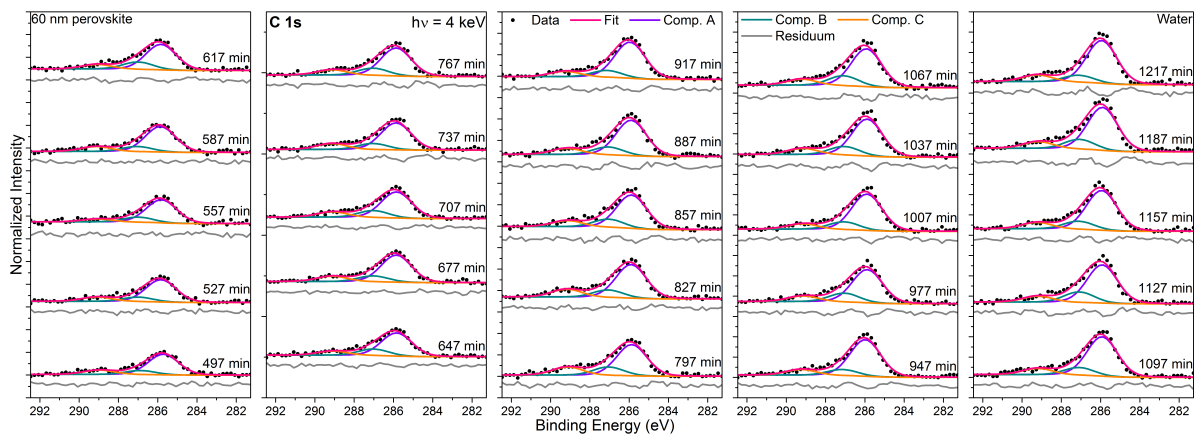


Figure B.11.: C 1s fits of the 60 nm perovskite sample in water vapor.

B.1 60 nm Perovskite

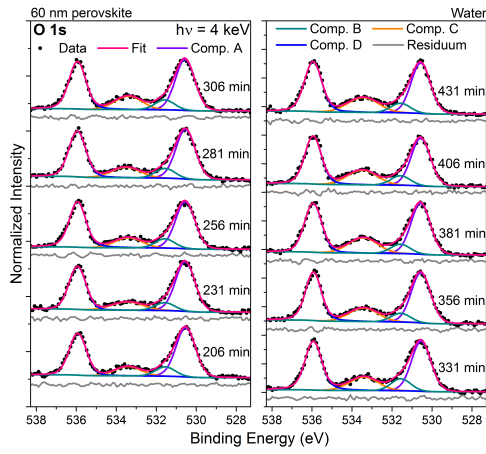


Figure B.12.: O 1s fits of the remeasured 60 nm perovskite sample in water vapor (second half).

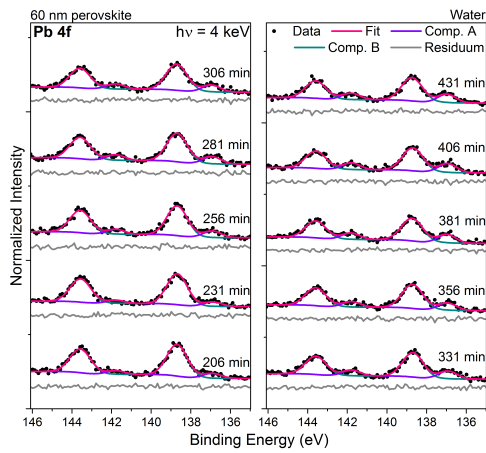


Figure B.13.: Pb 4f fits of the remeasured 60 nm perovskite sample in water vapor (second half).

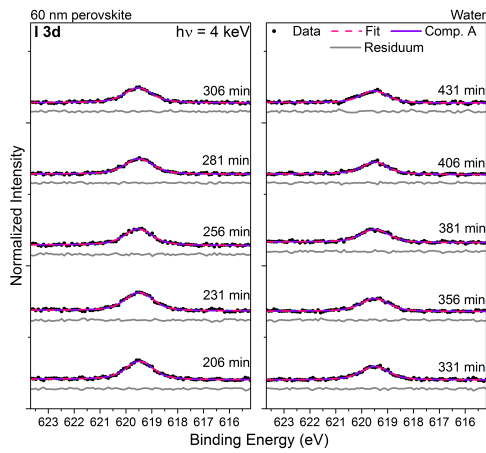


Figure B.14.: I 3d fits of the remeasured 60 nm perovskite sample in water vapor (second half).

B.2. 300 nm Perovskite

B.2.1. 300 nm Perovskite in the Dark

Figure B.15 shows the two Pb 4f spectra measured after the sequence in the dark at 15 Torr with more sweeps for a better resolution. The royal blue spectrum was measured at a new sample spot to check for beam damage effects.

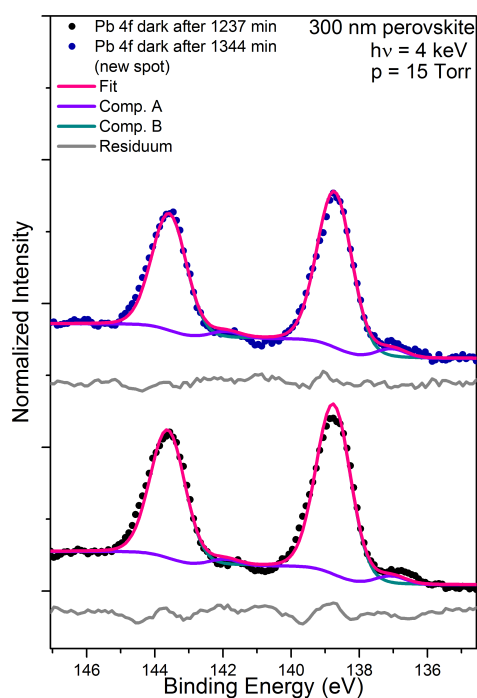


Figure B.15.: Pb 4f spectra (including fit analysis) of 300 nm sample measured after the sequence in the dark and in water vapor with an offset for clarity.

Figure B.16 shows the relative concentration of the two Pb species, for high vacuum and in water vapor, determined from the fit. Component Pb_A correspond to Pb^0 and Pb_B to Pb in the perovskite. The last two data points in the blue shaded region are not connected and represent the fit results from the two Pb 4f spectra measured after the sequence (see Figure B.15), where the slight decrease in the relative concentration of perovskite (Pb_B) for the last data point is not necessarily due to the new spot not being affected by the x-ray beam (beam damage), it might simply reflect a spot with a lower Pb perovskite content compared to the old spot.

B.2 300 nm Perovskite

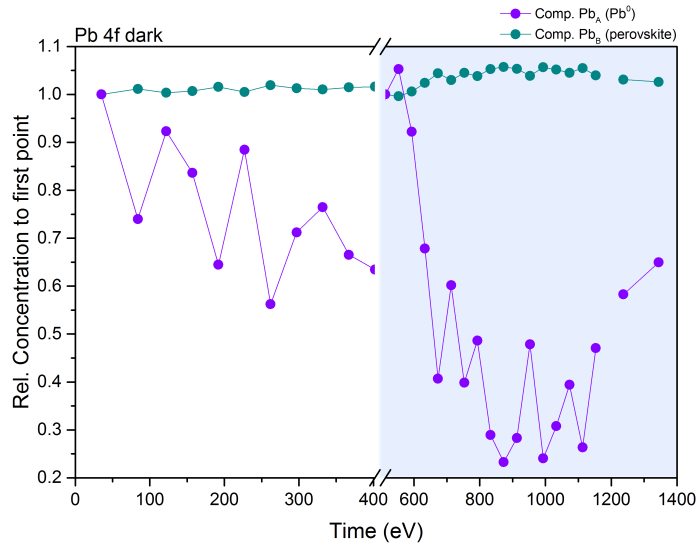


Figure B.16.: Shows the relative concentration of Pb 4f species in the dark as an overview for high vacuum and in water vapor (at 15 Torr) divided by the relative concentration of the first spectrum of each sequence. The blue shaded area indicates the data points from the water vapor measurements.

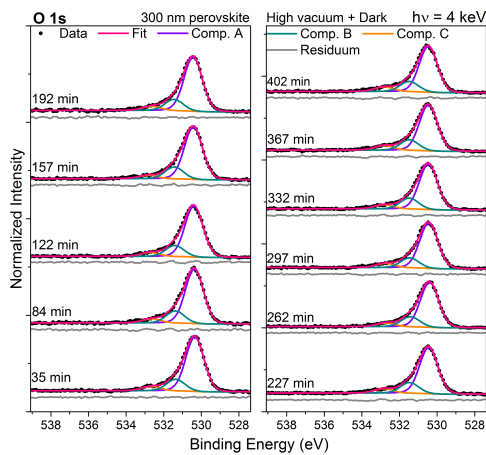


Figure B.17.: O 1s fits of 300 nm perovskite sample in high vacuum in the dark.

Appendix B

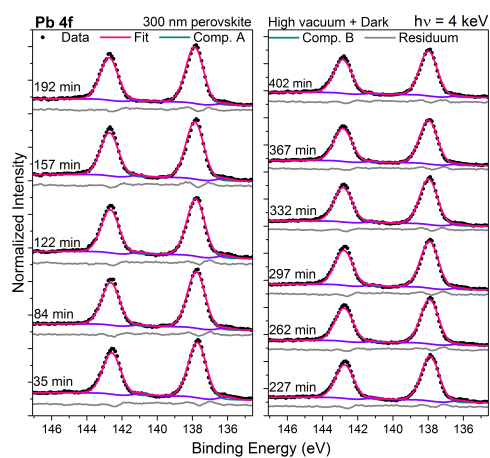


Figure B.18.: Pb 4f fits of 300 nm perovskite sample in high vacuum in the dark.

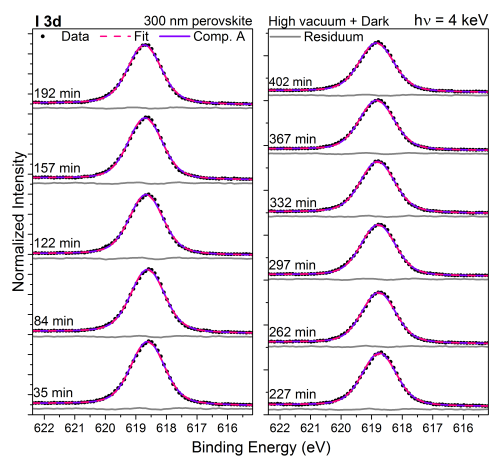


Figure B.19.: I 3d fits of 300 nm perovskite sample in high vacuum in the dark.

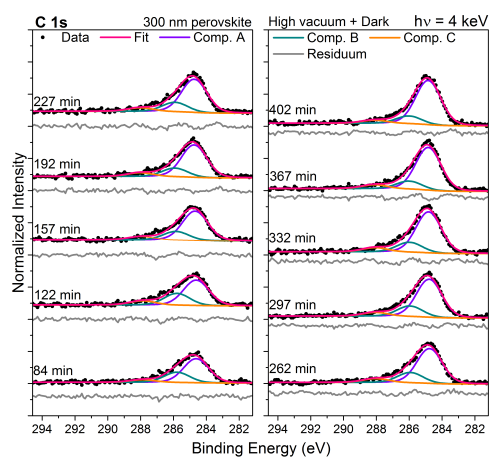


Figure B.20.: C 1s fits of 300 nm perovskite sample in high vacuum in the dark.

B.2 300 nm Perovskite

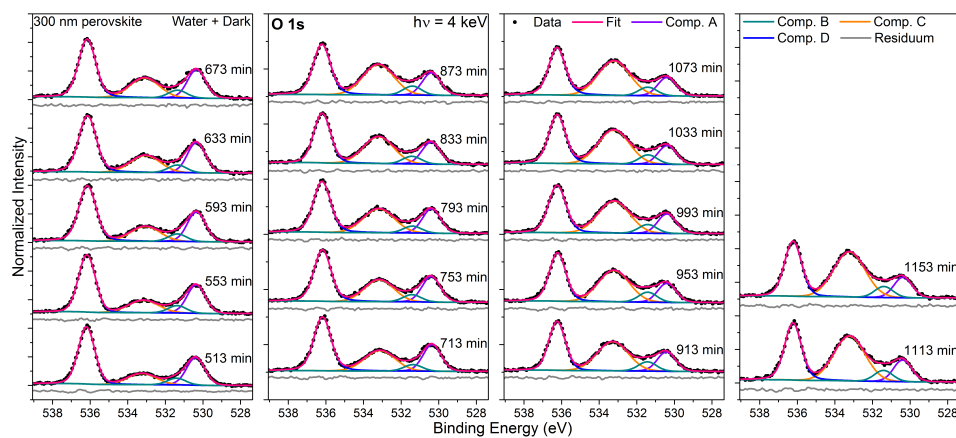


Figure B.21.: O 1s fits of 300 nm perovskite sample in water vapor in the dark.

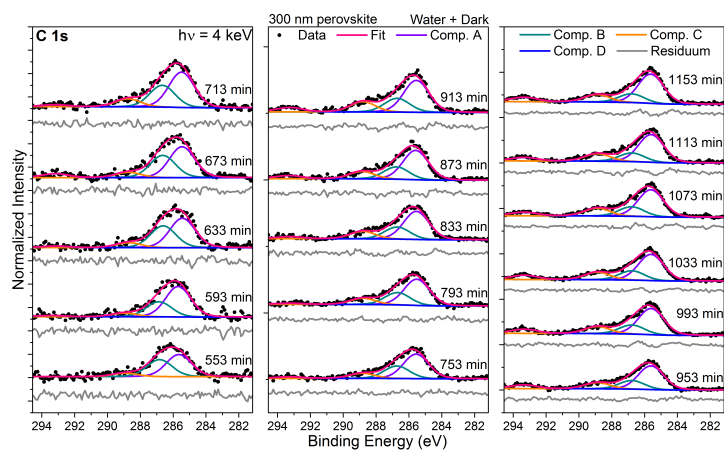


Figure B.22.: C 1s fits of 300 nm perovskite sample in water vapor in the dark.

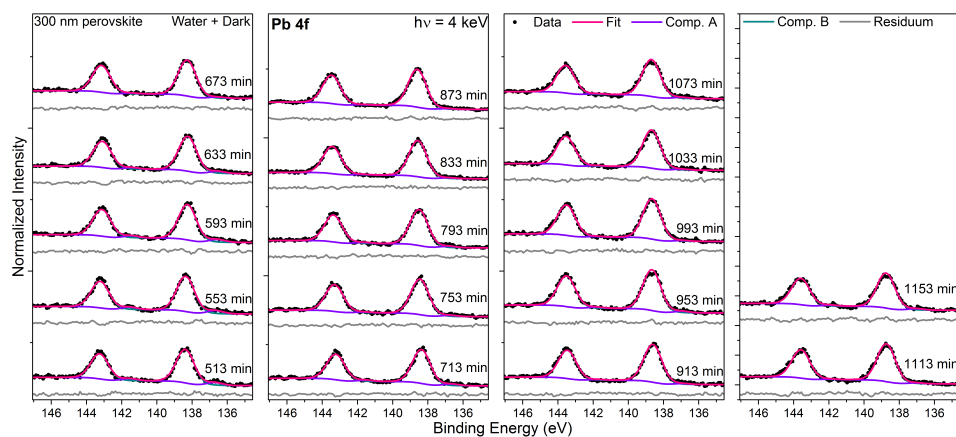


Figure B.23.: Pb 4f fits of 300 nm perovskite sample in water vapor in the dark.

Appendix B

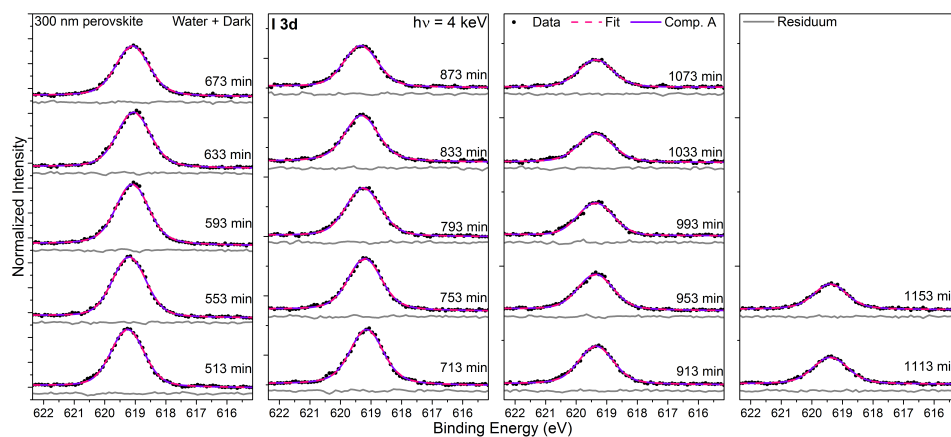


Figure B.24.: I 3d fits of 300 nm perovskite sample in water vapor in the dark.

B.2.2. 300 nm Perovskite under Illumination

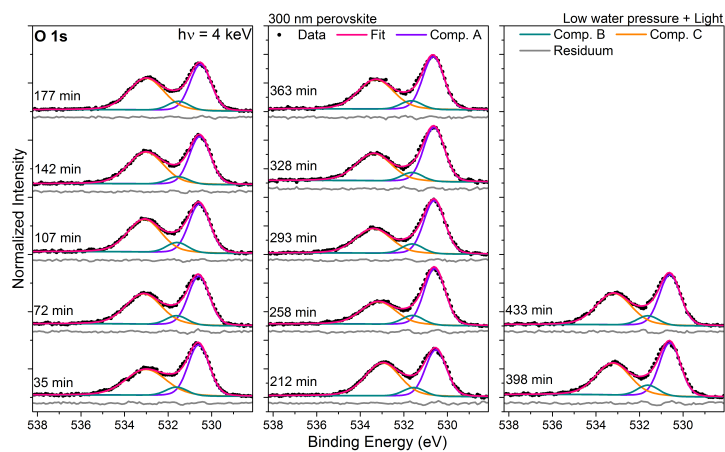


Figure B.25.: O 1s fits of 300 nm perovskite sample at low water pressure under illumination.

B.2 300 nm Perovskite

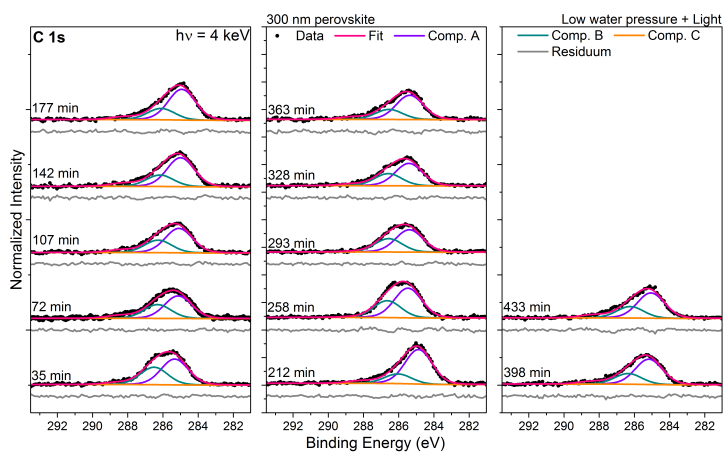


Figure B.26.: C 1s fits of 300 nm perovskite sample at low water pressure under illumination.

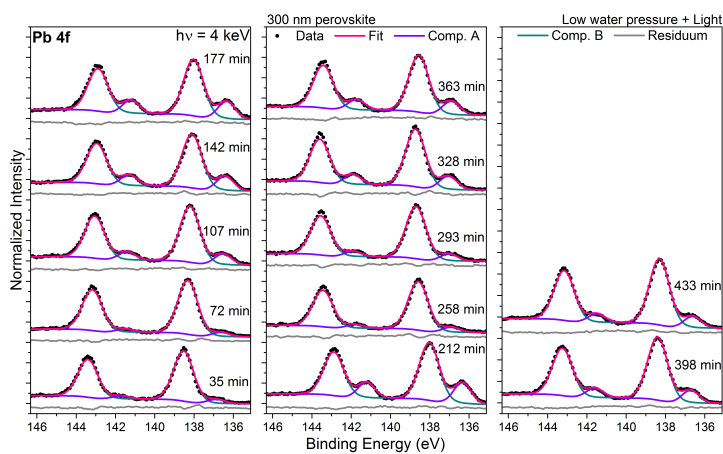


Figure B.27.: Pb 4f fits of 300 nm perovskite sample at low water pressure under illumination.

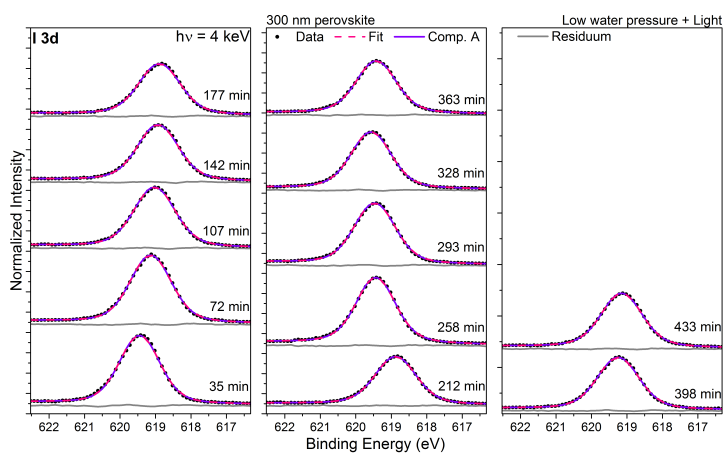


Figure B.28.: I 3d fits of 300 nm perovskite sample at low water pressure under illumination.

Perovskite in the Light and in Water Vapor

In this subsection the results of the sequence measurements taken from the perovskite sample at high water pressure (at 15 Torr) and under illumination will be presented. In order to increase the water in the chamber, after the sequence measurement at low water pressure under illumination (see subsection 5.2.3) a beaker filled with water was put into the chamber and pumped down to 15.2 Torr which further decreased to 14.6 Torr before stabilizing around 15 Torr. The timescale continues from the low water pressure measurement and the illumination of the sample started after the first scan after 537 min and was illuminated for 315 min. After that the sample was probed by x-rays for 140 min without illumination and after a total time of 997 min, the sample spot was changed. The measurement continued for 35 min more and then the solar simulator was turned on again after a total time of 1032 min for one more scan.

Figure B.29 displays the measured O 1s spectra and fit results. The peaks in the spectra shift first towards lower E_B as soon as the light is turned on, stay constant during illumination and then shift to higher E_B values as soon the light is turned off. Going to a new spot and turning the light on again leads first to a shift in E_B to lower values. The increase of E_B without light is to be expected due to the water environment and possible adsorption of molecular water on the surface, but the constant E_B during illumination may be due to a competitive process between the shift of E_B to lower values due to SPV and adsorption of water (chemical shift or dipole) to higher E_B . Similar to the O 1s in the dark four species can be identified through fitting and since the E_B shifts are small (and in the fitting error range) the following averaged E_B can be attributed to $O_A = (530.5 \pm 0.2)$ eV to O from TiO_2 , $O_B = (531.5 \pm 0.2)$ eV to OH groups, $O_C = (533.2 \pm 0.2)$ eV to molecular water and $O_D = (536.2 \pm 0.2)$ eV to gas phase water from the water vapor. The determined E_B of O 1s species in water vapor and under illumination correspond to E_B of O 1s species determined for the 300 nm samples under various conditions.

Further does the area of the gas phase water contribution O_D , in the right panel of Figure B.29, not change over time and is independent from the UV illumination (for normalization reasons). Only the molecular water component seems to increase, indicating a growth of the water film. Whereas the TiO_2 contribution decreases and the OH group contribution stays constant over time. Changing to a new spot results in a lower area ratio of molecular water and a slightly higher TiO_2 compared to the end of the measurements of the previous spot. Still, under illumination the increase of molecular water is not as strong as it was in the dark (see Figure 5.10), mainly due to the fact that for the low water pressure experiment water was already adsorbing on the sample. But the decrease of the substrate signal seems to be slightly

B.2 300 nm Perovskite

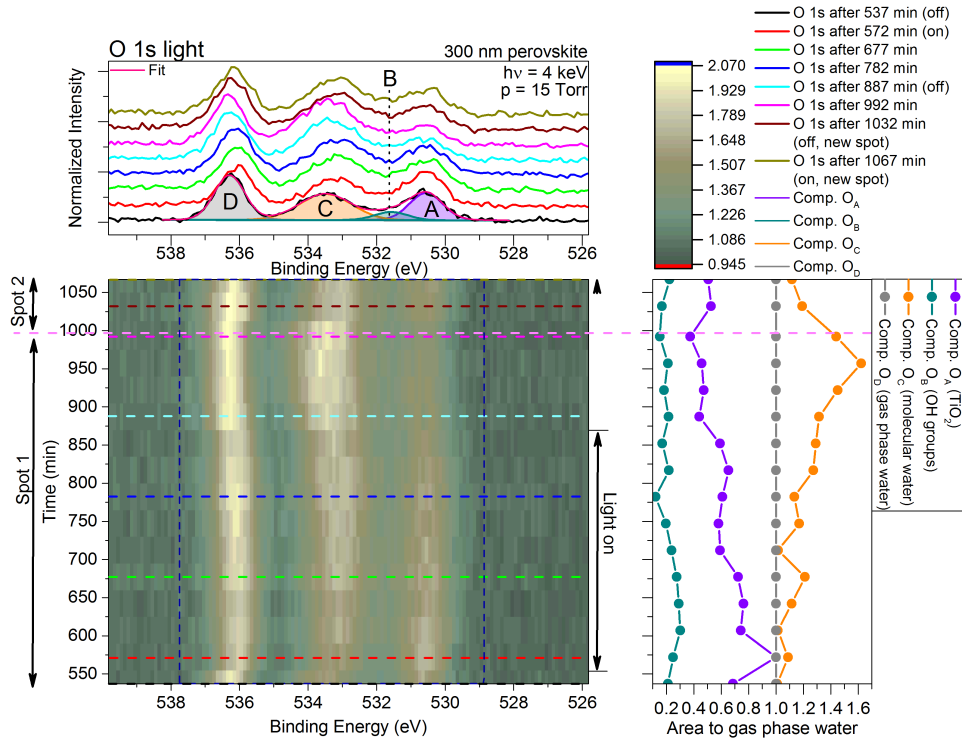


Figure B.29.: O 1s spectra and fit results of 300 nm sample over time under UV illumination at 15 Torr. Left bottom panel shows the measured O 1s as a 2D plot and representative selected spectra are shown in the left top panel as a 1D plot including the species from the fits labeled as A,B,C and D. The right panel shows the area of each of the four species determined from the fits divided by the area of the gas phase water contribution. The dark blue dashed line in the 2D plots indicates the fit range of the species displayed on the right. The light magenta dashed line shows the change to a new sample position and the arrow between the left and right panel indicates the time frame were the sample was illuminated.

enhanced, pointing towards adsorption of water on the TiO_2 .

For I 3d in Figure B.30, similar shifts in E_B over time as for O 1s in Figure B.29 can be observed, which are slightly more pronounced. Indicating further during illumination a slight shift to higher E_B which becomes stronger after the light is turned off. Since the shift in E_B for I 3d is more pronounced compared to O 1s, a E_B range for I_A from 619.0 to 619.5 eV is given, which is still within the energy range for I in a perovskite environment and corresponds to the E_B of I of the 300 nm perovskite sample in the dark in water vapor, at low water pressure under illumination and the 60 nm sample in UHV. Further shows Figure B.30 a decrease of I 3d_{5/2} intensity given by narrower appearing peaks in the 2D plot, which starts to decrease 70 min (2

Appendix B

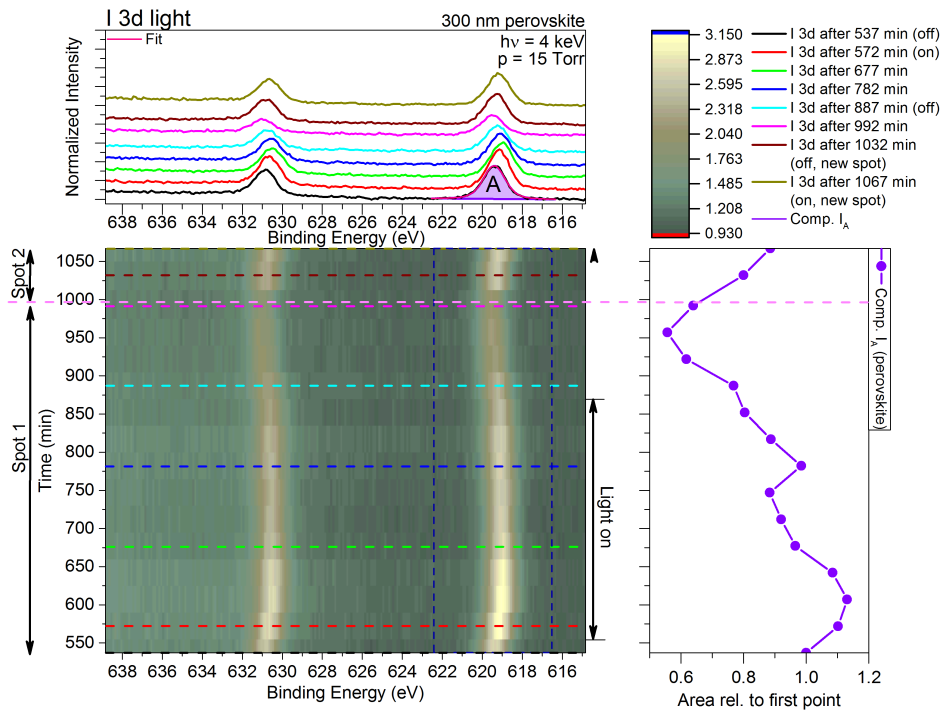


Figure B.30.: I 3d spectra and fit results of 300 nm sample over time under UV illumination at 15 Torr. Left bottom panel shows the measured I 3d as a 2D plot and representative selected spectra are shown in the left top panel as a 1D plot including the species from the fits labeled as A. The right panel shows the area of the species determined from the fits divided by the area of the first spectrum of this sequence. The dark blue dashed line in the 2D plots indicates the fit range of the species displayed on the right. The light magenta dashed line shows the change to a new sample position and the arrow between the left and right panel indicates the time frame were the sample was illuminated.

scans) after the light is turned on and only increases 70 min after the light is turned off (see right panel in Figure B.30); when going to a new spot the intensity of I seems to be less than the intensity of I of the previous spot at the beginning of the sequence measurement. The decrease of I might be, similar to the sample at low water pressure under illumination (see subsection 5.2.3), related to degradation according to equation (C1) and (C2) in Table 5.1. Where the absence of the HI species in Figure B.30 is explained by the very low amounts of HI (diluted) on the sample with its signal being below the HAXPES detection limit. Further might be also equation (C4) possible as origin for the decrease of I, if Pb^0 is formed.

Compared to I 3d (and O 1s), the 2D spectra of C 1s in Figure B.31 do not clearly show a shift

B.2 300 nm Perovskite

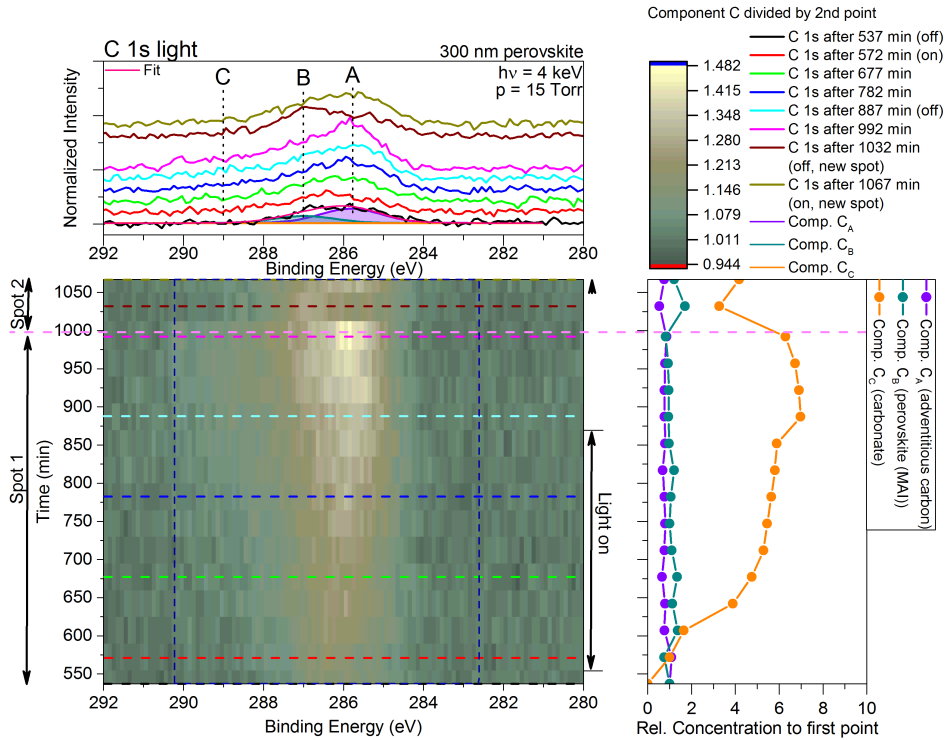


Figure B.31.: C 1s spectra and fit results of 300 nm sample over time under UV illumination at 15 Torr. Left bottom panel shows the measured C 1s as a 2D plot and representative selected spectra are shown in the left top panel as a 1D plot including the species from the fits labeled as A, B and C. The right panel shows the relative concentration of the three species determined from the fits divided by the relative concentration of the first spectrum of this sequence. The dark blue dashed line in the 2D plots indicates the fit range of the species displayed on the right. The light magenta dashed line shows the change to a new sample position and the arrow between the left and right panel indicates the time frame were the sample was illuminated.

in E_B , mainly due to the broadening of the peak attributed to the increase of carbonate signal. From the fits, three species can be identified, which are given again due to the present shift as a E_B range. C_A can be attributed to adventitious carbon in a E_B range between 285.5 and 286.1 eV, C_B to MAI between 286.7 and 287.3 eV and C_C to carbonates between 288.8 and 289.4 eV. The determined E_B for C 1s at high water vapor under illumination are in line with the determined E_B of C 1s for the other measurements, except for the 300 nm sample measured in the dark in high vacuum, which is lower in E_B . Moreover does the component related to carbonates increases under illumination with time and seems to slowly decrease when the light is turned off. This behavior is similar to the increase of the molecular water component under

Appendix B

illumination, indicating that the adsorption of carbonates is correlated to the adsorption of water. The components related to adventitious carbon and MAI are behaving differently, it seems that they stay constant over time in the scatter of the data. Although according to equation (C1) and (C2) in Table 5.1 an decrease in MAI is expected, due to the dilution of the components as discussed in subsection 5.2.3, it might also be possible that the diluted MAI stays on the sample within the detection limit.

Figure B.32 shows the Pb 4f spectra with a similar shift in E_B over time under illumination

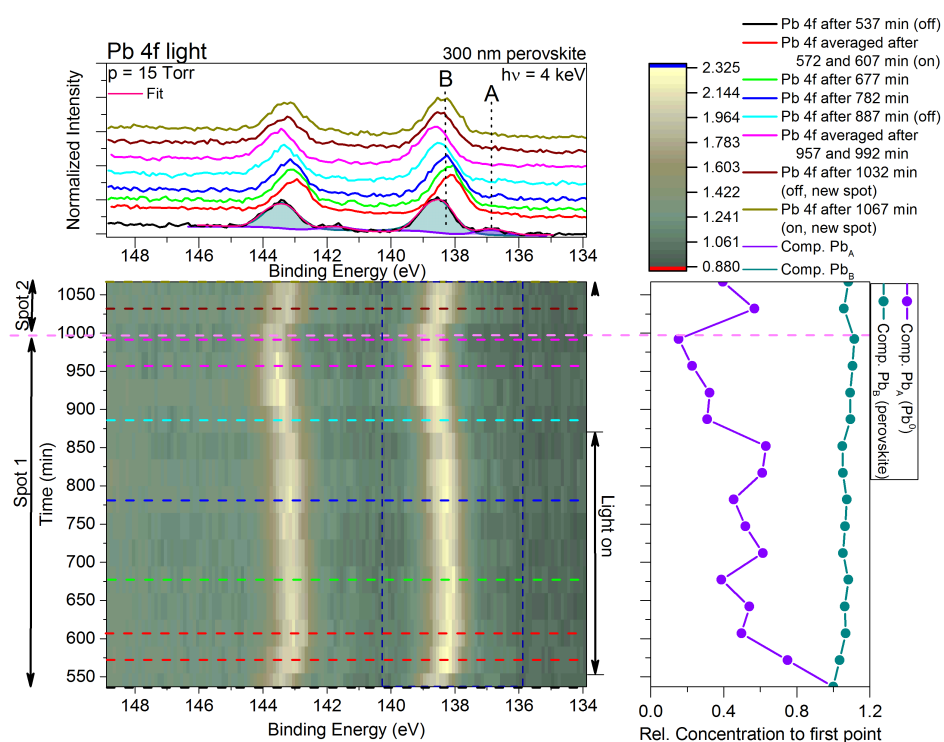


Figure B.32.: Pb 4f spectra and fit results of 300 nm sample over time under UV illumination at 15 Torr. Left bottom panel shows the measured Pb 4f as a 2D plot and representative selected spectra are shown in the left top panel as a 1D plot including the species from the fits labeled as A and B. The right panel shows the relative concentration of the two species determined from the fits divided by the relative concentration of the first spectrum of this sequence. The dark blue dashed line in the 2D plots indicates the fit range of the species displayed on the right. The light magenta dashed line shows the change to a new sample position and the arrow between the left and right panel indicates the time frame were the sample was illuminated.

as observed for the I 3d and O 1s measurements. From the fits, two species can be identified: Pb_A in the E_B range from 136.5 to 137.1 eV and Pb_B from 138.2 to 138.8 eV. As before

B.2 300 nm Perovskite

these peaks can be attributed to Pb^0 and perovskite Pb (or PbI_2) respectively and agree with the E_B obtained from the previous measurements, except for 300 nm sample in the dark in high vacuum, which is lower in E_B . In the right panel of Figure B.32 is the relative concentration over time for the different Pb species given, it seems that Pb^0 first decreases then slightly increases under illumination before it again decreases when the light is turned off. This indicates most likely two mechanism competing with each other, which might be the formation of Pb^0 and PbO as it will be discussed in the following. According to equation (C4) in Table 5.1 the formation of Pb^0 is to be expected as a degradation product, which has been confirmed for the low water pressure and under illumination experiment (see subsection 5.2.3). Further it has been seen that with the light off, the Pb^0 component decreases and it was assumed that most likely a PbO is formed without light. This could be also the case here, where first Pb^0 is formed which immediately oxidizes to PbO, reflected in the decrease of the relative contribution of Pb^0 . The slight increase of Pb^0 under illumination indicates the formation of Pb^0 outmatching the reaction to PbO until the light is turned off and no Pb^0 is further formed. Note that this is hypothetical, since PbO can not be resolved in the Pb 4f spectra. The component related to Pb perovskite (PbI_2) stays constant over time within the scatter of the data, which would be expected by back reaction of Pb^0 to PbO and adsorption of water on the perovskite.

Comparable to the sample in water vapor in the dark (see subsection 5.2.2), a water film is growing on the sample surface in water vapor under illumination. But through the wet chamber from the previous low water pressure measurements, water was already adsorbed, most likely on the perovskite surface and started to adsorb on the TiO_2 substrate under illumination (and continued water adsorption), as indicated by a slight decrease of the TiO_2 related signal (and increase of Pb^0). In the presence of water vapor (high water pressure) under illumination, the TiO_2 signal decreases significantly, whereas the Pb perovskite signal stays constant, indicating an enhanced adsorption of water on the substrate, whereas the present water film on the perovskite is getting thicker.

Appendix B

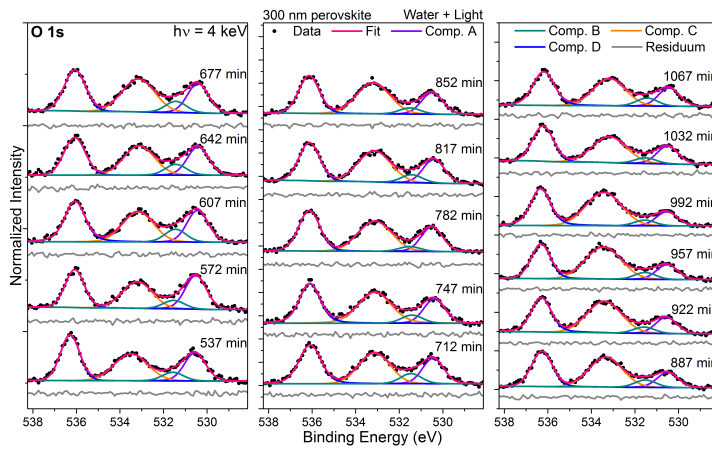


Figure B.33.: O 1s fits of 300 nm perovskite sample in water vapor under illumination.

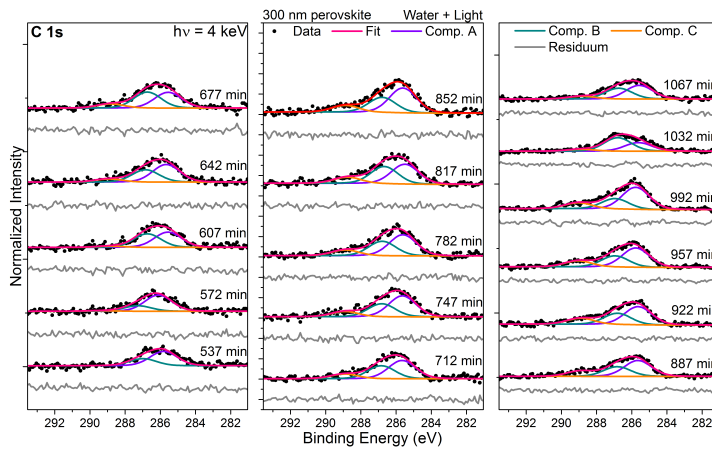


Figure B.34.: C 1s fits of 300 nm perovskite sample in water vapor under illumination.

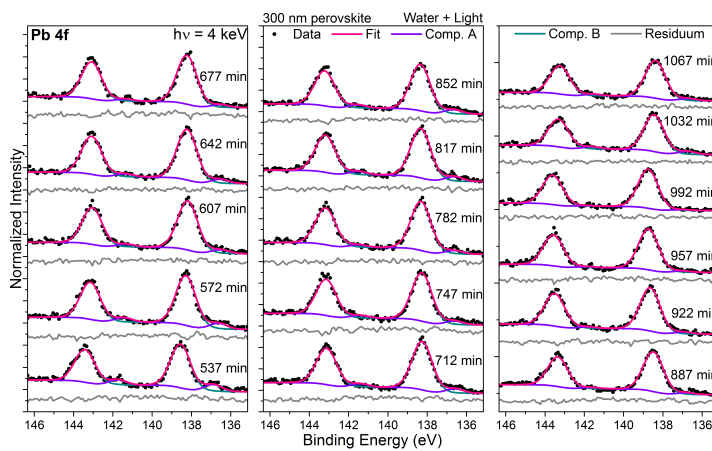


Figure B.35.: Pb 4f fits of 300 nm perovskite sample in water vapor under illumination.

B.2 300 nm Perovskite

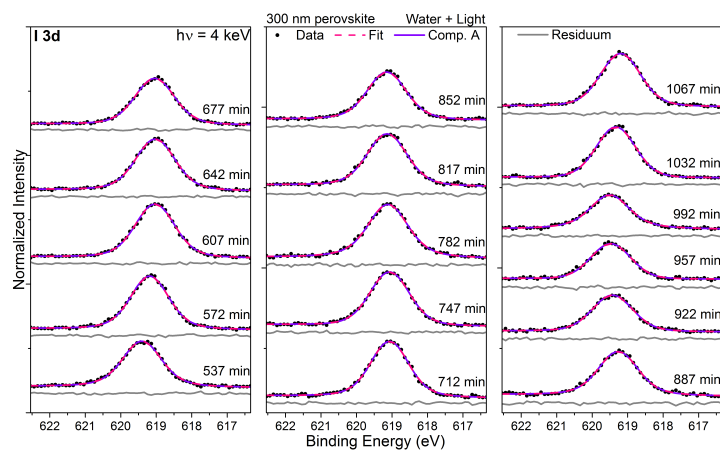


Figure B.36.: I 3d fits of 300 nm perovskite sample in water vapor under illumination.

C. Appendix C

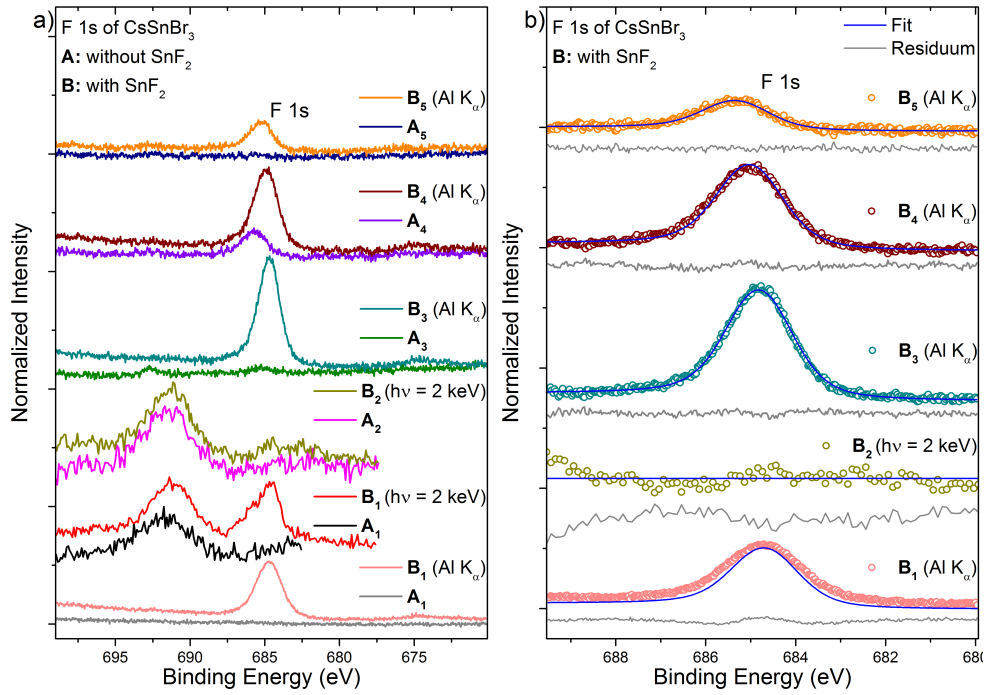


Figure C.1.: a) F 1s spectra of CsSnBr₃ without and with SnF₂ measured with an excitation energy of $h\nu = 1486.6$ eV (Al K α) and 2 keV. Spectra have been normalized to the background. b) F 1s spectra including fit analysis.

Figure C.1 a) shows the F 1s spectra, measured with an excitation energy of $h\nu = 1486.6$ eV (Al K α) and 2 keV (only for batch number 1 and 2). Note that for the energy axis of the data measured in the Sissy lab no energy calibration exists. The peak around 685 eV in Figure C.1 a) corresponds to F 1s from SnF₂ [84] and can be clearly seen for all CsSnBr₃ samples with SnF₂ (sample set B) measured in the lab. The only exception is sample A₄ where the peak might be due to cross contamination with the SnF₂ containing samples, although the samples were transported and kept in the glovebox separately. For the sample sets measured with HAXPES (A_{1,2} and B_{1,2}) an additional peak around 692 eV is present and can be ascribed to a third order Cs 4s peak [84]. Even though the same 20 mol% SnF₂ was always added to the precursor solution, the intensity of the F 1s signal varies by batch and cannot even be detected for B₂.

Appendix C

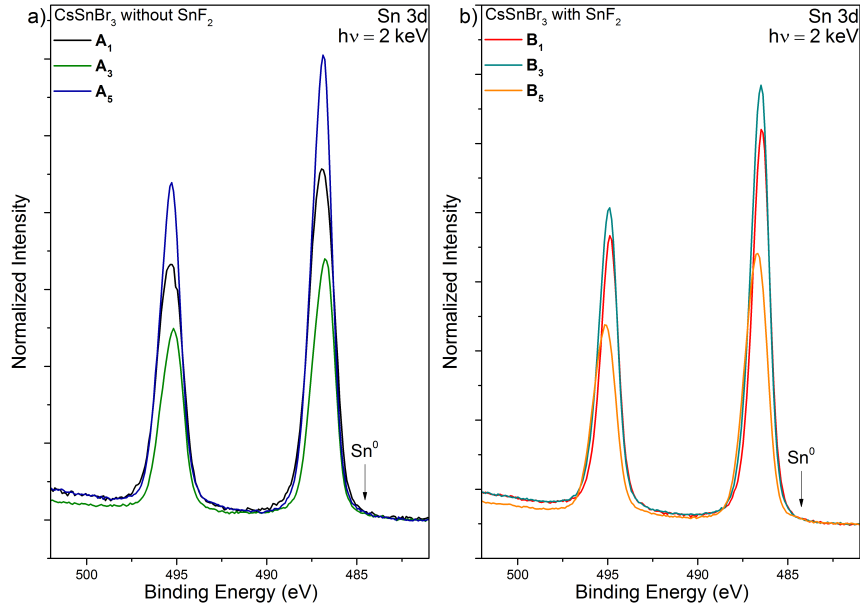


Figure C.2.: HAXPES Sn 3d detail spectra of a) CsSnBr₃ without SnF₂ (sample A_{1,3,5}) and b) CsSnBr₃ with SnF₂ (sample B_{1,3,5}). Spectra have been normalized to the background. The arrow marks the position of Sn⁰.

Table C.1.: E_B of the fitted peaks of the shallow core levels from Figure 6.2, 6.3 and 6.4 with an fitting error of ± 0.10 eV. Sample set A refers to CsSnBr₃ without SnF₂, sample set B to CsSnBr₃ with SnF₂. The index refers to the batch number. The Sn 4d_{5/2}, Br 3d_{5/2} and Cs 4d_{5/2} peaks have a main (I)/secondary (II) species contributing to the corresponding spectrum respectively.

Sample	Sn 4d _{5/2} [eV]		Cs 5s[eV]	O 2s [eV]	Br 3d _{5/2} [eV]		Cs 4d _{5/2} [eV]	
	I	II			I	II	I	II
A ₁	25.51 eV	26.27 eV	23.36 eV	22.15 eV	68.40 eV	69.06 eV	75.52 eV	75.11 eV
A ₂	25.44 eV	26.19 eV	22.99 eV	21.93 eV	68.21 eV	68.87 eV	75.31 eV	74.83 eV
A ₃	25.55 eV	26.36 eV	23.17 eV	21.81 eV	68.38 eV	68.94 eV	75.45 eV	74.92 eV
A ₄	25.50 eV	26.30 eV	23.28 eV	21.93 eV	68.36 eV	69.04 eV	75.42 eV	74.85 eV
A ₅	25.70 eV	26.53 eV	23.20 eV	22.02 eV	68.39 eV	68.95 eV	75.33 eV	74.75 eV
B ₁	25.39 eV	26.12 eV	23.33 eV	21.91 eV	68.28 eV	68.77 eV	75.42 eV	74.78 eV
B ₂	25.23 eV	25.93 eV	-	22.07 eV	68.12 eV	68.72 eV	75.22 eV	74.80 eV
B ₃	25.38 eV	26.11 eV	23.30 eV	21.38 eV	68.28 eV	68.76 eV	75.41 eV	74.90 eV
B ₄	25.35 eV	26.05 eV	23.20 eV	21.35 eV	68.26 eV	68.82 eV	75.37 eV	74.66 eV
B ₅	25.48 eV	26.22 eV	23.32 eV	21.98 eV	68.34 eV	69.03 eV	75.39 eV	74.71 eV

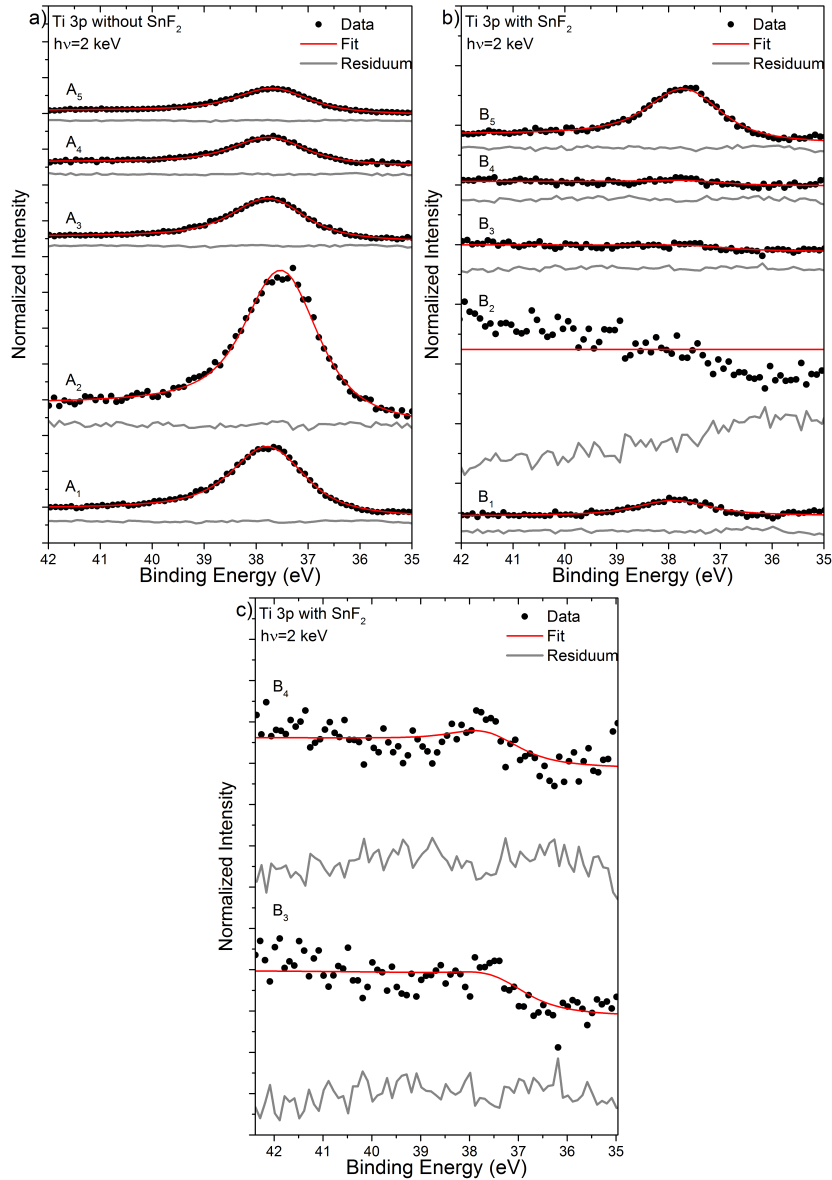


Figure C.3.: HAXPES Ti 3p detail spectra (including fit analysis) of a) CsSnBr₃ without SnF₂ (sample set A) and b) CsSnBr₃ with SnF₂ (sample set B) from the shallow core levels in Figure 6.1. The raw data is shown as circles, the spectra were normalized by the background intensity at the lower E_B around E_F and the resulting fits are given as red lines. The corresponding residuum is shown below each spectrum and the spectral background fitted using the Shirley background. c) Shows separately B₃ and B₄ of b) for clarity.

Appendix C

Table C.2.: Compositions and relative intensities calculated/obtained from the fits of wet-chemically deposited CsSnBr₃ samples without (A) and with (B) SnF₂ prepared sequentially in different batches.

Batch number	Cs/Sn		Br/Sn		Ti 3p		F 1s	F/Sn	Cs/Sn ⁴⁺		Sn 3p _{3/2}
	A	B	A	B	A	B	B	B	A	B	B
1	0.35	0.36	1.66	1.60	0.67	0.047	0.063	0.107	0.794	2.035	3.66
2	0.68	0.05	2.68	0.93	1.35	0	0	0	1.553	0.166	9.17
3	0.82	0.38	3.10	1.45	0.41	0.007	0.115	0.226	2.5	1.476	3.18
4	0.42	0.32	2.03	1.37	0.27	0.009	0.088	0.129	1.070	1.302	4.27
5	0.45	0.16	2.17	1.36	0.25	0.152	0.031	0.051	1.410	0.431	3.75

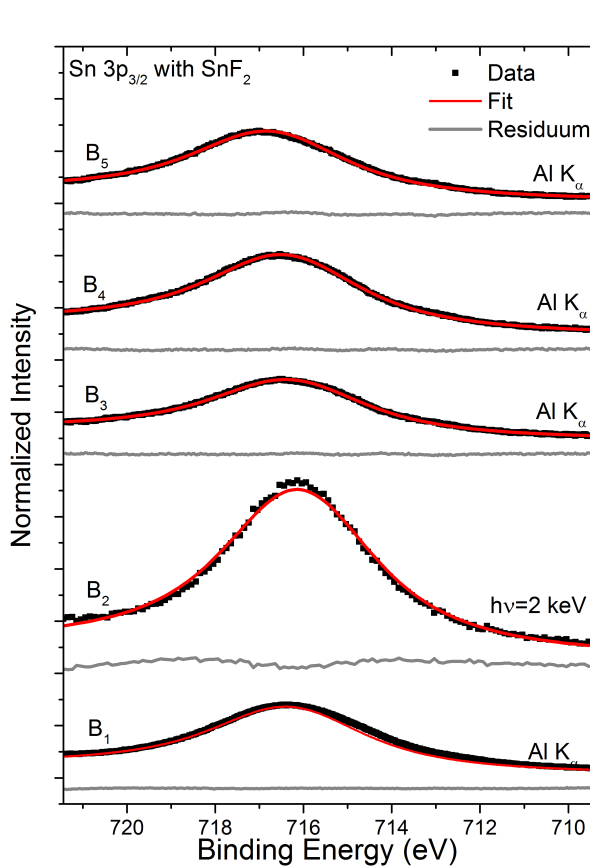


Figure C.4.: Sn 3p_{3/2} fits of sample set B. Note that all samples, except B₂, were measured in the lab.

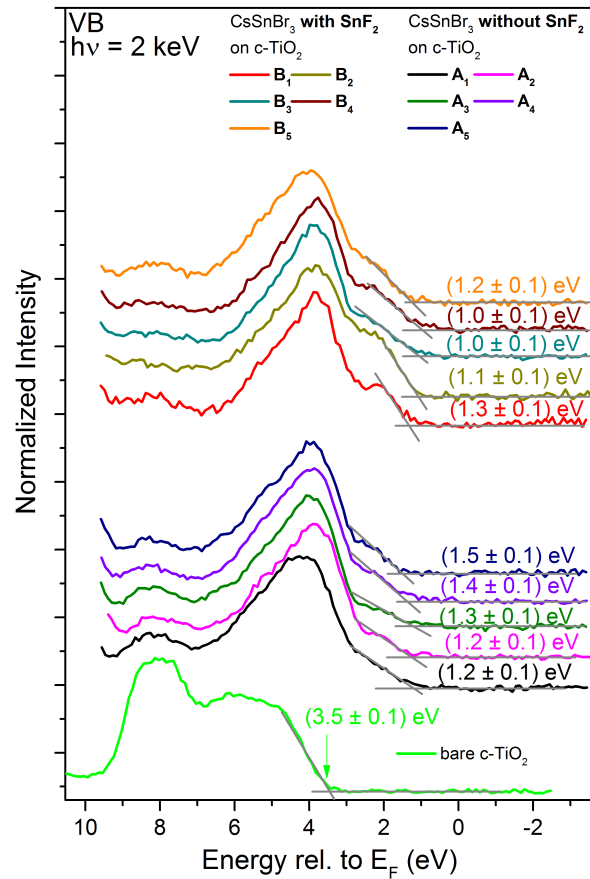


Figure C.5.: VB spectra of wet-chemically deposited CsSnBr₃ without (A) and with (B) SnF₂ as well as bare c-TiO₂ (including linear extrapolation of VBM).

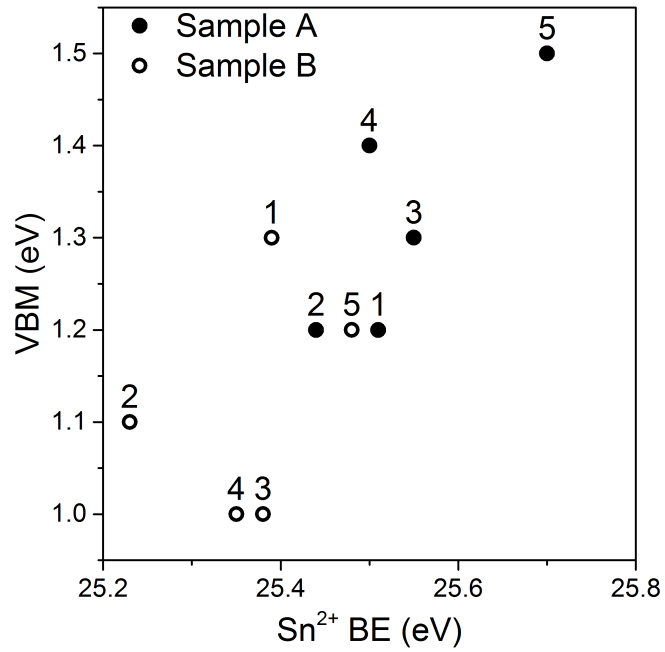


Figure C.6.: VBM positions plotted over $\text{Sn}^{2+} E_B$ for the two sample sets. Numbers above the data points correspond to batch number. The error of ± 0.1 eV is not displayed for better clarity.

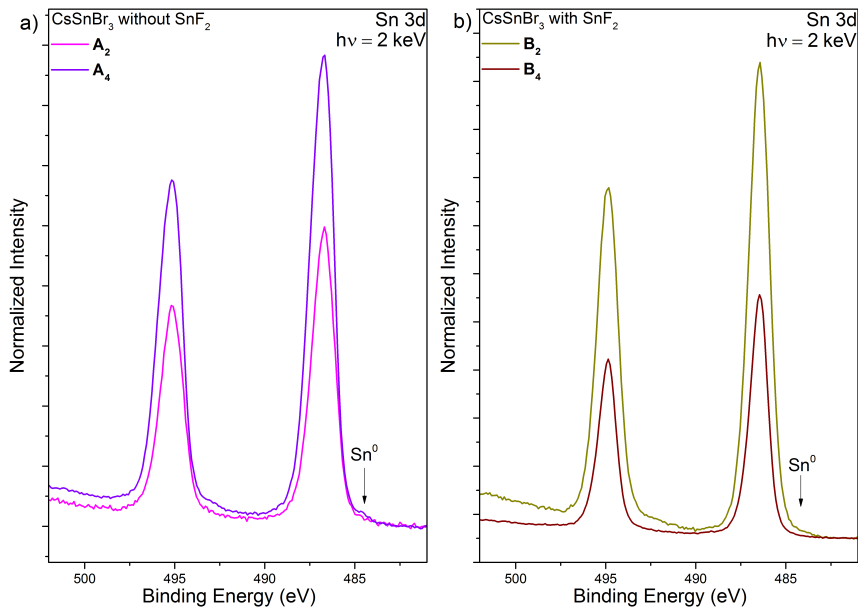


Figure C.7.: HAXPES Sn 3d detail spectra of a) CsSnBr_3 without SnF_2 (sample $A_{2,4}$) and b) CsSnBr_3 with SnF_2 (sample $B_{2,4}$). Spectra have been normalized to the background. The arrow marks the position of Sn^0 .

Appendix C

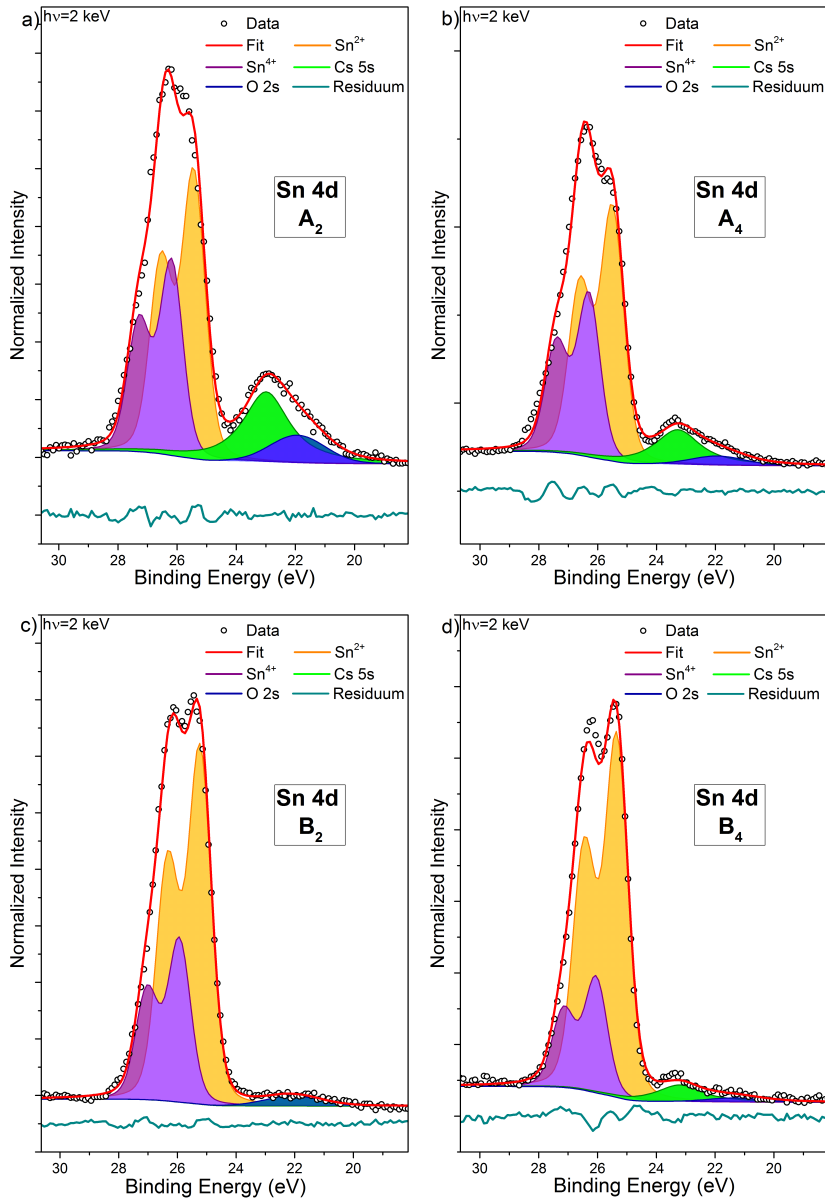


Figure C.8.: HAXPES Sn 4d detail spectra (including fit analysis) of CsSnBr₃ samples without SnF₂ (A₂, A₄) and with SnF₂ (B₂, B₄) from the shallow core levels in Figure 6.1. The raw data is shown as open circles, the spectra were normalized by the background intensity at the lower E_B around E_F and the resulting fits are given as red lines. The different contributions due to spin-orbit splitting and different Sn species are given as shaded areas in orange (Sn²⁺) and purple (Sn⁴⁺). The corresponding residuum is shown below each spectrum and the spectral background fitted using the Shirley background.

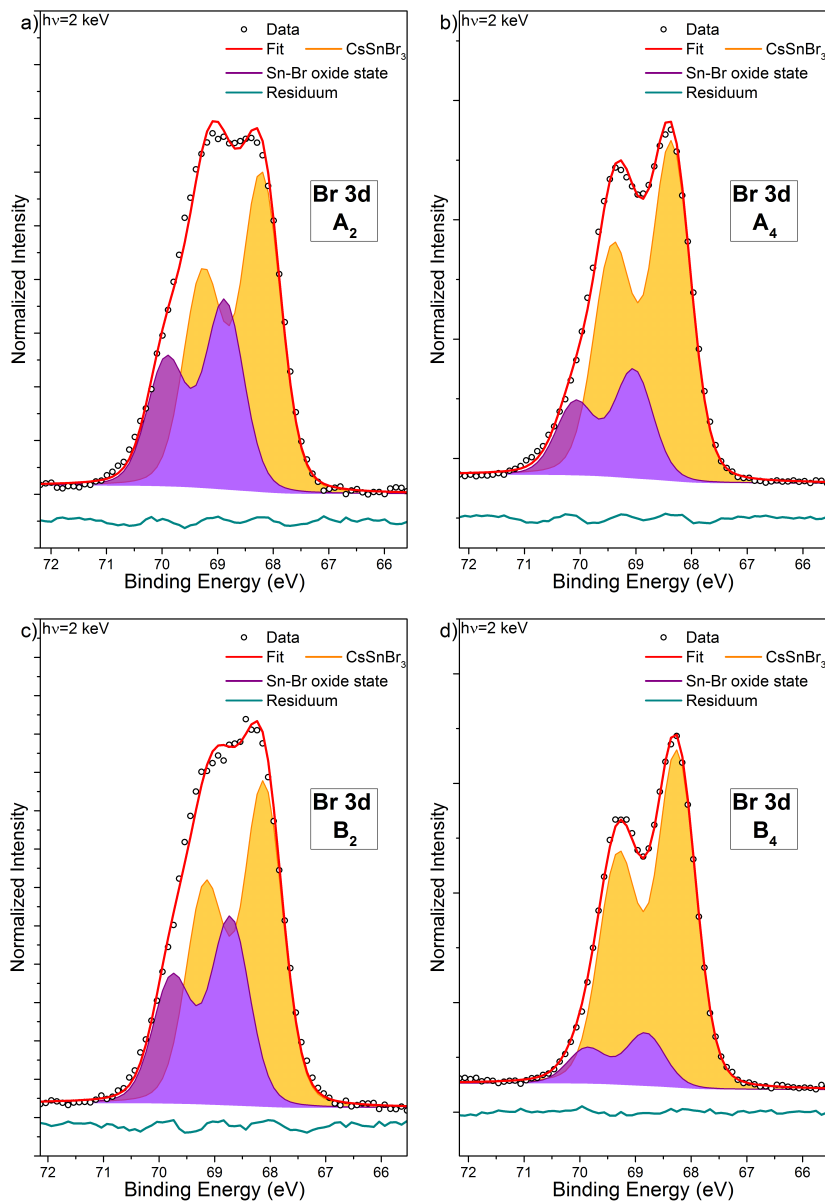


Figure C.9.: HAXPES Br 3d detail spectra (including fit analysis) of CsSnBr_3 samples without SnF_2 (A_2 , A_4) and with SnF_2 (B_2 , B_4) from the shallow core levels in Figure 6.1. The raw data is shown as open circles, the spectra were normalized by the background intensity at the lower E_B around E_F and the resulting fits are given as red lines. The different contributions due to spin-orbit splitting and different Br species are given as shaded areas in orange (CsSnBr_3) and purple (Sn-Br oxide state). The corresponding residuum is shown below each spectrum and the spectral background fitted using the Shirley background.

Appendix C

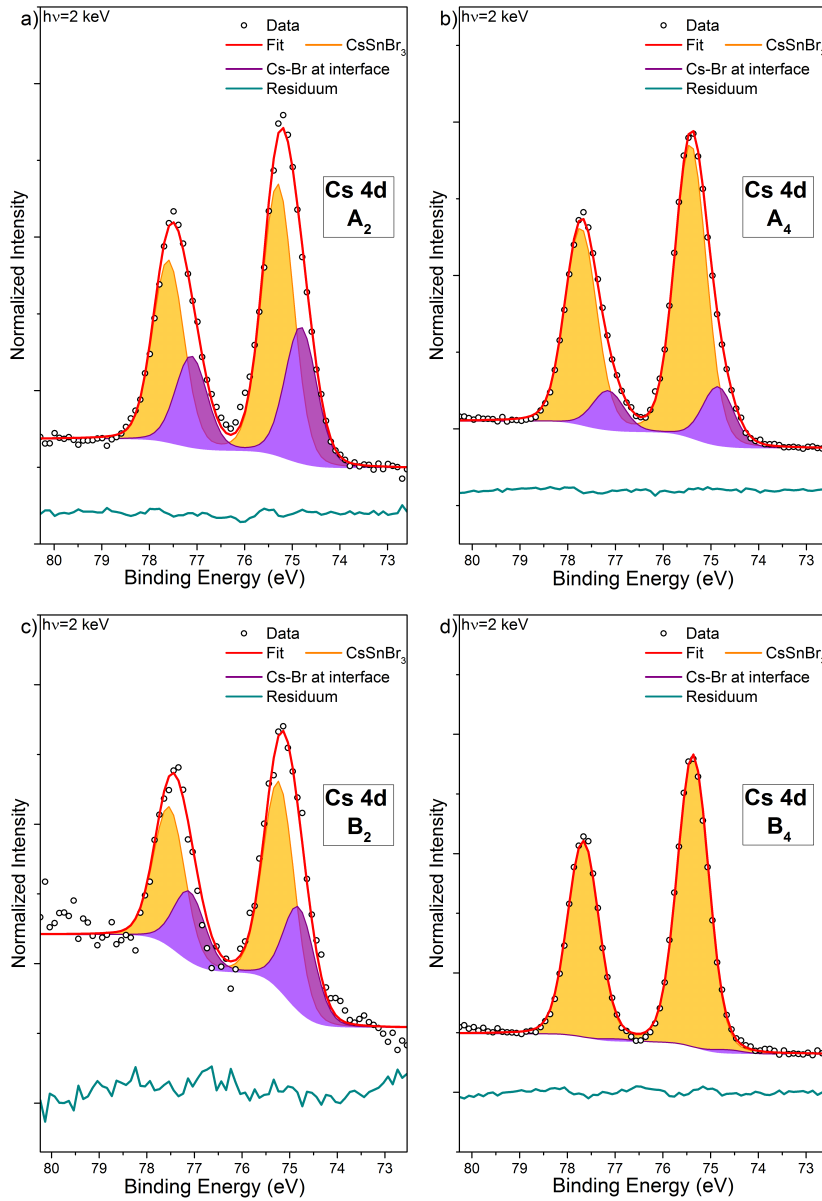


Figure C.10.: HAXPES Cs 4d detail spectra (including fit analysis) of CsSnBr_3 samples without SnF_2 (A_2 , A_4) and with SnF_2 (B_2 , B_4) from the shallow core levels in Figure 6.1. The raw data is shown as open circles, the spectra were normalized by the background intensity at the lower E_B around E_F and the resulting fits are given as red lines. The different contributions due to spin-orbit splitting and different Cs species are given as shaded areas in orange (CsSnBr_3) and purple (Cs-Br interface species). The corresponding residuum is shown below each spectrum and the spectral background fitted using the Shirley background.

Bibliography

- [1] A. M. Bagher, M. M. A. Vahid, and M. Mohsen. "Types of Solar Cells and Application". *American Journal of Optics and Photonics*, 3:94–113, 2015.
- [2] NREL. Efficiency chart, http://www.nrel.gov/ncpv/images/efficiency_chart.jpg, last accessed 09.08.2017.
- [3] H. J. Snaith. "Perovskites: The Emergence of a New Era for Low-Cost, High-Efficiency Solar Cells". *The Journal of Physical Chemistry Letters*, 4(21):3623–3630, 2013.
- [4] H.-S. Kim, C.-R. Lee, J.-H. Im, K.-B. Lee, T. Moehl, A. Marchioro, S.-J. Moon, R. Humphry-Baker, J.-H. Yum, J. E. Moser, M. Grätzel, and N.-G. Park. "Lead Iodide Perovskite Sensitized All-Solid-State Submicron Thin Film Mesoscopic Solar Cell with Efficiency Exceeding 9%". *Scientific Reports*, 2:591, 2012.
- [5] M. M. Lee, J. Teuscher, T. Miyasaka, T. N. Murakami, and H. J. Snaith. "Efficient Hybrid Solar Cells Based on Meso-Superstructured Organometal Halide Perovskites". *Science*, 338(6107):643–647, 2012.
- [6] M. Liu, M. B. Johnston, and H. J. Snaith. "Efficient planar heterojunction perovskite solar cells by vapour deposition". *Nature*, 501(7467):395, 2013.
- [7] H. Zhou, Q. Chen, G. Li, S. Luo, T.-b. Song, H.-S. Duan, Z. Hong, J. You, Y. Liu, and Y. Yang. "Interface engineering of highly efficient perovskite solar cells". *Science*, 345(6196):542–546, 2014.
- [8] T. Leijtens, G. E. Eperon, N. K. Noel, S. N. Habisreutinger, A. Petrozza, and H. J. Snaith. "Stability of Metal Halide Perovskite Solar Cells". *Advanced Energy Materials*, 5(20):1500963, 2015.
- [9] R. G. Wilks and M. Bär. "Perovskite solar cells: Danger from within". *Nature Energy*, 2:16204, 2017.

Bibliography

- [10] Y. Li, L. Meng, Y. (M.) Yang, G. Xu, Z. Hong, Q. Chen, J. You, G. Li, Y. Yang, and Y. Li. "High-efficiency robust perovskite solar cells on ultrathin flexible substrates". *Nature Communications*, 7:10214, 2016.
- [11] E. L. Unger, L. Kegelman, K. Suchan, D. Sorell, L. Korte, and S. Albrecht. "Roadmap and roadblocks for the band gap tunability of metal halide perovskites". *Journal of Materials Chemistry A*, 5:11401–11409, 2017.
- [12] S. Albrecht, M. Saliba, J. P. C. Baena, F. Lang, L. Kegelman, M. Mews, L. Steier, A. Abate, J. Rappich, L. Korte, R. Schlattmann, M. Khaja Nazeeruddin, A. Hagfeldt, M. Gratzel, and B. Rech. "Monolithic perovskite/silicon-heterojunction tandem solar cells processed at low temperature". *Energy & Environmental Science*, 9:81–88, 2016.
- [13] Z. Song, S. C. Watthage, A. B. Phillips, and M. J. Heben. "Pathways toward high-performance perovskite solar cells: review of recent advances in organo-metal halide perovskites for photovoltaic applications". *Journal of Photonics for Energy*, 6(2):022001, 2016.
- [14] M. Seetharaman S, P. Nagarjuna, P. N. Kumar, S. P. Singh, M. Deepa, and M. A. G. Namboothiry. "Efficient organic-inorganic hybrid perovskite solar cells processed in air". *Physical Chemistry Chemical Physics*, 16:24691–24696, 2014.
- [15] G. E. Eperon, V. M. Burlakov, P. Docampo, A. Goriely, and H. J. Snaith. "Morphological Control for High Performance, Solution-Processed Planar Heterojunction Perovskite Solar Cells". *Advanced Functional Materials*, 24(1):151–157, 2014.
- [16] G. Niu, X. Guo, and L. Wang. "Review of recent progress in chemical stability of perovskite solar cells". *Journal of Materials Chemistry A*, 3:8970–8980, 2015.
- [17] B. Philippe, B.-W. Park, R. Lindblad, J. Oscarsson, S. Ahmadi, E. M. J. Johansson, and H. Rensmo. "Chemical and Electronic Structure Characterization of Lead Halide Perovskites and Stability Behavior under Different Exposures-A Photoelectron Spectroscopy Investigation". *Chemistry of Materials*, 27(5):1720–1731, 2015.
- [18] J. Schoonman. "Organic-inorganic lead halide perovskite solar cell materials: A possible stability problem". *Chemical Physics Letters*, 619:193–195, 2015.
- [19] X. Tang, M. Brandl, B. May, I. Levchuk, Y. Hou, M. Richter, H. Chen, S. Chen, S. Kahmann, A. Osvet, F. Maier, H.-P. Steinruck, R. Hock, G. J. Matt, and C. J. Brabec. "Pho-

Bibliography

- toinduced degradation of methylammonium lead triiodide perovskite semiconductors". *Journal of Materials Chemistry A*, 4:15896–15903, 2016.
- [20] Y. Li, X. Xu, C. Wang, B. Ecker, J. Yang, J. Huang, and Y. Gao. "Light-Induced Degradation of $\text{CH}_3\text{NH}_3\text{PbI}_3$ Hybrid Perovskite Thin Film". *The Journal of Physical Chemistry C*, 121(7):3904–3910, 2017.
- [21] N. Rajamanickam, S. Kumari, V. K. Vendra, B. W. Lavery, J. Spurgeon, T. Druffel, and M. K. Sunkara. "Stable and durable $\text{CH}_3\text{NH}_3\text{PbI}_3$ perovskite solar cells at ambient conditions". *Nanotechnology*, 27(23):235404, 2016.
- [22] X. Dong, X. Fang, M. Lv, B. Lin, S. Zhang, J. Ding, and N. Yuan. "Improvement of the humidity stability of organic-inorganic perovskite solar cells using ultrathin Al_2O_3 layers prepared by atomic layer deposition". *Journal of Materials Chemistry A*, 3:5360–5367, 2015.
- [23] G. Niu, W. Li, F. Meng, L. Wang, H. Dong, and Y. Qiu. "Study on the stability of $\text{CH}_3\text{NH}_3\text{PbI}_3$ films and the effect of post-modification by aluminum oxide in all-solid-state hybrid solar cells". *Journal of Materials Chemistry A*, 2:705–710, 2014.
- [24] Y. Han, S. Meyer, Y. Dkhissi, K. Weber, J. M. Pringle, U. Bach, L. Spiccia, and Y.-B. Cheng. "Degradation observations of encapsulated planar $\text{CH}_3\text{NH}_3\text{PbI}_3$ perovskite solar cells at high temperatures and humidity". *Journal of Materials Chemistry A*, 3:8139 – 8147, 2015.
- [25] S. Gupta, T. Bendikov, G. Hodes, and D. Cahen. " CsSnBr_3 , A Lead-Free Halide Perovskite for Long-Term Solar Cell Application: Insights on SnF_2 Addition". *ACS Energy Letters*, 1(5):1028–1033, 2016.
- [26] Z. Chen, J. J. Wang, Y. Ren, C. Yu, and K. Shum. "Schottky solar cells based on CsSnI_3 thin-films". *Applied Physics Letters*, 101(9):093901, 2012.
- [27] I. Chung, J.-H. Song, J. Im, J. Androulakis, C. D. Malliakas, H. Li, A. J. Freeman, J. T. Kenney, and M. G. Kanatzidis. " CsSnI_3 : Semiconductor or Metal? High Electrical Conductivity and Strong Near-Infrared Photoluminescence from a Single Material. High Hole Mobility and Phase-Transitions". *Journal of the American Chemical Society*, 134(20):8579–8587, 2012.

Bibliography

- [28] S. J. Lee, S. S. Shin, Y. C. Kim, D. Kim, T. K. Ahn, J. H. Noh, J. Seo, and S. I. Seok. "Fabrication of Efficient Formamidinium Tin Iodide Perovskite Solar Cells through SnF₂-Pyrazine Complex". *Journal of the American Chemical Society*, 138(12):3974–3977, 2016.
- [29] M. H. Kumar, S. Dharani, W. L. Leong, P. P. Boix, R. R. Prabhakar, T. Baikie, C. Shi, H. Ding, R. Ramesh, M. Asta, M. Graetzel, S. G. Mhaisalkar, and N. Mathews. "Lead-Free Halide Perovskite Solar Cells with High Photocurrents Realized Through Vacancy Modulation". *Advanced Materials*, 26(41):7122–7127, 2014.
- [30] Reference Solar Spectral Irradiance: Air Mass 1.5. Online available: <http://rredc.nrel.gov/solar/spectra/am1.5/>.
- [31] PVEDUCATION.ORG; standard solar spectra table. [Online]. Available: <http://www.pveducation.org/pvcdrom/appendices/standard-solar-spectra>.
- [32] W. Shockley and H. J. Queisser. "Detailed Balance Limit of Efficiency of p-n Junction Solar Cells". *Journal of Applied Physics*, 32(3):510–519, 1961.
- [33] S. Rühle. "Tabulated values of the Shockley-Queisser limit for single junction solar cells". *Solar Energy*, 130:139 – 147, 2016.
- [34] B. O'Regan and M. Grätzel. "A low-cost, high-efficiency solar cell based on dye-sensitized colloidal TiO₂ films". *Nature*, 353:737 – 740, 1991.
- [35] A. Kojima, K. Teshima, Y. Shirai, and T. Miyasaka. "Organometal Halide Perovskites as Visible-Light Sensitizers for Photovoltaic Cells". *Journal of the American Chemical Society*, 131(17):6050 – 6051, 2009.
- [36] W. S. Yang, J. H. Noh, N. J. Jeon, Y. C. Kim, S. Ryu, J. Seo, and S. I. Seok. "High-performance photovoltaic perovskite layers fabricated through intramolecular exchange". *Science*, 348(6240):1234–1237, 2015.
- [37] W. S. Yang, B.-W. Park, E. H. Jung, N. J. Jeon, Y. C. Kim, D. U. Lee, S. S. Shin, J. Seo, E. K. Kim, J. H. Noh, and S. I. Seok. "Iodide management in formamidinium-lead-halide-based perovskite layers for efficient solar cells". *Science*, 356(6345):1376–1379, 2017.

Bibliography

- [38] S. D. Stranks and H. J. Snaith. "Metal-halide perovskites for photovoltaic and light-emitting devices". *Nature Nanotechnology*, 10:391 – 402, 2015.
- [39] S. A. Kulkarni, T. Baikie, P. P. Boix, N. Yantara, N. Mathews, and S. Mhaisalkar. "band-gap tuning of lead halide perovskites using a sequential deposition process". *Journal of Materials Chemistry A*, 2:9221–9225, 2014.
- [40] Z. Wang, D. P. McMeekin, N. Sakai, S. van Reenen, K. Wojciechowski, J. B. Patel, M. B. Johnston, and H. J. Snaith. "Efficient and Air-Stable Mixed-Cation Lead Mixed-Halide Perovskite Solar Cells with n-Doped Organic Electron Extraction Layers". *Advanced Materials*, 29(5):1604186, 2017.
- [41] S. N. Habisreutinger, D. P. McMeekin, H. J. Snaith, and R. J. Nicholas. "Research Update: Strategies for improving the stability of perovskite solar cells". *APL Materials*, 4(9):091503, 2016.
- [42] J. M. Ball, M. M. Lee, A. Hey, and H. J. Snaith. "Low-temperature processed meso-superstructured to thin-film perovskite solar cells". *Energy & Environmental Science*, 6:1739–1743, 2013.
- [43] M. T. Hörantner, P. K. Nayak, S. Mukhopadhyay, K. Wojciechowski, C. Beck, D. McMeekin, B. Kamino, G. E. Eperon, and H. J. Snaith. "Shunt-Blocking Layers for Semitransparent Perovskite Solar Cells". *Advanced Materials Interfaces*, 3(10):1500837, 2016.
- [44] I. Hwang, I. Jeong, J. Lee, M. J. Ko, and K. Yong. "Enhancing Stability of Perovskite Solar Cells to Moisture by the Facile Hydrophobic Passivation". *ACS Applied Materials & Interfaces*, 7(31):17330 – 17336, 2015.
- [45] T. Leijtens, G. E. Eperon, S. Pathak, A. Abate, M. M. Lee, and H. J. Snaith. "Overcoming ultraviolet light instability of sensitized TiO₂ with meso-superstructured organometal tri-halide perovskite solar cells". *Nature Communications*, 4:2885, 2013.
- [46] C.-Y. Chen, M. Wang, J.-Y. Li, N. Pootrakulchote, L. Alibabaei, C.-h. Ngoc-le, J.-D. Decoppet, J.-H. Tsai, C. Grätzel, C.-G. Wu, S. M. Zakeeruddin, and M. Grätzel. "Highly Efficient Light-Harvesting Ruthenium Sensitizer for Thin-Film Dye-Sensitized Solar Cells". *ACS Nano*, 3(10):3103–3109, 2009.

Bibliography

- [47] H.-S. Kim, J.-Y. Seo, and N.-G. Park. "Material and Device Stability in Perovskite Solar Cells". *ChemSusChem*, 9(18):2528–2540, 2016.
- [48] J. C.-R. Ke, A. S. Walton, D. J. Lewis, A. Tedstone, P. O'Brien, A. G. Thomas, and W. R. Flavell. "In situ investigation of degradation at organometal halide perovskite surfaces by x-ray photoelectron spectroscopy at realistic water vapour pressure". *Chemical Communications*, 53:5231–5234, 2017.
- [49] W.-J. Yin, J.-H. Yang, J. Kang, Y. Yan, and S.-H. Wei. "halide perovskite materials for solar cells: a theoretical review". *Journal of Materials Chemistry A*, 3:8926–8942, 2015.
- [50] S. D. Stranks, G. E. Eperon, G. Grancini, C. Menelaou, M. J. P. Alcocer, T. Leijtens, L. M. Herz, A. Petrozza, and H. J. Snaith. "Electron-Hole Diffusion Lengths Exceeding 1 Micrometer in an Organometal Trihalide Perovskite Absorber". *Science*, 342(6156):341–344, 2013.
- [51] S. Colella, E. Mosconi, P. Fedeli, A. Listorti, F. Gazza, F. Orlandi, P. Ferro, T. Besagni, A. Rizzo, G. Calestani, G. Gigli, F. De Angelis, and R. Mosca. "MAPbI_{3-x}Cl_x Mixed Halide Perovskite for Hybrid Solar Cells: The Role of Chloride as Dopant on the Transport and Structural Properties". *Chemistry of Materials*, 25(22):4613–4618, 2013.
- [52] J. Liu and O. V. Prezhdo. "Chlorine Doping Reduces Electron-Hole Recombination in Lead Iodide Perovskites: Time-Domain Ab Initio Analysis". *The Journal of Physical Chemistry Letters*, 6(22):4463–4469, 2015.
- [53] D. E. Starr, G. Sadoughi, E. Handick, R. G. Wilks, J. H. Alsmeier, L. Köhler, M. Gorgoi, H. J. Snaith, and M. Bär. "Direct observation of an inhomogeneous chlorine distribution in CH₃NH₃PbI_{3-x}Cl_x layers: surface depletion and interface enrichment". *Energy & Environmental Science*, 8:1609–1615, 2015.
- [54] Hui Yu, Feng Wang, Fangyan Xie, Wenwu Li, Jian Chen, and Ni Zhao. "The Role of Chlorine in the Formation Process of "CH₃NH₃PbI_{3-x}Cl_x" Perovskite". *Advanced Functional Materials*, 24(45):7102–7108, 2014.
- [55] U.S. Department of Health National Toxicology Program and Human Services. "Organotin (Methyl and Butyl) Toxicity", https://ntp.niehs.nih.gov/ntp/htdocs/chem_background/exsumpdf/organotins_508.pdf.

Bibliography

- [56] M. Kulbak, S. Gupta, N. Kedem, I. Levine, T. Bendikov, G. Hodes, and D. Cahen. "Cesium Enhances Long-Term Stability of Lead Bromide Perovskite-Based Solar Cells". *The Journal of Physical Chemistry Letters*, 7(1):167–172, 2016.
- [57] H. Lüth. *"Solid Surfaces, Interfaces and Thin Films"*. Graduate Texts in Physics. Springer Berlin Heidelberg, 2010.
- [58] D. Abou-Ras, T. Kirchartz, and U. Rau. *"Advanced Characterization Techniques for Thin Film Solar Cells"*. WILEY-VCH Verlag GmbH & Co. KGaG, 2011.
- [59] R. Fink, M.R. Weiss, E. Umbach, D. Preikszas, H. Rose, R. Spehr, P. Hartel, W. Engel, R. Degenhardt, R. Wichtendahl, H. Kuhlenbeck, W. Erlebach, K. Ihmann, R. Schlögl, H.-J. Freund, A.M. Bradshaw, G. Lilienkamp, Th. Schmidt, E. Bauer, and G. Benner. "SMART: a planned ultrahigh-resolution spectromicroscope for BESSY II". *Journal of Electron Spectroscopy and Related Phenomena*, 84(1 - 3):231 – 250, 1997.
- [60] Th. Schmidt, U. Groh, R. Fink, E. Umbach, O. Schaff, W. Engel, B. Richter, H. Kuhlenbeck, R. Schlögl, H.-J. Freund, A. M. Bradshaw, D. Preikszas, P. Hartel, R. Spehr, H. Rose, G. Lilienkamp, E. Bauer, and G. Benner. "XPEEM WITH ENERGY-FILTERING: ADVANTAGES AND FIRST RESULTS FROM THE SMART PROJECT". *Surface Review and Letters*, 09(01):223–232, 2002.
- [61] "Fityk". Available: <http://fityk.nieto.pl/>.
- [62] Unifit 2016. Available: <http://home.uni-leipzig.de/unifit/>.
- [63] M.B. Trzhaskovskaya, V.I. Nefedov, and V.G. Yarzhemsky. "Photoelectron angular distribution parameters for elements $Z=1$ to $Z=54$ in the photoelectron energy range 100-5000 eV". *Atomic Data and Nuclear Data Tables*, 77(1):97 – 159, 2001.
- [64] M.B. Trzhaskovskaya, V.I. Nefedov, and V.G. Yarzhemsky. "Photoelectron angular distribution parameters for elements $Z=55$ to $Z=100$ in the photoelectron energy range 100-5000 eV". *Atomic Data and Nuclear Data Tables*, 82(2):257 – 311, 2002.
- [65] M. P. Seah and W. A. Dench. "Quantitative electron spectroscopy of surfaces: A standard data base for electron inelastic mean free paths in solids". *Surface and Interface Analysis*, 1(1):2–11, 1979.
- [66] S. Tougaard. QUASES-IMFP-TPP2M, 2002.

Bibliography

- [67] S. Tanuma, C. J. Powell, and D. R. Penn. "Calculations of electron inelastic mean free paths. V. Data for 14 organic compounds over the 50 - 2000 eV range". *Surface and Interface Analysis*, 21(3):165–176, 1994.
- [68] P. Schulz, E. Edri, S. Kirmayer, G. Hodes, D. Cahen, and A. Kahn. "Interface energetics in organo-metal halide perovskite-based photovoltaic cells". *Energy & Environmental Science*, 7:1377–1381, 2014.
- [69] J. R. Waldrop, R. W. Grant, S. P. Kowalczyk, and E. A. Kraut. "Measurement of semiconductor heterojunction band discontinuities by x-ray photoemission spectroscopy". *Journal of Vacuum Science & Technology A: Vacuum, Surfaces, and Films*, 3(3):835–841, 1985.
- [70] D. Briggs and M.P. Seah. *Practical Surface Analysis: Auger and X-ray Photoelectron Spectroscopy*. John Wiley & Sons Ltd, 1983.
- [71] D. Attwood. *Soft X-Rays and Extreme Ultraviolet Radiation - Principles and Applications*. Cambridge University Press, 1992.
- [72] M. Gorgoi, S. Svensson, F. Schäfers, G. Öhrwall, M. Mertin, P. Bressler, O. Karis, H. Siegbahn, A. Sandell, H. Rensmo, W. Doherty, C. Jung, W. Braun, and W. Eberhardt. "The high kinetic energy photoelectron spectroscopy facility at BESSY progress and first results". *Nuclear Instruments and Methods in Physics Research Section A: Accelerators, Spectrometers, Detectors and Associated Equipment*, 601(1 - 2):48–53, 2009. Special issue in honour of Prof. Kai Siegbahn.
- [73] F. Schaefer, M. Mertin, and M. Gorgoi. "KMC-1: A high resolution and high flux soft x-ray beamline at BESSY". *Review of Scientific Instruments*, 78(12):123102, 2007.
- [74] S. Axnanda, E. J. Crumlin, B. Mao, S. Rani, R. Chang, P. G. Karlsson, M. O. M. Edwards, M. Lundqvist, R. Moberg, P. Ross, Z. Hussain, and Z. Liu. "Using "Tender" X-ray Ambient Pressure X-Ray Photoelectron Spectroscopy as A Direct Probe of Solid-Liquid Interface". *Scientific Reports*, 5:9788, 2015.
- [75] C. Hartmann, G. Sadoughi, R. Félix, E. Handick, H. W. Klemm, G. Peschel, E. Madej, A. B. Fuhrich, X. Liao, S. Raoux, D. Abou-Ras, D. Wargulski, T. Schmidt, R. G. Wilks, H. Snaith, and M. Bär. "Spatially Resolved Insight into the Chemical and Electronic Structure of Solution-Processed Perovskites - Why to (Not) Worry about Pinholes". *Advanced Materials Interfaces*, page 1701420, 2018.

Bibliography

- [76] G. Sadoughi, D. E. Starr, E. Handick, S. D. Stranks, M. Gorgoi, R. G. Wilks, M. Bär, and H. J. Snaith. "Observation and Mediation of the Presence of Metallic Lead in Organic - Inorganic Perovskite Films". *ACS Applied Materials and Interfaces*, 7(24):13440–13444, 2015.
- [77] P. Schulz, L. L. Whittaker-Brooks, B. A. MacLeod, D. C. Olson, Y.-L. Loo, and A. Kahn. "Electronic Level Alignment in Inverted Organometal Perovskite Solar Cells". *Advanced Materials Interfaces*, 2(7):1400532, 2015.
- [78] E. M. Sanehira, B. J. Tremolet de Villers, P. Schulz, M. O. Reese, S. Ferrere, K. Zhu, L. Y. Lin, J. J. Berry, and J. M. Luther. "Influence of Electrode Interfaces on the Stability of Perovskite Solar Cells: Reduced Degradation Using MoO_x/Al for Hole Collection". *ACS Energy Letters*, 1(1):38–45, 2016.
- [79] R. Lindblad, D. Bi, B.-w. Park, J. Oscarsson, M. Gorgoi, H. Siegbahn, M. Odellius, E. M. J. Johansson, and H. Rensmo. "Electronic Structure of TiO₂/CH₃NH₃PbI₃ Perovskite Solar Cell Interfaces". *The Journal of Physical Chemistry Letters*, 5(4):648–653, 2014.
- [80] L. Huang, Z. Hu, G. Yue, J. Liu, X. Cui, J. Zhang, and Y. Zhu. "CH₃NH₃PbI_{3-x}Cl_x films with coverage approaching 100% and with highly oriented crystal domains for reproducible and efficient planar heterojunction perovskite solar cells". *Physical Chemistry Chemical Physics*, 17:22015–22022, 2015.
- [81] G. S. Henderson, X. Liu, and M. E. Fleet. "A Ti L-edge X-ray absorption study of Ti-silicate glasses". *Physics and Chemistry of Minerals*, 29(1):32–42, 2002.
- [82] W. S. M. Werner. "Electron transport in solids for quantitative surface analysis". *Surface and Interface Analysis*, 31(3):141–176, 2001.
- [83] L. Karlsson, S. Svensson, P. Baltzer, M. Carlsson-Gothe, M. P. Keane, A. N. de Brito, N. Correia, and B. Wannberg. "The NVV Auger electron spectrum of the HI molecule". *Journal of Physics B: Atomic, Molecular and Optical Physics*, 22(19):3001, 1989.
- [84] NIST X-ray Photoelectron Spectroscopy (XPS) Database. [Online].
- [85] Y. Zhang, M. Liu, G. E. Eperon, T. C. Leijtens, D. McMeekin, M. Saliba, W. Zhang, M. de Bastiani, A. Petrozza, L. M. Herz, M. B. Johnston, H. Lin, and H. J. Snaith.

Bibliography

- "Charge selective contacts, mobile ions and anomalous hysteresis in organic-inorganic perovskite solar cells". *Materials Horizons*, 2:315–322, 2015.
- [86] Y. K. Gupta and D. N. Sharma. "Kinetics and mechanism of the reduction of iodate to iodite by bromide in the presence of phenol". *The Journal of Physical Chemistry*, 75(16):2516–2522, 1971.
- [87] V. M. Burlakov, G. E. Eperon, H. J. Snaith, S. J. Chapman, and A. Goriely. "Controlling coverage of solution cast materials with unfavourable surface interactions". *Applied Physics Letters*, 104(9):091602, 2014.
- [88] J. F. Moulder, W. F. Stickle, P. E. Sobol, K. D. Bomben, J. Chastain, and R. C. King. *Handbook of X-ray photoelectron spectroscopy: a reference book of standard spectra for identification and interpretation of XPS data*. Physical Electronics Division, Perkin-Elmer Corporation, 1995.
- [89] Y. Li, X. Xu, C. Wang, C. Wang, F. Xie, J. Yang, and Y. Gao. "Investigation on thermal evaporated $\text{CH}_3\text{NH}_3\text{PbI}_3$ thin films". *AIP Advances*, 5(9):097111, 2015.
- [90] W. Su, Y. Zhang, Z. Li, L. Wu, X. Wang, J. Li, and X. Fu. "Multivalency Iodine Doped TiO_2 : Preparation, Characterization, Theoretical Studies, and Visible - Light Photocatalysis". *Langmuir*, 24(7):3422–3428, 2008.
- [91] Q. Zhang, Y. Li, E. A. Ackerman, M. Gajdardziska-Josifovska, and H. Li. "Visible light responsive iodine-doped TiO_2 for photocatalytic reduction of CO_2 to fuels". *Applied Catalysis A: General*, 400(1-2):195–202, 2011.
- [92] G. Liu, C. Sun, X. Yan, L. Cheng, Z. Chen, X. Wang, L. Wang, S. C. Smith, G. Q. (M.) Lu, and H.-M. Cheng. "Iodine doped anatase TiO_2 photocatalyst with ultra-long visible light response: correlation between geometric/electronic structures and mechanisms". *Journal of Materials Chemistry*, 19:2822–2829, 2009.
- [93] T. Oku. *Crystal Structures of $\text{CH}_3\text{NH}_3\text{PbI}_3$ and Related Perovskite Compounds Used for Solar Cells, Solar Cells - New Approaches and Reviews, Prof. Leonid A. Kosyachenko (Ed.)*. InTech, 2015.
- [94] T. Minemoto, T. Matsui, H. Takakura, Y. Hamakawa, T. Negami, Y. Hashimoto, T. Uenoyama, and M. Kitagawa. "Theoretical analysis of the effect of conduction band

Bibliography

- offset of window/CIS layers on performance of CIS solar cells using device simulation". *Solar Energy Materials and Solar Cells*, 67(1-4):83–88, 2001.
- [95] X. Liu and J. R. Sites. "Calculated effect of conduction-band offset on CuInSe₂ solar-cell performance". *AIP Conference Proceedings*, 353(1):444–452, 1996.
- [96] R. Scheer. "Activation energy of heterojunction diode currents in the limit of interface recombination". *Journal of Applied Physics*, 105(10):104505, 2009.
- [97] J. Krüger, U. Bach, and M. Grätzel. "Modification of TiO₂ Heterojunctions with Benzoic Acid Derivatives in Hybrid Molecular Solid-State Devices". *Advanced Materials*, 12(6):447–451, 2000.
- [98] J.A. Dean and N.A. Lange. "*Lange's Handbook of Chemistry*". Number Bd. 15 in Lange's Handbook of Chemistry. McGraw-Hill, 1999.
- [99] C. Momblona, O. Malinkiewicz, C. Roldán-Carmona, A. Soriano, L. Gil-Escrig, E. Bandiello, M. Scheepers, E. Edri, and H. J. Bolink. "Efficient methylammonium lead iodide perovskite solar cells with active layers from 300 to 900 nm". *APL Materials*, 2(8):081504, 2014.
- [100] G. Ketteler, S. Yamamoto, H. Bluhm, K. Andersson, D. E. Starr, D. F. Ogletree, H. Ogasawara, A. Nilsson, and M. Salmeron. "The Nature of Water Nucleation Sites on TiO₂ (110) Surfaces Revealed by Ambient Pressure X-ray Photoelectron Spectroscopy". *The Journal of Physical Chemistry C*, 111(23):8278–8282, 2007.
- [101] H. S. Casalongue, S. Kaya, V. Viswanathan, D. J. Miller, D. Friebe, H. A. Hansen, J. K. Nørskov, A. Nilsson, and H. Ogasawara. "Direct observation of the oxygenated species during oxygen reduction on a platinum fuel cell cathode". *Nature Communications*, 4:2817, 2013.
- [102] Y. K. Kim, B. Jeon, and H. J. Park. "Interfacial Electronic Structure of Methylammonium Lead Iodide Grown on a Mesoporous TiO₂ Layer on F-Doped Tin Oxide Substrate". *The Journal of Physical Chemistry C*, 120(39):22460–22465, 2016.
- [103] M. Chaychian, M. Al-Sheikhly, J. Silverman, and W. L. McLaughlin. "The mechanisms of removal of heavy metals from water by ionizing radiation". *Radiation Physics and Chemistry*, 53(2):145 – 150, 1998.

Bibliography

- [104] J. R. Harwell, T. K. Baikie, I. D. Baikie, J. L. Payne, C. Ni, J. T. S. Irvine, G. A. Turnbull, and I. D. W. Samuel. "Probing the energy levels of perovskite solar cells via Kelvin probe and UV ambient pressure photoemission spectroscopy". *Physical Chemistry Chemical Physics*, 18:19738–19745, 2016.
- [105] L. Weinhardt, O. Fuchs, M. Blum, M. Bär, M. Weigand, J.D. Denlinger, Y. Zubavichus, M. Zharnikov, M. Grunze, C. Heske, and E. Umbach. "Resonant X-ray emission spectroscopy of liquid water: Novel instrumentation, high resolution, and the "map" approach". *Journal of Electron Spectroscopy and Related Phenomena*, 177(2):206 – 211, 2010.
- [106] Q. Wang, Y. Shao, H. Xie, L. Lyu, X. Liu, Y. Gao, and J. Huang. "Qualifying composition dependent p and n self-doping in $\text{CH}_3\text{NH}_3\text{PbI}_3$ ". *Applied Physics Letters*, 105(16):163508, 2014.
- [107] C. Eames, J. M. Frost, P. R. F. Barnes, B. C. O'Regan, A. Walsh, and M. S. Islam. "Ionic transport in hybrid lead iodide perovskite solar cells". *Nature Communications*, 6:7497, 2015.
- [108] K. Lee, Q. Kim, S. An, J. An, J. Kim, B. Kim, and W. Jhe. "Superwetting of TiO_2 by light-induced water-layer growth via delocalized surface electrons". *Proceedings of the National Academy of Sciences of the United States of America*, 111:5784 – 5789, 2014.
- [109] L. Kronik and Y. Shapira. "Surface photovoltage phenomena: theory, experiment, and applications". *Surface Science Reports*, 37(1):1 – 206, 1999.
- [110] P. De Padova, M. Fanfoni, R. Larciprete, M. Mangiantini, S. Priori, and P. Perfetti. "A synchrotron radiation photoemission study of the oxidation of tin". *Surface Science*, 313(3):379 – 391, 1994.
- [111] T. Kendelewicz, P. Soukiassian, M. H. Bakshi, Z. Hurych, I. Lindau, and W. E. Spicer. "Soft x-ray core level photoemission study of the Cs/InP interface formation". *Journal of Vacuum Science & Technology B: Microelectronics Processing and Phenomena*, 6(4):1331–1335, 1988.
- [112] M.-C. Jung, S. R. Raga, and Y. Qi. "Properties and solar cell applications of Pb-free perovskite films formed by vapor deposition". *RSC Advances*, 6:2819–2825, 2016.

Bibliography

- [113] W. E. Spicer, I. Lindau, C. Y. Su, P. W. Chye, and P. Pianetta. "Core-level photoemission of the Cs-O adlayer of NEA GaAs cathodes". *Applied Physics Letters*, 33(11):934–935, 1978.
- [114] J.-C. Zheng, C. H. A. Huan, A. T. S. Wee, and M. H. Kuok. "Electronic properties of CsSnBr₃: studies by experiment and theory". *Surface and Interface Analysis*, 28(1):81–83, 1999.
- [115] E. Handick. "*Surface and interface characterization by X-ray and electron spectroscopies - revealing the peculiarities of Cu(In, Ga)Se₂ chalcopyrite and CH₃NH₃PbI_(3-x)Cl_x perovskite-based thin film solar cell structures*". PhD thesis, 2017.
- [116] M. A. Sánchez-García, X. Bokhimi, A. Maldonado-Álvarez, and A. E. Jiménez-González. "Effect of Anatase Synthesis on the Performance of Dye-Sensitized Solar Cells". *Nanoscale Research Letters*, 10(1):306, 2015.
- [117] D. O. Scanlon, C. W. Dunnill, J. Buckeridge, S. A. Shevlin, A. J. Logsdail, S. M. Woodley, C. R. A. Catlow, M. J. Powell, R. G. Palgrave, I. P. Parkin, G. W. Watson, T. W. Keal, P. Sherwood, A. Walsh, and A. A. Sokol. "Band alignment of rutile and anatase TiO₂". *Nature Materials*, 12:798–801, 2013.
- [118] J.-M. Themlin, M. Chtaïb, L. Henrard, P. Lambin, J. Darville, and J.-M. Gilles. "Characterization of tin oxides by x-ray-photoemission spectroscopy". *Physical Review B*, 46:2460–2466, 1992.
- [119] M. Batzill and U. Diebold. "The surface and materials science of tin oxide". *Progress in Surface Science*, 79(2-4):47–154, 2005.
- [120] N. Pal, M. Paul, A. Bera, D. Basak, and A. Bhaumik. "Synthesis, characterization and enhanced photoconductivity from a mesoporous titania on dye doping". *Analytica Chimica Acta*, 674(1):96 – 101, 2010.
- [121] Z. Bastl and H. Gehlmann. "X-ray photoelectron spectroscopic (XPS) studies of iodine oxocompounds". *Collection of Czechoslovak Chemical Communications*, 53:425 – 432, 1988.
- [122] M. J. Van Stipdonk, V. Santiago, E. A. Schweikert, C. C. Chusuei, and D. W. Goodman. "Secondary ion emission from keV energy atomic and polyatomic projectile impacts on sodium iodate". *International Journal of Mass Spectrometry*, 197(1-3):149–161, 2000.

Bibliography

- [123] X.-L. Zhou, F. Solymosi, P. M. Blass, K. C. Cannon, and J. M. White. "Interactions of methyl halides (Cl, Br and I) with Ag(111)". *Surface Science*, 219(1):294–316, 1989.
- [124] P. M. A. Sherwood. "X-ray photoelectron spectroscopic studies of some iodine compounds". *Journal of the Chemical Society, Faraday Transactions 2: Molecular and Chemical Physics*, 72:1805–1820, 1976.
- [125] A. N. Mansour and C. A. Melendres. "Characterization of KNiIO_6 by XPS". *Surface Science Spectra*, 3(3):287–295, 1994.

Publications

- R. Félix, N. Llobera-Vila, C. Hartmann, C. Klimm, M. Hartig, R. G. Wilks and M. Bär. "Preparation and in-system study of SnCl₂ precursor layers: towards vacuum-based synthesis of Pb-free perovskites." *RSC Advances*, 2018, **8**, 67, DOI: 10.1039/C7RA12172E.
- C. Hartmann, G. Sadoughi, R. Félix, E. Handick, H. W. Klemm, G. Peschel, E. Madej, A. B. Fuhrich, X. Liao, S. Raoux, D. Abou-Ras, D. Wargulski, T. Schmidt, R. G. Wilks, H. Snaith and M. Bär. "Spatially Resolved Insight into the Chemical and Electronic Structure of Solution-Processed Perovskites—Why to (Not) Worry about Pinholes". *Advanced Materials Interfaces* **2018**, 1701420, DOI: 10.1002/admi.201701420.

Acknowledgement

At the end of my thesis I would like to thank people who have supported and helped me through my years as PhD student and made this thesis possible. Writing this dissertation had been a big impact on me accompanied by a period of intense learning in the scientific area as well as on a personal level.

Firstly, I would like to express my sincere gratitude to my advisor Prof. Dr. *Marcus Bär* for the continuous support of my PhD study and related research, for his patience, motivation, and immense knowledge. His guidance helped me in all the time of research and writing of this thesis.

I would also like to thank Dr. *Regan G. Wilks* for his great support in data analysis, technical issues in the lab or at beamlines and for always having an open ear to questions/problems. His motivating feedback during my PhD helped me polishing/learning new skills and accomplishing the thesis.

I thank my collaborators Dr. *Golnaz Sadoughi*, Dr. *Severin Habisreutinger* and Prof. Dr. *Henry Snaith* from Oxford University as well as my collaborators from the Weizmann Institute in Israel Dr. *Satyajit Gupta* and Prof. Dr. *David Cahen* for providing me with samples for my research, sharing their knowledge about perovskites as well as their vulnerable feedback on conducted/planned experiments.

I thank my fellow labmates for the stimulating discussions, for the sleepless nights we were working together at the beamlines, and for all the fun we have had in the last years making my PhD an enjoyable experience in my life. In particular, I am grateful to Dr. *Roberto Félix Duarte* for supervising me and teaching me how to operate HiKE as well as sharing with me countless days/nights at the KMC-1 beamline. I'm also grateful to Dr. *Leonard Köhler* and Dr. *Evelyn Handick* for welcoming me in the group, introducing me to the experimental lab set-up as well as sharing their experience and knowledge as PhD students. I would like to thank Dr. *Xeniya Kozina* for sharing her experience/knowledge about research and lots of beamtimes with me, which I enjoyed a lot and I'm thankful for all the fun and interesting chats between the work.

I'm grateful to Dr. *David Starr* and Dr. *Eva Unger* for the fruitful discussion/sharing their knowledge about AP-HAXPES and perovskites.

I'm also thankful to MSc *Núria Lloberia Vila* for sharing the experience of depositing perovskites with me and giving me the experience/opportunity of tutoring her as a master student. Last but not least, I would like to thank my family: my parents *Manfred* and *Christine Hartmann* for their guidance through out my life and their support to pursue my dreams. I would like to thank my grandmother *Dorothea Kuschel* for her support and my brothers Dipl.-Physiker *Mathias* and MSc *Martin Hartmann* for sharing my passion for science as well as the interesting scientific discussions overlapping different aspects of physics. I would also like to thank my brothers girlfriend MSc *Lam-Ha Ly* for being a good friend and supporting me and I thank my nephew *Aaron Hartmann* for being my little sunshine.

Declaration of Academic Integrity

I declare that this dissertation titled "Surface and Interface Characterization of $\text{CH}_3\text{NH}_3\text{PbI}_{(3-x)}\text{Cl}_x$ and CsSnBr_3 Perovskite based Thin-Film Solar Cell Structures" and the work presented in it are my own. I confirm that this work was done wholly or mainly while in candidature for a research degree at this University. No part of this thesis has previously been submitted for a degree or any other qualification at this University or any other institution. This thesis is my first submission for a PhD degree at any institution. Where I have consulted the published work of others, this is always clearly attributed. Where I have quoted from the work of others, the source is always given. With the exception of such quotations, this thesis is entirely my own work. I have acknowledged all main sources of help. Already published or submitted parts of this thesis are clearly indicated.

place, date

Claudia Marion Hartmann